

Cover Page



Universiteit Leiden



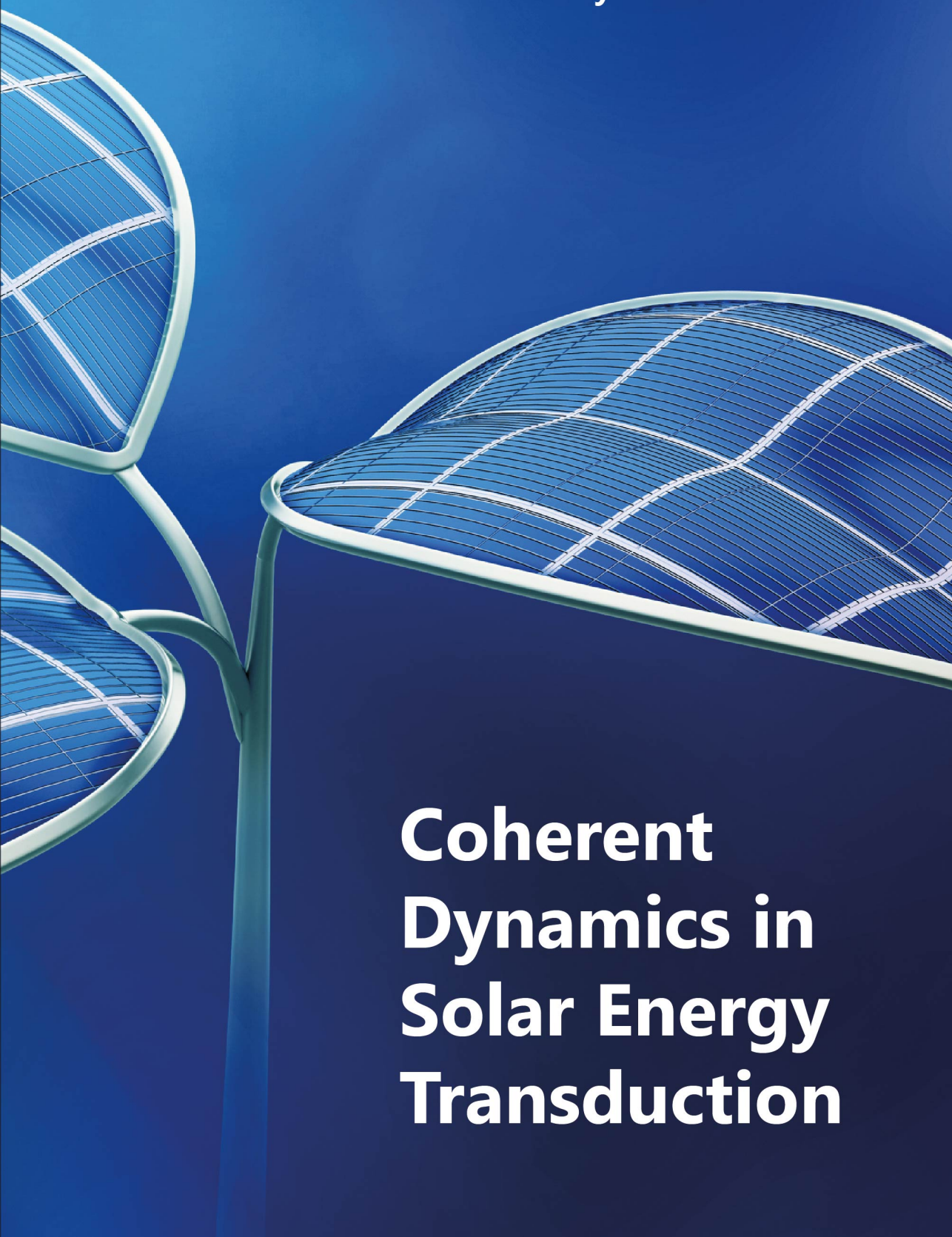
The handle <http://hdl.handle.net/1887/30117> holds various files of this Leiden University dissertation

Author: Eisenmayer, Thomas J.

Title: Coherent dynamics in solar energy transduction

Issue Date: 2014-12-15

Thomas J. Eisenmayer



**Coherent
Dynamics in
Solar Energy
Transduction**

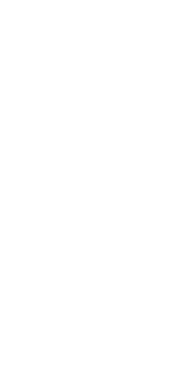
Coherent Dynamics in Solar Energy Transduction

PROEFSCHRIFT

ter verkrijging van
de graad van Doctor aan de Universiteit Leiden,
op gezag van Rector Magnificus prof. mr. C. J. J. M. Stolker,
volgens besluit van het College voor Promoties
te verdedigen op maandag 15 december 2014
klokke 15.00 uur
door

Thomas J. Eisenmayer

geboren te Carrara, Italië
in 1982



Thomas J. Eisenmayer
Coherent Dynamics in Solar Energy Transduction
Ph.D. Thesis, Leiden University

Copyright ©Thomas J. Eisenmayer

No part of this thesis may be reproduced in any form without the express written permission of the copyright holders.

Promotiecommissie

Promotor:

Prof. dr. Huub de Groot

Copromotor:

Dr. Francesco Buda

Overige leden:

Prof. dr. Johannes Neugebauer

Prof. dr. Rienk van Grondelle

Prof. dr. Geert-Jan Kroes

Prof. dr. Jaap Brouwer

This project was carried out within the research programme of BioSolar Cells, co-financed by the Dutch Ministry of Economic Affairs (project C1.9).

The use of supercomputer facilities was sponsored by NWO Physical Sciences, with financial support from the Netherlands Organization for Scientific Research (NWO).

We acknowledge also the PRACE-3IP project (FP7 RI-312763) for the use of supercomputing resources.

Table of Contents

Symbols	i
Abbreviations	iii
1 Introduction	1
1.1 Artificial Photosynthesis	2
1.1.1 Solar Light Absorption	3
1.1.2 Photoinduced Charge Separation	5
1.2 Coupling and Coherence	7
1.3 Natural Photosynthesis	8
1.3.1 The Bacterial Reaction Center	8
1.3.2 Photosystem II	10
1.4 References	11
2 Theoretical Methods	13
2.1 Methods I: The Electronic Problem	13
2.1.1 The Ground State	14
2.1.2 Excited States	17
2.2 Methods II: Propagating the Nuclei	19
2.2.1 Adiabatic Molecular Dynamics	19
2.2.2 Nonadiabatic Molecular Dynamics	20
2.3 References	23
3 Efficient Evolution of Excitons into Charge Transfer States	25
3.0.1 ABSTRACT	25
3.1 Introduction	26
3.2 The Ground State	28
3.3 The Excited State	32
3.4 Conclusions	34
3.5 References	34
4 Stable Charge Separation through Proton Displacements	37
4.0.1 ABSTRACT	37
4.1 Introduction	38
4.2 Model and Methods	40

4.3	Results	41
4.4	Discussion and Conclusions	47
4.5	References	49
5	Photoinduced Coherent Charge Transfer	53
5.0.1	ABSTRACT	53
5.1	Introduction	54
5.2	Model and Methods	54
5.3	Results and Discussion	58
5.4	Conclusions	61
5.5	References	62
5.6	Appendices	64
6	Redox Levels and Potentials	67
6.0.1	ABSTRACT	67
6.1	Introduction	68
6.2	Models and Methods	68
6.3	Results and Discussion	70
6.4	Conclusions	75
6.5	References	76
7	Proton-Coupled Electron Transfer	79
7.0.1	ABSTRACT	79
7.1	Introduction	80
7.2	Model and Methods	81
7.3	Results and Discussion	82
7.4	Conclusions	86
7.5	References	87
8	Conclusions and Outlook	89
8.1	Conclusions	89
8.2	Outlook	90
8.3	References	91
	Summary	93
	Samenvatting	95
	Curriculum Vitae	97
	List of Publications	100

Symbols

\mathbf{a}, \mathbf{A}	vector \vec{a}, \vec{A} (bold)
a_{ij}	density matrix element
$a(t)$	acceleration
$c_i(t)$	time-dependent coefficient
$\chi(\mathbf{R}(t))$	nuclear wavefunction
$d_{ij}(\mathbf{r}, \mathbf{R}(t))$	nonadiabatic coupling
ϵ_i	orbital energy
ε_i	photon energy
E	energy
$E_0(\mathbf{R}(t))$	ground state energy
$E_i(\mathbf{R}(t))$	excited state energy
$\hat{\mathcal{H}}(\mathbf{r}, \mathbf{R}(t))$	Hamiltonian operator
$\hat{\mathcal{H}}_e(\mathbf{r}, \mathbf{R}(t))$	electronic Hamiltonian
$\hat{\mathcal{H}}_{ij}(\mathbf{r}, \mathbf{R}(t))$	Hamiltonian matrix element
f_i	oscillator strength
F	force
γ_c	bath correlation time
$\Gamma(t)$	density matrix
ΔG	free energy difference
λ	reorganization energy
$\hat{\mu}$	dipole moment operator
M	mass
N	number of electrons
∇_i	differential operator
O	observable
$\phi(\mathbf{r})$	molecular orbital
$\varphi(\mathbf{r}, t)$	time-dependent molecular orbital
$\psi(\mathbf{r}; \mathbf{R}(t))$	electronic wavefunction
$\Psi(\mathbf{r}, \mathbf{R}(t))$	electron-nuclear wavefunction
$\Psi(\mathbf{r}, \mathbf{R}, t)$	total time-dependent wavefunction
$PSD(\mathbf{r}, t)$	photoinduced spin density
ρ	electron density
ρ_0	ground state electron density

$\rho^{\alpha,\beta}$	<i>spin polarized electron density</i>
\mathbf{r}	<i>electronic coordinate</i>
\mathbf{R}	<i>nuclear coordinate</i>
$\mathbf{R}(t)$	<i>nuclear trajectory</i>
$\mathbf{R}'(t)$	<i>specific nuclear motion</i>
t	<i>time</i>
Δt	<i>timestep</i>
\hat{T}	<i>kinetic energy operator</i>
v	<i>single particle potential</i>
V	<i>potential energy</i>
V_{el-el}	<i>electron-electron potential</i>
V_{el-n}	<i>electron-nucleus potential</i>
V_{n-n}	<i>nucleus-nucleus potential</i>
$v(t)$	<i>velocity</i>
\hat{W}	<i>electronic population operator</i>
$x(t)$	<i>position</i>
Z_I	<i>nuclear charge</i>

Abbreviations

ADF	<i>Amsterdam Density Functional</i>
AIMD	<i>Ab Initio Molecular Dynamics</i>
BiP	<i>Benzimidazolephenol</i>
BLYP	<i>Becke Lee Yang Parr</i>
bRC	<i>Bacterial Reaction Center</i>
CCSD	<i>Coupled Cluster Singles and Doubles</i>
CDFT	<i>Constrained Density Functional Theory</i>
COSMO	<i>Conductor-Like Screening Model</i>
CPMD	<i>Car-Parrinello Molecular Dynamics</i>
CT	<i>Charge Transfer</i>
DCACP	<i>Dispersion Corrected Atom Centered Pseudopotentials</i>
DFT	<i>Density Functional Theory</i>
ENDOR	<i>Electron Nuclear Double Resonance</i>
EOM	<i>Equations of Motion</i>
EPR	<i>Electron Paramagnetic Resonance</i>
ET	<i>Electron Transfer</i>
GGA	<i>Generalized Gradient Approximation</i>
HF	<i>Hartree-Fock</i>
HOMO	<i>Highest Occupied Molecular Orbital</i>
HSD	<i>Hole Spin Density</i>
LDA	<i>Local Density Approximation</i>
LUMO	<i>Lowest Unoccupied Molecular Orbital</i>
MM	<i>Molecular Mechanics</i>
MPI	<i>Message Passing Interface</i>
NDI	<i>Napthalene Diimide</i>
NMR	<i>Nuclear Magnetic Resonance</i>
OCTOPUS	<i>Open-Source Software for Real-Time TDDFT</i>
OEC	<i>Oxygen Evolving Complex</i>
PCET	<i>Proton-Coupled Electron Transfer</i>
PDB	<i>Protein Data Bank</i>
PES	<i>Potential Energy Surface</i>
PSII	<i>Photosystem II</i>
PSD	<i>Photoinduced Spin Density</i>

QM	<i>Quantum Mechanics</i>
RC	<i>Reaction Center</i>
RMSD	<i>Root Mean Square Displacement</i>
ROKS	<i>Restricted Open-Shell Kohn Sham</i>
TDDFT	<i>Time-Dependent Density Functional Theory</i>
TZP	<i>Triple Zeta Polarized Basis Set</i>
VDOS	<i>Vibrational Density of States</i>

Chapter 1

Introduction

This thesis is concerned with the transfer of energy from light to matter. Over a century ago it was established that light consists of packets of energy [1], now known as photons. Not much later the energy levels of matter at the atomic scale were found to be discrete [2]. These phenomena required a new physical description that has become the theory of quantum mechanics [3]. Now, this theory of light and matter could contribute to tackling a fundamental socioeconomic and technological challenge: To find a sustainable supply of useful energy that is cheap, abundant and generated on-the-spot.

For this purpose the sun is the most obvious energy source as it is abundant and readily available almost everywhere. Evolution has developed a mechanism to capture and convert solar irradiation and fixate atmospheric carbon, known as photosynthesis. Ironically, one of the major societal concerns today regarding the supply of energy is related to the re-emission of this carbon millions of years after it was sequestered. Nevertheless, the bulk of the energy supply remains fossil, illustrating that the dependence on energy is deeply rooted. This is not surprising as the availability of affordable energy is highly correlated with living standards. It also tells that there is no current alternative. Therefore, a technology that can generate fuel or electricity from solar irradiation in real-time would be an elegant solution.

Mimicking the highly efficient sunlight to charge, and charge to fuel conversions in photosynthesis has become the objective of a scientific field called artificial photosynthesis [4,5]. In this work, the processes initiated by the absorption of a solar photon in photosynthetic complexes (**Chapters 3,4 and 6**) as well as biomimetic systems (**Chapters 5 and 7**) are analyzed. The mixing of quantum states through resonant coherent nuclear motion is found to drive the efficient conversion of light into separated charges in the first section (**Chapters 3-5**). In the final part (**Chapters 6-7**) results are presented on stabilizing separated charges and the interfacing with catalysis.

1.1 Artificial Photosynthesis

Generating fuel from sunlight and water is a conceptually simple process (Figure 1.1). An incident solar photon is absorbed by a molecule resulting in an excited state ($molecule \rightarrow molecule^*$). The neutral excited electron-hole pair (exciton) undergoes charge separation through the transfer of an electron to a mediator, while the electron vacancy (the hole) is transferred to a different mediator.

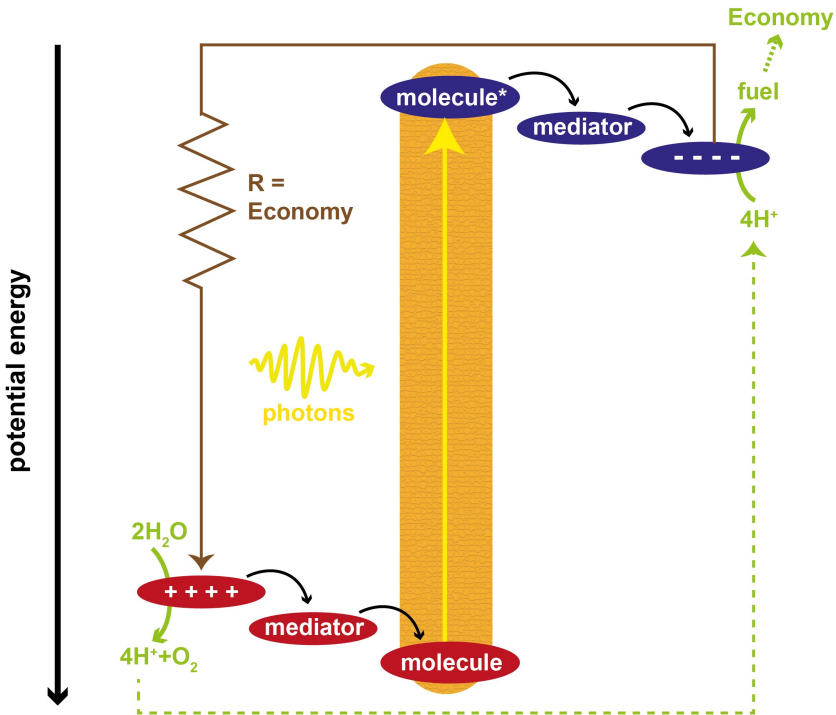


Figure 1.1: Supplying the economy with energy from the sun can be either achieved through photoproduction of electricity (brown) or fuel (green).

Mediators are required to spatially separate the electron and hole. The movement of a hole is also an electronic process. In the conventional picture it is transferred by means of an electron from a neighbouring molecule filling the positive vacancy, thereby displacing the hole from its initial site to the new molecule. The transfer of charge from an excited state of a molecule to a mediator is a quantum mechanical process that involves the system changing its quantum mechanical state.

Metal oxides are known to be good mediators for photoexcited electrons [6]. The early 90's also saw the development of polymer systems that rapidly transfer the photoexcited electrons to buckminsterfullerene (C60) [7]. Both systems, now referred to as dye-sensitized and bulk-heterojunction solar cells, are becoming commercially available for small-scale electricity generation [8]. A promising hole mediator is the recent molecule found by Moore and coworkers [9] that mimics an ingenious mechanism in oxygenic photosynthesis to store positive charges (see **Chapter 7**). The most efficient systems for direct photoinduced water splitting (e.g. [10]) unfortunately still contain very expensive semiconducting components.

In this context, the screening of large numbers of molecules for their potential to produce stable charge separated states is crucial to find more efficient systems for artificial photosynthesis. As it is far from trivial to synthesize molecules, smart strategies are needed to answer questions such as:

- (1) What is the fraction of solar irradiation that is absorbed by the molecules?
- (2) What is the percentage of absorbed photons that actually evolve into stable charge separated states?

Quantum Mechanics (QM) contains the answers to these questions. In the following QM will be introduced in the context of solar energy transduction within Schrödinger's picture of QM as this most closely resembles the computational methods employed in this thesis. In section 1.1.3 the concepts of coupling and coherence will briefly be discussed. Atomic units are used throughout.

1.1.1 Solar Light Absorption

The first step in considering question (1) - from a computational chemists perspective - is to find the ground state energy E_0 from Schrödinger's time-independent equation:

$$\hat{H}(\mathbf{r}, \mathbf{R}(t))\Psi_0(\mathbf{r}, \mathbf{R}(t)) = E_0(\mathbf{R}(t))\Psi_0(\mathbf{r}, \mathbf{R}(t)), \quad (1.1)$$

where $\Psi_0(\mathbf{r}, \mathbf{R}(t))$ is the ground state wavefunction that is a function of the coordinates of the electrons \mathbf{r} and nuclei $\mathbf{R}(t)$. The time-dependence $\mathbf{R} = \mathbf{R}(t)$ is added explicitly to emphasize that the wavefunction *does* change as the nuclear positions evolve in time. $\hat{H}(\mathbf{r}, \mathbf{R}(t))$ is the total unperturbed time-independent Hamiltonian. The total set of eigenvalues

including excited states can be found by considering the full spectrum of the Hamiltonian¹:

$$\hat{H}(\mathbf{r}, \mathbf{R}(t)) \begin{pmatrix} \Psi_0 \\ \Psi_1 \\ \Psi_2 \\ \vdots \\ \Psi_i \end{pmatrix} = \begin{pmatrix} E_0 & 0 & 0 & \cdots & 0 \\ 0 & E_1 & 0 & \cdots & 0 \\ 0 & 0 & E_2 & \cdots & 0 \\ \vdots & \vdots & \vdots & \ddots & \vdots \\ 0 & 0 & 0 & \cdots & E_i \end{pmatrix} \begin{pmatrix} \Psi_0 \\ \Psi_1 \\ \Psi_2 \\ \vdots \\ \Psi_i \end{pmatrix}. \quad (1.2)$$

For every transition between the ground state and an excited state i an oscillator strength f_i can be calculated [11]:

$$f_i = 2/3(E_i - E_0)|\langle \Psi_0 | \hat{\mu} | \Psi_i \rangle|^2, \quad (1.3)$$

where the energy gap ($E_i - E_0$) is the excitation or photon energy (ε_i) required to bring the system from the ground state to excited state i and $\hat{\mu}$ is the dipole moment operator. In Figure 1.2 the oscillator strengths of a hypothetical molecule are plotted with the solar irradiation spectrum.

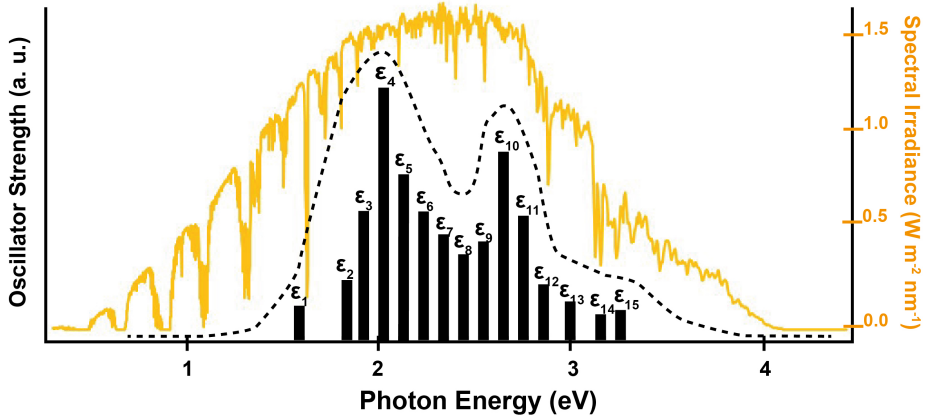


Figure 1.2: Comparison of the solar irradiation spectrum (AM 1.5, orange line) with a schematic representation of the excitation energies ε_i and their respective oscillator strength.

Calculating the overlap between the convoluted excitations (dotted line, figure 2.1) obtained from QM and the solar spectrum provides a reasonable answer to question (1).

¹Note that *electron-nuclear* wavefunctions are discussed (not molecular orbitals), therefore the lowest eigenfunction is the ground state $\Psi_0(\mathbf{r}, \mathbf{R}(t))$.

1.1.2 Photoinduced Charge Separation

The more difficult question is (2). The static QM picture discussed so far doesn't provide the necessary information to successfully answer (2). To simulate whether the excited states $\Psi_i(\mathbf{r}, \mathbf{R}(t))$ will undergo charge separation - again from a computational chemists perspective - requires solving the time-dependent Schrödinger equation:

$$i \frac{\partial \Psi(\mathbf{r}, \mathbf{R}, t)}{\partial t} = \hat{\mathcal{H}}(\mathbf{r}, \mathbf{R}(t)) \Psi(\mathbf{r}, \mathbf{R}, t). \quad (1.4)$$

This can be achieved by constructing the time-dependent wavefunction $\Psi(\mathbf{r}, \mathbf{R}, t)$ from a basis of time-independent wavefunctions that are eigenstates of the Hamiltonian [12]:

$$\Psi(\mathbf{r}, \mathbf{R}, t) = \sum_i c_j(t) \Psi_j(\mathbf{r}, \mathbf{R}(t)). \quad (1.5)$$

where $c_j(t)$ are the time-dependent coefficients that can be seen as the weights of the specific states in the total wavefunction. The stationary eigenstates change as the nuclear coordinates $R(t)$ evolve in time. Therefore, different excited states can be prepared through the initial conditions of the time dependent coefficients:

$$c_1(0) = 0, \dots, c_i(0) = 1, \dots, c_j(0) = 0, \quad (1.6)$$

where these initial conditions correspond to the molecule in excited state i after absorption of a photon with energy $(E_i - E_0)$. To properly answer (2) one would need to prepare initial conditions 1.6 for all excited states with non-negligible oscillator strength, substitute the resulting expansions 1.5 into equation 1.4 and evolve $\Psi(\mathbf{r}, \mathbf{R}, t)$ starting from a statistically representative ensemble of nuclear coordinates for each excited state.

A way to interpret the results is the visualization of the excited state progression through the spatial difference in particle density between spin up and spin down electrons (this is done within Kohn-Sham in **Chapter 5**)²:

$$\begin{aligned} PSD(\mathbf{r}, t) = & N \int \Psi^*([\mathbf{r}, \uparrow] \mathbf{x}_2 \cdots \mathbf{x}_N) \Psi([\mathbf{r}, \uparrow] \mathbf{x}_2 \cdots \mathbf{x}_N) d\mathbf{x}_2 \cdots d\mathbf{x}_N \\ & - N \int \Psi^*([\mathbf{r}, \downarrow] \mathbf{x}_2 \cdots \mathbf{x}_N) \Psi([\mathbf{r}, \downarrow] \mathbf{x}_2 \cdots \mathbf{x}_N) d\mathbf{x}_2 \cdots d\mathbf{x}_N, \end{aligned} \quad (1.7)$$

²This visualization method will not give the charge transfer when spin and charge decouple (as observed in Chapter 7).

where N is the total number of electrons. If the excited electron is spin up, negative regions of the $PSD(\mathbf{x}, t)$ will represent the photoinduced hole, whereas the positive regions will represent the photoinduced electron. In most cases, excited states with significant oscillator strength are of excitonic character, meaning that the electron and hole regions of the $PSD(\mathbf{x}, t)$ overlap significantly as visualized in Figure 1.3 for a hypothetical linear molecule.

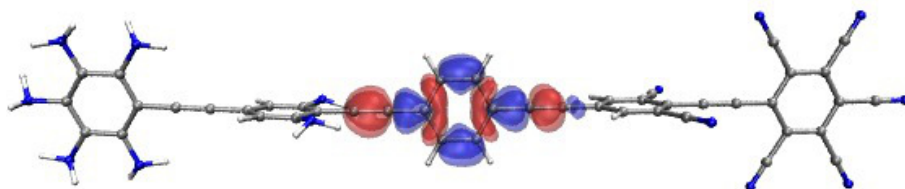


Figure 1.3: Spatial distribution of the $PSD(\mathbf{x}, 0)$ in a hypothetical linear molecule for an excitonic state. The red isosurface corresponds to the photoinduced hole and the blue isosurface to the photoinduced electron (*Isosurfaces are visualized through the Kohn-Sham equivalent of equation 1.8: see Chapter 5, equation 5.5*).

However, the $PSD(\mathbf{x}, 0)$ need not be symmetric as in Figure 1.3. The initial excited state in vision, for example, is significantly polarized [13]. Charge transfer states generally are characterized by a large(r) spatial separation between the hole and electron regions of the $PSD(\mathbf{x}, t)$ (Figure 1.4).

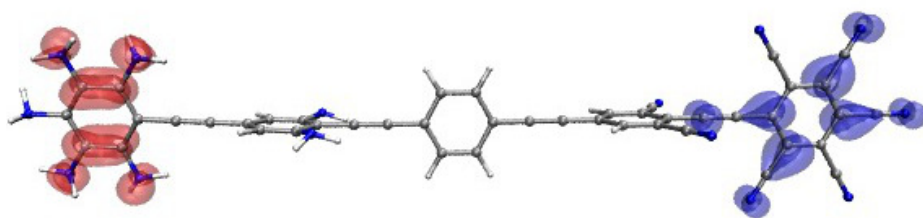


Figure 1.4: Spatial distribution of the $PSD(\mathbf{x}, \tau)$ in a hypothetical linear molecule for a charge transfer state.

With this interpretation scheme, all the different time traces can be visualized to follow the progression of the excited states. This will enable a quantitative assessment of the progression of initial excitonic states into lower lying charge transfer states and provide an answer to (2).

1.2 Coupling and Coherence

In practice, the wavefunctions are not known and equation 1.4 and expansion 1.5 in section 1.1.2 need to be approximated (see **Chapter 2**). This is not trivial and requires significant computational resources even for short simulations of small molecules. Therefore, an understanding of the underlying physical or chemical process is important.

Consider substituting expansion 1.5 in equation 1.4 and projecting both sides of the resulting equation on a set of functions $\Psi_k(\mathbf{r}, \mathbf{R}(t))$, with coefficients $c_k(t)$, then the time evolution of the coefficients reads [12]:

$$i \frac{\partial c_k(t)}{\partial t} = \left[\hat{\mathcal{H}}_{kj}(\mathbf{r}, \mathbf{R}(t)) - i \langle \Psi_k | \nabla_{\mathbf{R}} | \Psi_j \rangle \cdot \frac{d\mathbf{R}(t)}{dt} \right] c_j(t). \quad (1.8)$$

The terms between brackets, the Hamiltonian matrix elements $\hat{\mathcal{H}}_{kj}$ and the second term that is the nonadiabatic coupling \mathbf{d}_{kj} between states k and j , are responsible for transitions. Interestingly, $\hat{\mathcal{H}}_{kj}(\mathbf{r}, \mathbf{R}(t))$ and $\mathbf{d}_{kj}(\mathbf{r}, \mathbf{R}(t))$ do not explicitly depend on time in this representation. Their change is effectuated through the implicit time-dependence on the nuclear coordinates $\mathbf{R}(t)$. Therefore, finding the specific nuclear motion $\mathbf{R}'(t)$ that evolves the reactant state into the desired product state is key. This topic is covered in **Chapters 3,4,5 and 7** for photosynthetic and biomimetic systems.

To better understand the nature of $\mathbf{R}'(t)$ consider a subspace of the Hilbert space comprising two states as the only ones that can interact, against a background manifold of states that are energetically well separated. For illustrative purposes let these be an exciton $\Psi_e(\mathbf{r}, \mathbf{R}(t))$ and a charge transfer state $\Psi_c(\mathbf{r}, \mathbf{R}(t))$ with coefficients $c_e(t)$ and $c_c(t)$. A 2x2 density matrix $\Gamma(t)$ can then be constructed for these states as:

$$\Gamma(t) = \begin{bmatrix} a_{ee}(t) & a_{ec}(t) \\ a_{ce}(t) & a_{cc}(t) \end{bmatrix} = \begin{bmatrix} c_e(t)c_e(t)^* & c_e(t)c_c(t)^* \\ c_c(t)c_e(t)^* & c_c(t)c_c(t)^* \end{bmatrix}. \quad (1.9)$$

Here, the diagonal elements are the populations and the off-diagonal elements represent the coherences that mix the states [14]. Consider a nuclear motion $\mathbf{R}'(t)$ that oscillates at resonance with the matrix element $a_{ec}(t) = c_e(t)c_c(t)^*$ responsible for mixing the charge transfer into the exciton. The process of photoinduced charge transfer is most efficient when it couples to such coherent nuclear motion.

1.3 Natural Photosynthesis

1.3.1 The Bacterial Reaction Center

In bacterial photosynthesis all absorbed photons are converted into stable charge separated states by reaction center (bRC) complexes [15,16]. When a photon is absorbed by a light-active bacteriochlorophyll pigment the resulting electron-hole pair - the exciton - is neutral. Only when an electron is transferred to a neighbouring pigment and the resulting electron vacancy - the hole - is not, charges are separated. Given the identical nature of the pigments in photosynthesis and the invariable locus of the charge separation (the reaction center), the evolutionary optimization of solar energy transduction must be strongly linked to the protein matrix surrounding the pigments (Figure 1.5).

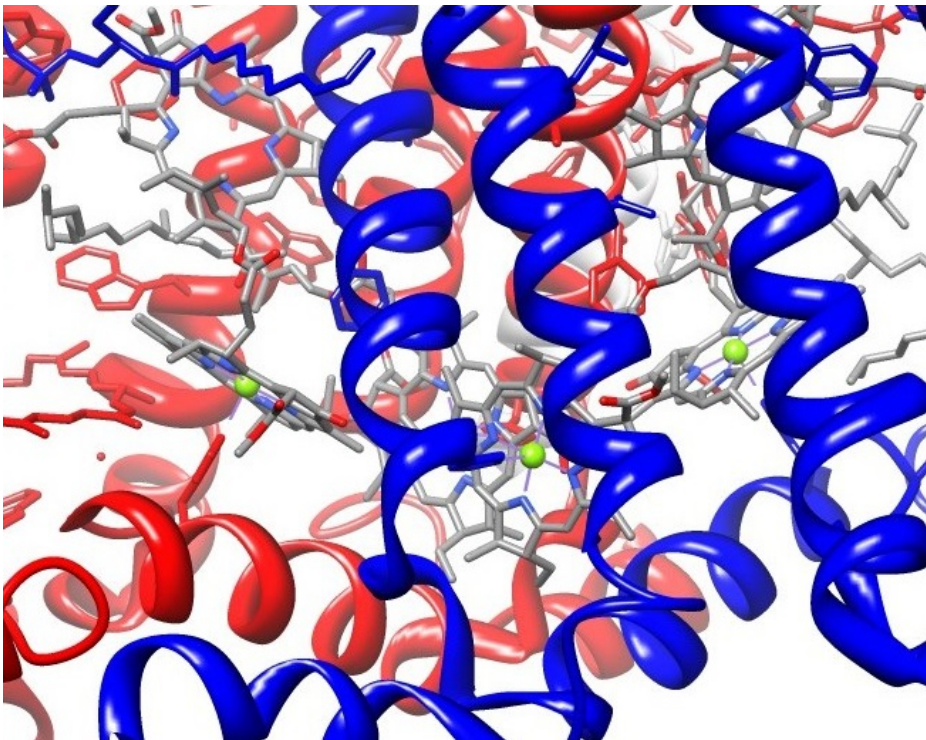


Figure 1.5: Zoomed-in view of the x-ray crystal structure of the *Rhodospirillum rubrum* reaction center (PDB-entry: 1M3X). The special pair bacteriochlorophylls (P) can be seen incased in the protein matrix, with on either side an accessory bacteriochlorophyll (B) and a bacteriopheophytin (H).

In fact, the vibrational spectrum of the site where excitons are dissociated in bRC – the special pair – differs markedly from that of its neighbouring pigment [17]. What is then the parameter that evolution has used to optimize charge separation? The answer may be specific coherent nuclear dynamics first reported in 1993 [18] that control the efficient evolution of excitons into separated charges ([19] and **Chapter 3** of this thesis). Figure 1.6 shows the pigments in bRC without the protein matrix. It can be seen that there is a two-fold symmetry between the cofactor branches. The special pair (P) is the closely coupled pair of bacteriochlorophylls (in white). Peripheral antenna complexes transfer photoinduced excitons to P . Here they are localized long enough to allow them to coherently couple to a low frequency collective mode of the pigments and the protein matrix (see **Chapter 3**). This mode introduces partial charge transfer character into the exciton (**Chapter 3**). The full charge separation takes place on a 3 ps timescale and involves a transfer of the excited electron to the accessory bacteriochlorophyll B_A ([20] and **Chapter 4**), while the hole remains on P . An interstitial water between P and B_A may play a crucial role in facilitating the full transfer ([21] and **Chapter 4**). Subsequent electron transfer from B_A to H_A (the right bottom red bacteriopheophytin in Figure 1.6) is fast and occurs on a 1 ps timescale.

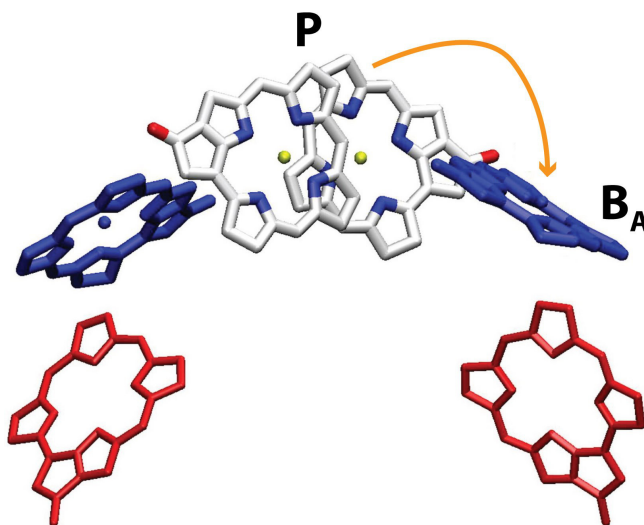


Figure 1.6: Twofold symmetric architecture of the bRC without protein environment. The first photoinduced electron transfer step (orange arrow) from P to B_A is illustrated.

1.3.2 Photosystem II

The Photosystem II reaction center (PSII) is commonly found in plants. It performs very efficient photoinduced charge separation and interfaces the charge separation with the slower process of water oxidation in the oxygen evolving center (OEC). Furthermore PSII possesses the highest known oxidation potential in living organisms (see **Chapter 6** of this thesis), which is required to drive the water oxidation. The branched structure of the chlorophyll pigments is shown in Figure 1.7 and comes from the latest highly accurate crystal structure [22].

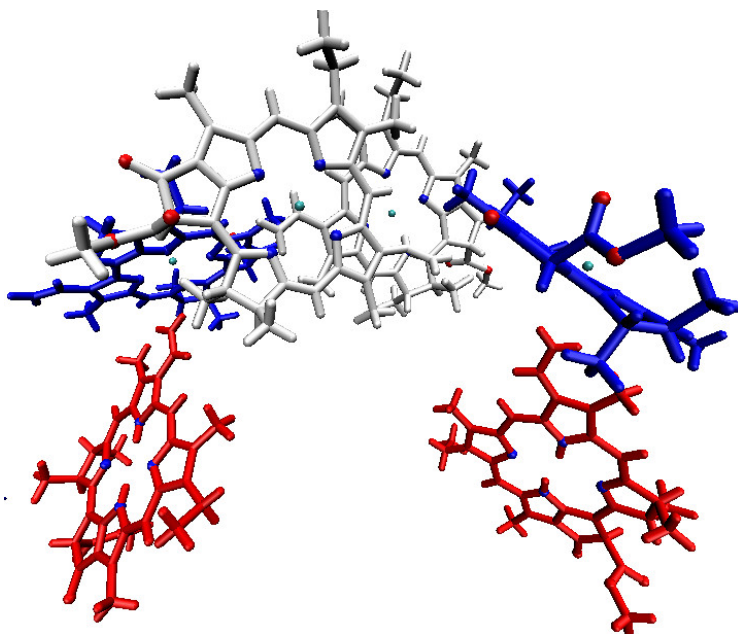


Figure 1.7: Twofold symmetric architecture of pigments in the Photosystem II reaction center without protein environment.

Interestingly the redox gradients between pigments in PSII are much smaller than in bRC (see [23] and **Chapter 6** of this thesis). To bridge the time scales of charge separation and catalysis an interstitial amino acid in the protein (Tyr_Z) is able to reversibly transfer a proton to another amino acid (His_Z) upon oxidation (see [24] and **Chapter 7** of this thesis). Finally, also in PSII very recently signatures of coherent nuclear motion coupled to photoinduced charge transfer have been observed [25,26] that drive the process along different charge separation pathways [27].

1.4 References

- [1] Albert Einstein, Über einen die Erzeugung und Verwandlung des Lichtes betreffenden heuristischen Gesichtspunkt, *Annalen der Physik*, **1905**, 17, 132-148.
- [2] Erwin Schrödinger, Quantisierung als Eigenwertproblem, *Annalen der Physik*, **1926**, (Erste Mitteilung) 79: 361-376, (Zweite Mitteilung) 79: 489-527, (Dreite Mitteilung) 80: 437-490, (Vierte Mitteilung) 81: 109-139.
- [3] A. M. Dirac, (1930). The Principles of Quantum Mechanics.
- [4] Michael Grätzel, Artificial photosynthesis: water cleavage into hydrogen and oxygen by visible light, *Accounts of Chemical Research*, **1981**, 14, 376-384.
- [5] D. Gust, T. A. Moore, A. L. Moore. Solar fuels via artificial photosynthesis. *Accounts of chemical research*, **2009**, 42, 1890-898.
- [6] B. O'Regan and M. Grätzel. A low-cost, high-efficiency solar cell based on dye-sensitized colloidal TiO_2 films, *Nature*, **1991**, 353, 737-740.
- [7] N. S. Sariciftci, L. Smilowitz, A. J. Heeger, F. Wudl, Photoinduced Electron Transfer from a Conducting Polymer to Buckminsterfullerene, *Science*, **1992**, 258, 1474-1476.
- [8] For example: <http://gcell.com/> and <http://www.heliatek.com/>.
- [9] J. D. Megiato Jr, D. D. Mendez-Hernandez, M. E. Tejada-Ferrari, A. Teillout, M. J. Llansola-Portoles, G. Kodis, O. G. Poluektov, T. Rajh, V. Mujica, T. L. Groy, D. Gust, T. A. Moore & A. L. Moore, A bioinspired redox relay that mimics radical interactions of the Tyr-His pairs of photosystem II, *Nature Chemistry*, **2014**, 6, 423-428.
- [10] O. Khaselev and J. A. Turner, A Monolithic Photovoltaic-Photoelectrochemical Device for Hydrogen Production via Water Splitting, *Science*, **1998**, 280, 425-427.
- [11] R. S. Mulliken and C. A. Rieke, Molecular electronic spectra, dispersion and polarization: The theoretical interpretation and computation of oscillator strengths and intensities, *Rep. Prog. Phys.*, **1941**, 8, 231.
- [12] A. V. Akimov, A. J. Neukirch and O. V. Prezhdo, Theoretical Insights into Photoinduced Charge Transfer and Catalysis at Oxide Interfaces, *Chemical Reviews*, **2013**, 6, 4496.
- [13] F. Buda, H. J. M. de Groot, A. Bifone, Charge localization and dynamics in rhodopsin, *Physical Review Letters*, **77**, 4474-4477.
- [14] C. Zener, Non-Adiabatic Crossing of Energy Levels. *Proceedings of the Royal Society A: Mathematical, Physical and Engineering Sciences*, **1932**, 137, 696-702.
- [15] R. E. Blankenship, Molecular Mechanisms of Photosynthesis, **2014**, 2nd Ed. *Wiley-Blackwell*, Oxford, UK.

- [16] Deisenhofer, J.; Epp, O.; Miki, K.; Huber, R.; Michel, H. Structure of the Protein Subunits in the Photosynthetic Reaction Centre of *Rhodospseudomonas Viridis* at 3Å Resolution. *Nature* **1985**, 318, 618-624.
- [17] N. J. Cherepy, A. P. Shreve, L. J. Moore, S. Franzen, S. G. Boxer, R. A. Mathies, Near-Infrared Resonance Raman Spectroscopy of the Special Pair and the Accessory Bacteriochlorophylls in Photosynthetic Reaction Centers, *J. Phys. Chem.*, **1994**, 98, 602.
- [18] M. H. Vos, F. Rappaport, J. C. Lambry, J. Breton, J. L. Martin, Visualization of coherent nuclear motion in a membrane protein by femtosecond spectroscopy, *Nature*, **1993**, 363, 320-325.
- [19] Novoderezhkin, V.; Yakovlev, A.; van Grondelle, R.; Shuvalov, V. Coherent Nuclear and Electronic Dynamics in Primary Charge Separation in Photosynthetic Reaction Centers: A Redfield Theory Approach. *J. Phys. Chem. B*, **2004**, 108, 7445-7457.
- [20] Holzappel, W., Finkle, U., Kaiser, W., Oesterhelt, D., Scheer, H., Stiltz, H.U., and Zinth, W., Initial electron-transfer in the reaction center from *Rhodobacter sphaeroides*, *PNAS* **1990**, 87, 5168-5172.
- [21] Potter, J. A.; Fyfe, P. K.; Frolov, D.; Wakeham, M. C.; Grondelle, R. V.; Robert, B.; Jones, M. R. Strong Effects of an Individual Water Molecule on the Rate of Light-driven Charge Separation in the *Rhodobacter sphaeroides* Reaction Center. *Biochemistry* **2005**, 280, 27155-27164.
- [22] Umena, Y., Kawakami, K., Shen, J.-R., and Kamiya, N., Crystal structure of oxygen-evolving photosystem II at a resolution of 1.9 Å, *Nature* **2011**, 473, 55-60.
- [23] Konermann, L., and Holzwarth, A.R., Analysis of the absorption spectrum of photosystem II reaction centers: Temperature dependence, pigment assignment, and inhomogeneous broadening, *Biochemistry* **1996**, 35, 829-842.
- [24] L. Hammarstrom and S. Styring, Proton-coupled electron transfer of tyrosines in photosystem II and model systems for artificial photosynthesis, *Energy Environ. Sci.*, **2011**, 4, 2379-2388.
- [25] Romero, E., Augulis, R., Novoderezhkin, V.I., Ferretti, M., Thieme, J., Zigmantas, D., and van Grondelle, R., Quantum coherence in photosynthesis for efficient solar-energy conversion, *Nature Physics* **2014**, *advanced publication*.
- [26] Fuller, F.D., Pan, J., Gelzinis, A., Butkus, V., Senlik, S.S., Wilcox, D.E., Yocum, C.F., Valkunas, L., Abramavicius, D., and Ogilvie, J.P., Vibronic coherence in oxygenic photosynthesis, *Nature Chemistry* **2014**, 6, 706-711.
- [27] Romero, E., van Stokkum, I.H.M., Novoderezhkin, V.I., Dekker, J.P., and van Grondelle, R., Two Different Charge Separation Pathways in Photosystem II, *Biochemistry* **2010**, 49, 4300-4307.

Chapter 2

Theoretical Methods

In section 2.1 the fast (electrons) and slow (nuclei) variables are separated using the adiabatic (Born-Oppenheimer) approximation. Density Functional Theory is introduced and excited state methods are discussed. Section 2.2 contains the methods used in this thesis to evolve the nuclei within and beyond the adiabatic approximation.

2.1 Methods I: The Electronic Problem

The total unperturbed Hamiltonian:

$$\begin{aligned} \hat{\mathcal{H}}(\mathbf{r}, \mathbf{R}(t)) = & - \sum_J \frac{1}{2M_J} \nabla_J^2 - \sum_j \frac{1}{2} \nabla_j^2 + \sum_{J < K} \frac{Z_J Z_K}{|\mathbf{R}_J - \mathbf{R}_K|} \\ & + \sum_{j < k} \frac{1}{|\mathbf{r}_j - \mathbf{r}_k|} - \sum_{Jj} \frac{Z_J}{|\mathbf{R}_J - \mathbf{r}_j|} \end{aligned} \quad (2.1)$$

can be condensed to a nuclear kinetic energy \hat{T}_n and an electronic Hamiltonian $\hat{\mathcal{H}}_e(\mathbf{r}, \mathbf{R}(t))$:

$$\hat{\mathcal{H}}(\mathbf{r}, \mathbf{R}(t)) = \hat{T}_n + \hat{\mathcal{H}}_e(\mathbf{r}, \mathbf{R}(t)), \quad (2.2)$$

such that:

$$[\hat{T}_n + \hat{\mathcal{H}}_e(\mathbf{r}, \mathbf{R}(t))] \Psi_I(\mathbf{r}, \mathbf{R}(t)) = E_I(\mathbf{R}(t)) \Psi_I(\mathbf{r}, \mathbf{R}(t)), \quad (2.3)$$

where the electron-nuclear wavefunctions $\Psi_I(\mathbf{r}, \mathbf{R}(t))$ can be further decomposed into electronic $\psi_I(\mathbf{r}; \mathbf{R}(t))$ and nuclear $\chi_I(\mathbf{R}(t))$ wavefunctions using the adiabatic (Born-Oppenheimer) approximation based on the large difference in mass between nuclei and electrons:

$$\Psi_I(\mathbf{r}, \mathbf{R}(t)) = \psi_I(\mathbf{r}; \mathbf{R}(t)) \chi_I(\mathbf{R}(t)), \quad (2.4)$$

leaving the electronic problem:

$$\hat{\mathcal{H}}_e(\mathbf{r}, \mathbf{R}(t))\psi_0(\mathbf{r}; \mathbf{R}(t)) = E_0(\mathbf{R}(t))\psi_0(\mathbf{r}; \mathbf{R}(t)), \quad (2.5)$$

where $\psi_0(\mathbf{r}; \mathbf{R}(t))$ is the electronic ground state with energy E_0 subject to a static external potential generated by the (positive) nuclei. The equation for the nuclei then becomes:

$$(\hat{T}_n + E_0(\mathbf{R}(t)))\chi(\mathbf{R}(t)) = E(\mathbf{R}(t))\chi(\mathbf{R}(t)). \quad (2.6)$$

2.1.1 The Ground State

The Electron Density

The scheme of Kohn, Hohenberg and Sham [1,2] for approximating the ground state of equation 2.5, commonly referred to as Density Functional Theory (DFT), has become a widespread tool to predict, model and interpret a large variety of scientific and applied problems. The central quantity in DFT is the ground state electron density:

$$\rho_0(\mathbf{r}) = N \int_{-\infty}^{+\infty} d\mathbf{r}_2^3 \cdots \int_{-\infty}^{+\infty} d\mathbf{r}_N^3 \psi_0(\mathbf{r}, \mathbf{r}_2, \dots, \mathbf{r}_N) \psi_0^*(\mathbf{r}, \mathbf{r}_2, \dots, \mathbf{r}_N), \quad (2.7)$$

where N is the number of electrons and the integrals run over $N - 1$ electronic coordinates. It has been proven that the ground state electronic wavefunction is a unique functional of the ground state electron density: $\psi_0 = \psi[\rho_0]$. It follows that the ground state expectation value of any observable O is a functional of the electron density:

$$O_0[\rho_0] = \langle \psi_0[\rho_0] | \hat{O} | \psi_0[\rho_0] \rangle, \quad (2.8)$$

including the ground state energy E_0 :

$$E_0[\rho_0] = \langle \psi_0[\rho_0] | \hat{\mathcal{H}}_e | \psi_0[\rho_0] \rangle. \quad (2.9)$$

The second Hohenberg-Kohn theorem introduces the variational principle into DFT [1], stating that every guess of the density ρ_0 and hence the wavefunction ψ_0 will yield an energy that is higher than the true ground state energy E_0 . This allows for a practical numerical scheme to minimize the ground state energy through progressive iterative 'guessing' of the density.

The Kohn-Sham Energy Functional

The main difficulty in DFT lies in finding the Kohn-Sham energy functional $E_{KS}[\rho_0]$. As the electronic problem is considered for a fixed nuclear configuration the nuclear-nuclear term is trivial and can be added as a constant. The electron-nuclear energy functional can be conveniently decomposed into a sum of single-particle potentials $v_{ext}(\mathbf{r})$:

$$E_{n-el}[\rho_0] = \langle \psi_0[\rho_0] | V_{n-el} | \psi_0[\rho_0] \rangle = \int d\mathbf{r} v_{ext}(\mathbf{r}) \rho_0(\mathbf{r}). \quad (2.10)$$

that may be seen as an external potential generated by the (positive) nuclei in which the electrons move. The complicated energy term is the electron-electron energy functional $E_{el-el}[\rho_0]$. It can be approximated classically through a Coulomb term involving the electron density $\rho(\mathbf{r})$ with the remainder being an unknown QM energy functional $E_{qm}[\rho_0]$:

$$E_{el-el}[\rho_0] = \frac{1}{2} \int d\mathbf{r}_1 \int d\mathbf{r}_2 \left[\frac{\rho(\mathbf{r}_1)\rho(\mathbf{r}_2)}{r_{12}} \right] + E_{qm}[\rho_0]. \quad (2.11)$$

Finally, the kinetic energy $T_{el}[\rho_0]$ is also non-trivial and can be approximated by summing all the kinetic energies of the Kohn-Sham orbitals $\phi_i(\mathbf{r})$ with the remainder being some unknown kinetic correlation energy $T_c[\rho_0]$:

$$T_{el}[\rho] = \sum_i^N \langle \phi_i(\mathbf{r}) | -\frac{1}{2}\nabla^2 | \phi_i(\mathbf{r}) \rangle + T_c[\rho]. \quad (2.12)$$

Exchange-Correlation Functionals

The unknown functional $E_{qm}[\rho]$ and the kinetic correlation energy $T_c[\rho]$ are together termed the exchange-correlation energy $E_{XC}[\rho]$. This functional requires approximations that are crucial to the accuracy of DFT and that are becoming ever more sophisticated. The Local Density Approximation (LDA) was one of the first to be developed and its energy functional reads:

$$E_{XC}^{LDA}[\rho] = \int \rho(\mathbf{r}) \epsilon_{XC}(\rho(\mathbf{r})) d\mathbf{r}, \quad (2.13)$$

where ϵ_{XC} is the exchange-correlation energy of a homogeneous electron gas. An improvement to this approximation came with the development of the Generalized Gradient Approximation (GGA) [3] that includes a functional dependence on the gradient of the density $\nabla\rho$:

$$E_{XC}^{GGA}[\rho, \nabla\rho] = \int f(\rho(\mathbf{r}), \nabla\rho(\mathbf{r}))d\mathbf{r}. \quad (2.14)$$

The recent accurate class of hybrid approximations combine exact Hartree Fock exchange E_X^{HF} :

$$E_X^{HF} = -\frac{1}{2} \sum_{i,j}^{occ} \int d\mathbf{r}'d\mathbf{r} \frac{\phi_i^*(\mathbf{r}')\phi_j^*(\mathbf{r})\phi_i(\mathbf{r})\phi_j(\mathbf{r}')}{|\mathbf{r} - \mathbf{r}'|}, \quad (2.15)$$

through fitted or calculated parameters (i.e. α) with any number of other exchange-correlation functionals:

$$E_{XC}^{hybrid} = \alpha E_X^{HF} + (1 - \alpha)E_{XC}^{GGA}. \quad (2.16)$$

The Kohn-Sham Equations

The conceptual step in the Kohn-Sham formalism [2] is to define an effective single-particle potential $v_{eff}(\mathbf{r})$ of a non-interacting system of electrons such that it reproduces the electron density of the true interacting system. The effective potential contains the functional derivatives of the known external and Coulomb energy terms ($v_{ext}(\mathbf{r})$ and $v_{Coul}(\mathbf{r})$) plus the unknown $v_{XC}(\mathbf{r})$ that can be approximated through the exchange-correlation functionals discussed above. The density is then constructed through the set of orbitals $\phi_i(\mathbf{r})$ that minimizes the energy functional. This leads to the Kohn-Sham equations:

$$[-1/2\nabla^2 + v_{eff}(\mathbf{r})] \phi_i(\mathbf{r}) = \epsilon_i\phi_i(\mathbf{r}) \quad (2.17a)$$

$$\sum_i^N |\phi_i(\mathbf{r})|^2 = \rho(\mathbf{r}). \quad (2.17b)$$

In practice 2.17a is solved self-consistently by generating an initial guess for the density, using the guess to calculate an effective potential $v_{eff}(\mathbf{r})$, solving 2.17a to obtain a set of orbitals ϕ_i and calculate a density from these orbitals with 2.17b that is used to start a new iteration until a predefined convergence criterion is met.

Basis sets

The molecular orbitals are constructed through linear combinations of pre-defined functions ξ_i called basis sets:

$$\phi_i(\mathbf{r}) = \sum_1^k c_{iu} \xi_u. \quad (2.18)$$

with coefficient c_{iu} and where k is the number of basisfunctions. In the ADF quantum chemical suite [4] used in this thesis the basis functions are of the Slater type:

$$\xi(\mathbf{r}) = \Upsilon_{lm} r^n e^{-\zeta r}, \quad (2.19)$$

where Υ are the spherical harmonics, l, m, n the quantum numbers and ζ determines the long-range decay of the function. The Gaussian program [5] is named after its basis functions of the contracted form:

$$\xi(\mathbf{r}) = \Upsilon_{lm} r^n \sum_1^p c_p e^{\alpha_p r^2}, \quad (2.20)$$

where c_p is the contraction coefficient corresponding to the exponent α_p . The CPMD implementation of DFT [6] uses pseudopotentials to describe the core electrons and plane waves for the valence electrons:

$$\xi(\mathbf{r}) = e^{i\mathbf{G}r}, \quad (2.21)$$

where \mathbf{G} is the wave vector. Finally, in OCTOPUS [7], a numerical grid is used where the functions are represented by values on a set of points in real-space.

2.1.2 Excited States

Linear Response Time-Dependent DFT

The most general and most rigorous formalism to approximate excited states within DFT is time-dependent DFT (TDDFT). The theoretical justification follows from the theorem of Runge and Gross [8]. Similarly to ground state DFT the Runge-Gross theorem establishes that the time-dependent single particle potential $v_{eff}(\mathbf{r}, t)$ and kinetic term $-1/2\nabla^2$ acting on the non-interacting time-dependent orbitals $\varphi_i(\mathbf{r}, t)$ uniquely define the time-dependent density $\rho(\mathbf{r}, t)$ through the time-dependent Kohn-Sham equations:

$$\left[-\frac{1}{2}\nabla^2 + v_{eff}(\mathbf{r}, t)\right] \varphi_i(\mathbf{r}, t) = i\frac{\partial}{\partial t}\varphi_i(\mathbf{r}, t) \quad (2.22a)$$

$$\sum_i^N |\varphi_i(\mathbf{r}, t)|^2 = \rho(\mathbf{r}, t). \quad (2.22b)$$

The interaction with a photon is a small perturbation to the time-dependent density. Therefore, to first order, the linear response of the density will depend only on the ground state density, which can conveniently be found from the DFT framework considered so far. The poles of the response function will consequently give the excitation energies and the pole strengths can be considered the DFT equivalents of QM oscillator strengths.

Special Cases

Several methods are also available for targeting specific excited states, such as approximating the lowest singlet excited state and charge transfer excited states.

In restricted open-shell Kohn-Sham (ROKS) the lowest excited singlet state is approximated by considering separately the closed-shell doubly occupied orbitals and the open-shell singly occupied orbitals [9,10]. This method is particularly relevant if one is interested in computationally efficient excited state dynamics of the lowest excited singlet state [11].

In constrained DFT (CDFT) [12] charge transfer energies and geometries can be assessed by constraining charges on predefined regions of the molecule. Therefore, if one has some a priori knowledge of where the photoinduced electron and hole could be localized, this method can approximate the energy of charge transfer excited states.

2.2 Methods II: Propagating the Nuclei

As a first approximation for propagating the nuclei one can neglect the quantum mechanical effects and solve Newton's second law of motion for the nuclei \mathbf{R}_I in a classical molecular dynamics framework:

$$M_I \frac{d^2 \mathbf{R}_I}{dt^2} = -\nabla V_C(\mathbf{R}_I) = F(\mathbf{R}_I), \quad (2.23)$$

where $F(\mathbf{R}_I)$ is the force acting on the nuclei due to the potential $V_C(\mathbf{R}_I)$ generated by the electrons. Usually this potential is approximated by a simple parametrized force field [e.g. 13].

2.2.1 Adiabatic Molecular Dynamics

A more sophisticated approach is called first-principles molecular dynamics (AIMD) and was pioneered by Car and Parrinello, who were the first to unify electronic structure theory in the form of DFT and molecular dynamics [14]. The basic scheme in AIMD [15,16] is to calculate the adiabatic ground state energy as the expectation value of the electronic Hamiltonian:

$$E_0 = \langle \psi_0(\mathbf{r}; \mathbf{R}(t)) | \hat{\mathcal{H}}_e | \psi_0(\mathbf{r}; \mathbf{R}(t)) \rangle. \quad (2.24)$$

Using the Hellman-Feynman theorem the force

$$F(\mathbf{R}_I) = -\nabla_I \langle \psi_0(\mathbf{r}; \mathbf{R}(t)) | \hat{\mathcal{H}}_e | \psi_0(\mathbf{r}; \mathbf{R}(t)) \rangle \quad (2.25)$$

acting on the nuclei can be calculated from the expectation value of the derivative of the electronic Hamiltonian with respect to the nuclear coordinates:

$$F(\mathbf{R}_I) = -\frac{\partial E_0}{\partial \mathbf{R}_I} = \left\langle \psi_0(\mathbf{r}; \mathbf{R}(t)) \left| -\frac{\partial \hat{\mathcal{H}}_e}{\partial \mathbf{R}_I} \right| \psi_0(\mathbf{r}; \mathbf{R}(t)) \right\rangle. \quad (2.26)$$

However, in practical numerical applications the employed basis set is incomplete and additional terms need to be calculated, the so called 'incomplete basis set correction' calculated from the gradients of the basis functions and the 'non-self consistency correction'. The equation of motion for the nuclei is:

$$\begin{aligned} M_I \frac{d^2 \mathbf{R}_I}{dt^2} &= -\nabla_I \langle \psi_0(\mathbf{r}; \mathbf{R}(t)) | \hat{\mathcal{H}}_e | \psi_0(\mathbf{r}; \mathbf{R}(t)) \rangle \\ &= -\nabla_I V_E^0(\mathbf{R}_I), \end{aligned} \quad (2.27)$$

where $V_E^0(\mathbf{R}_I)$ is the ground state multidimensional potential energy surface (PES) that maps the potential as a function of the nuclear coordinates. So far the electronic structure method was not specified. To incorporate DFT the expectation value of the electronic Hamiltonian is equated to the Kohn-Sham energy:

$$\langle \psi_0(\mathbf{r}; \mathbf{R}(t)) | \hat{\mathcal{H}}_e | \psi_0(\mathbf{r}; \mathbf{R}(t)) \rangle = E_{KS}[\{\phi_i\}], \quad (2.28)$$

where the Kohn-Sham energy functional is:

$$E_{KS}[\{\phi_i\}] = T_{el}[\{\phi_i\}] + \int d\mathbf{r} V_{ext}(\mathbf{r})\rho(\mathbf{r}) + \frac{1}{2} \int d\mathbf{r} V_H(\mathbf{r})\rho(\mathbf{r}) + E_{XC}[\rho]. \quad (2.29)$$

The usual algorithm for propagating the nuclei in AIMD is the velocity Verlet:

$$\begin{aligned} \mathbf{x}(t + \Delta t) &= \mathbf{x}(t) + \mathbf{v}(t)\Delta t + \frac{1}{2}\mathbf{a}(t)\Delta t^2 \\ \mathbf{v}(t + \Delta t) &= \mathbf{v}(t) + \frac{\mathbf{a}(t) + \mathbf{a}(t + \Delta t)}{2}\Delta t, \end{aligned} \quad (2.30)$$

where $\mathbf{x}(t)$ represents a position vector, $\mathbf{v}(t)$ the velocity and $\mathbf{a}(t)$ acceleration. The typical timestep Δt used in this thesis is 0.1 fs and most simulations are performed with a thermostat in a canonical NVT ensemble.

2.2.2 Nonadiabatic Molecular Dynamics

In first-principles molecular dynamics the nuclear motion takes place on a single adiabatic potential energy surface, the ground state. Nonadiabatic dynamics is a generalization of this principle for multiple adiabatic states, including the transitions between states. A general strategy for this in the Schrödinger picture of QM is to construct the total time-dependent *electronic* wavefunction $\psi(\mathbf{r}, t)$ from a basis of adiabatic functions [17]:

$$\psi(\mathbf{r}, t) = \sum_i c_i(t)\psi_i(\mathbf{r}; \mathbf{R}(t)), \quad (2.31)$$

where $c_i(t)$ are the time-dependent coefficients. Substituting this expansion into the time-dependent Schrödinger equation for the electrons:

$$i \frac{\partial \psi(\mathbf{r}, t)}{\partial t} = \hat{\mathcal{H}}_e \psi(\mathbf{r}, t) \quad (2.32)$$

and by projecting both sides of the resulting expression onto the set $\Psi_j(\mathbf{r}, \mathbf{R}(t))$, the following equation for the time-dependent coefficients $c_j(t)$ is obtained [17]:

$$i \frac{\partial c_j(t)}{\partial t} = \left[\hat{\mathcal{H}}_{ji}(\mathbf{r}, \mathbf{R}(t)) - i \left\langle \psi_j(\mathbf{r}; \mathbf{R}(t)) \left| \frac{\partial \psi_i(\mathbf{r}; \mathbf{R}(t))}{\partial t} \right. \right\rangle \right] c_i(t), \quad (2.33)$$

where the electronic Hamiltonian matrix elements between state j and i are:

$$\hat{\mathcal{H}}_{ji}(\mathbf{r}, \mathbf{R}(t)) = \langle \Psi_j(\mathbf{r}; \mathbf{R}(t)) | \hat{\mathcal{H}}_e(\mathbf{r}, \mathbf{R}(t)) | \Psi_i(\mathbf{r}, \mathbf{R}(t)) \rangle. \quad (2.34)$$

The nonadiabatic coupling between adiabatic state functions is contained in the second term between brackets in 2.33, which can easily be seen by using the chain rule:

$$\mathbf{d}_{ji}(\mathbf{r}, \mathbf{R}(t)) = \langle \psi_j(\mathbf{r}; \mathbf{R}(t)) | \nabla_{\mathbf{R}} \psi_i(\mathbf{r}; \mathbf{R}(t)) \rangle \cdot \frac{d\mathbf{R}}{dt}, \quad (2.35)$$

Thus, in this framework there are essentially two terms that promote transitions, the off-diagonal Hamiltonian matrix elements $\hat{\mathcal{H}}_{ji}(\mathbf{r}, \mathbf{R}(t))$ and the nonadiabatic coupling $\mathbf{d}_{ji}(\mathbf{r}, \mathbf{R}(t))$. As discussed in the introduction the process of interest in this thesis is the evolution of a pure exciton state ($c_{ex}(0) = 1$) into a charge transfer state ($c_{ct}(\tau) = 1$). To achieve this some nuclear motion is required, as $\hat{\mathcal{H}}_{ji}(\mathbf{r}, \mathbf{R}(t))$ and $\mathbf{d}_{ji}(\mathbf{r}, \mathbf{R}(t))$ will only change in time through their dependence on $\mathbf{R}(t)$.

Tully's Surface Hopping

A commonly used algorithm to approximate this time-dependent problem was developed by Tully [18]. In Tully's nonadiabatic dynamics the nuclear motion takes place on a single potential energy surface, while evolving multiple adiabatic states simultaneously. The nonadiabatic coupling between all states is evaluated along the trajectories to calculate transition probabilities. If the probability reaches above a certain threshold generated by a random number, the algorithm will invoke an instantaneous nonadiabatic transition between states. Although this method is accurate in describing equilibrium behaviour on long timescales [19], the description of gradual coherent charge transfer from an excitonic state to a charge transfer state is

limited by the instantaneous nature of the transitions in this framework. Recent experimental and theoretical work indicates that the oscillatory charge transfer process has an associated nonzero timescale and involves a mixing of adiabatic states.

Ehrenfest TDDFT

In Ehrenfest dynamics, the electronic motion originates directly from solving the time-dependent electronic Schrödinger equation for the time-dependent electronic wavefunction $\psi(\mathbf{r}, t)$.

$$i\frac{\partial\psi(\mathbf{r}, t)}{\partial t} = \hat{\mathcal{H}}_e\psi(\mathbf{r}, t). \quad (2.36)$$

Consequently, for every newly obtained electronic wavefunction $\psi(\mathbf{r}, t+\Delta t)$, where Δt is very small ($\sim 10^{-18}s$) forces can be calculated to evolve the nuclei according to:

$$M_I\frac{d^2\mathbf{R}_I}{dt^2} = -\nabla_I\langle\psi(\mathbf{r}, t) | \hat{\mathcal{H}}_e | \psi(\mathbf{r}, t)\rangle, \quad (2.37)$$

which includes nonadiabatic transitions and the possibility of mixing between (adiabatic) states. In this way coherent evolution of an exciton into a charge transfer state can be simulated in real-time.

The implementation of the Ehrenfest formalism within TDDFT is through the time-dependent Kohn-Sham equations that give the time evolution of the time-dependent Kohn-Sham orbitals $\phi_i(\mathbf{r}, t)$ and the time dependent density $\rho(\mathbf{r}, t)$:

$$i\frac{\partial}{\partial t}\varphi_i(\mathbf{r}, t) = [-1/2\nabla^2 + v_{eff}(\mathbf{r}, t)]\varphi_i(\mathbf{r}, t)$$

$$\sum_i^N |\varphi_i(\mathbf{r}, t)|^2 = \rho(\mathbf{r}, t). \quad (2.38)$$

The time-dependent Kohn-Sham orbitals $\varphi_i(\mathbf{r}, t)$ can subsequently be expanded in terms of adiabatic Kohn-Sham orbitals $\phi_i(\mathbf{r}; \mathbf{R}(t))$:

$$\varphi(\mathbf{r}, t) = \sum_i c_i(t)\phi_i(\mathbf{r}; \mathbf{R}(t)), \quad (2.39)$$

that are obtained through a regular time-independent DFT optimization (section 2.1). The time evolution of the coefficients then becomes [20]:

$$i \frac{\partial c_i(t)}{\partial t} = \sum_j c_j(t) (\epsilon_j \delta_{ij} - \mathbf{d}_{ij}), \quad (2.40)$$

where ϵ_j is the energy of adiabatic orbital j and \mathbf{d}_{ij} the nonadiabatic coupling $\langle \phi_i(\mathbf{r}; \mathbf{R}(t)) | \nabla_{\mathbf{R}} | \phi_j(\mathbf{r}; \mathbf{R}(t)) \rangle \cdot d\mathbf{R}/dt$ between orbital i and j .

As in adiabatic dynamics, the classical equation of motion for the nuclei follows from the time derivative of the Kohn–Sham energy functional:

$$M_I \frac{d^2 \mathbf{R}_I}{dt^2} = - \frac{\partial E_{KS}[\rho(\mathbf{r}, t)]}{\partial \mathbf{R}_I}. \quad (2.41)$$

Now, by modifying the nonadiabatic coupling \mathbf{d}_{ij} between adiabatic orbitals the nuclear motion can invoke nonadiabatic transitions. Thus, a framework is in place to approximate in real-time the photoinduced charge transfer in molecules.

2.3 References

- [1] P. Hohenberg, W. Kohn, Inhomogeneous Electron Gas, *Physical Review*, **1964**, 136, 864.
- [2] W. Kohn, L. J. Sham, Self-Consistent Equations Including Exchange and Correlation Effects, *Physical Review*, **1965**, 140, 1133.
- [3] J. P. Perdew, K. Burke, and M. Ernzerhof, Generalized gradient approximation made simple, *Phys. Rev. Lett.*, **1997**, 78, 1396.
- [4] ADF2012, SCM, Theoretical Chemistry, Vrije Universiteit, Amsterdam, The Netherlands, <http://www.scm.com/>.
- [5] M. J. Frisch, et al., Gaussian 09, Revision D.01; Gaussian, Inc.: Wallingford CT, **2009**.
- [6] CPMD v3.11.1, Copyright IBM Corp, 1990–2008; Copyright MPI für Festkörperforschung Stuttgart, 1997–2001; <http://www.cpmd.org/>.
- [7] H. Castro, M. O. Appel, C.A. Rozzi, X. Andrade, F. Lorenzen, M.A.L. Marques, E.K.U. Gross, and A. Rubio, "Octopus: A tool for the application of time-dependent density functional theory", *Phys. Stat. Sol. B*, **2006**, 243, 2465–2488.
- [8] E. Runge and E. K. U. Gross, Density-Functional Theory for Time-Dependent Systems, *Phys. Rev. Lett*, **1984**, 52 (12), 997–1000.
- [9] F. Irmgard, J. Hütter, D. Marx and M. Parrinello, Molecular dynamics in low-spin excited states, *The Journal of chemical physics*, **1998**, 108, 4060–4069.

- [10] M. Filatov, S. Shaik, Spin-restricted density functional approach to the open-shell problem, *Chemical Physics Letters*, **1998**, 288, 689-697.
- [11] N. L. Doltsinis and D. Marx, Nonadiabatic Car-Parrinello Molecular Dynamics, *Physical Review Letters*, **2002**, 88, 166402.
- [12] Wu, Q.; Van Voorhis, T. Direct Optimization Method to Study Constrained Systems Within Density-functional Theory. *Phys. Rev. A* **2005**, 72, 024502.
- [13] D.A. Case et al., AMBER 14, **2014**, University of California, San Francisco.
- [14] R. Car, M. Parrinello, "Unified Approach for Molecular Dynamics and Density-Functional Theory", *Phys. Rev. Lett.*, **1985**, 55, 2471.
- [15] F. Buda, Introduction to theory/modeling methods in photosynthesis, *Photosynthesis Research*, **2009**, 102, 437-441.
- [16] Marx, D.; Hütter, J. Ab Initio Molecular Dynamics: Basic Theory and Advanced Methods; Cambridge University Press: Cambridge, U.K., 2009.
- [17] A. V. Akimov, A. J. Neukirch and O. V. Prezhdo, Theoretical Insights into Photoinduced Charge Transfer and Catalysis at Oxide Interfaces, *Chemical Reviews*, **2013**, 6, 4496.
- [18] J. C. Tully, Molecular Dynamics with Electronic Transitions, *The Journal of Chemical Physics*, **1990**, 93, 1061.
- [19] J. C. Tully, Perspective: Nonadiabatic Dynamics Theory, *J. Chem. Phys.*, **2012**, 137, 22301.
- [20] W. R. Duncan and O. V. Prezhdo, Nonadiabatic Molecular Dynamics Study of Electron Transfer from Alizarin to the Hydrated Ti^{4+} Ion, *J. Phys. Chem. B*, **2005**, 109, 17998-18002.

Chapter 3

Efficient Evolution of Excitons into Charge Transfer States

3.0.1 ABSTRACT

Using first-principles molecular dynamics, we predict the reaction coordinate and mechanism of the first charge-transfer step in the reaction center of photosynthetic bacteria in a model including the special pair (P) and closest relevant residues. In the ground state, a dynamic localization of the highest occupied orbital is found to be a defining characteristic of P . This feature is linked to the tuning of the orbital energy levels by the coupling with two collective low-frequency vibrational modes. After electronic excitation, one specific mode coherently couples to P^* , representing the reaction coordinate along which the excited state develops. This characteristic vibrational coordinate represents the rotation of an axial histidine (HisM202), which selectively lowers the energy of one (P_M) of the two bacteriochlorophylls in P . This leads to an efficient and coherent evolution of $P_L^+P_M^-$ charge-transfer character, as the precursor of the full charge separated state $P^+B_A^-$.

Parts of this chapter were published in:

T. J. Eisenmayer, H. J. M. de Groot, E. van de Wetering, J. Neugebauer, F. Buda, "Mechanism and Reaction Coordinate of Directional Charge Separation in Bacterial Reaction Centers", *Journal of Physical Chemistry Letters*, 2012, 3, pp 694-697.
DOI: 10.1021/jz201695p

3.1 Introduction

In the pseudo-symmetric architecture of photosynthetic reaction centers (*RCs*), charge separation occurs preferentially along one (*A*) of two cofactor branches. Numerous experiments find vibrational modes in the region $100\text{--}150\text{ cm}^{-1}$ that coherently couple to the initial photo-excited state of the special pair (P^*) [1-4].

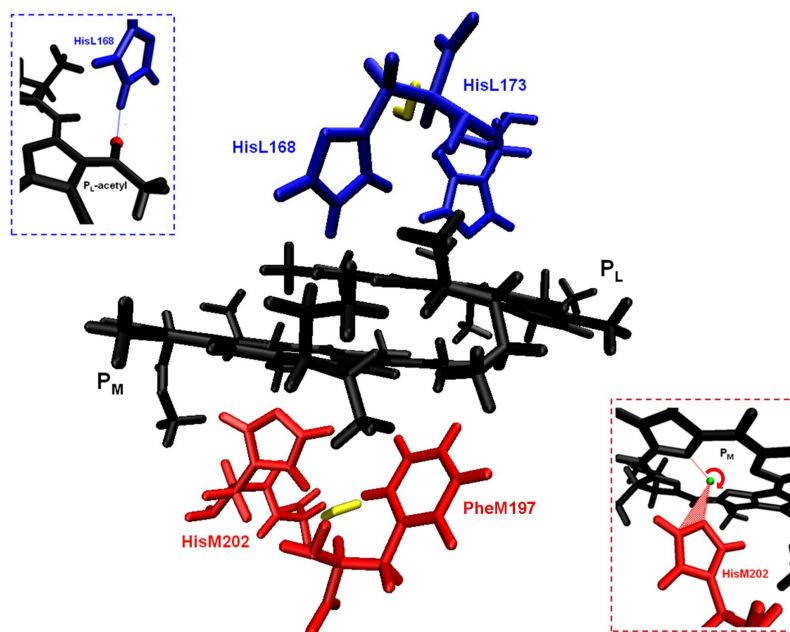


Figure 3.1: Model of the special pair and direct surroundings, including the axially coordinated histidines HisL173, HisM202, the water molecules in their vicinity, and the residues HisL168 and PheM197. The protein environment mechanical constraints are ensured by fixing the tails of the histidines, the phenylene, and the truncated phytol chains. Left top: hydrogen bond between HisL168 and the acetyl oxygen of the P_L dimer half. Right bottom: dihedral angle of the histidine ring of HisM202 with respect to the Mg-N_τ coordination axis.

On a 3 ps time scale the primary electron donor is oxidized and an accessory bacteriochlorophyll (B_A) is reduced [5]. Stark experiments find an internal charge transfer (CT) character state $P_L^+P_M^-$ to have strong influence on P^* [6]. The ground-state electron density distribution of

P and of the radical cation $P^{\bullet+}$ is influenced by the immediate protein environment as indicated by solid-state NMR, ENDOR/EPR and density functional calculations [7,8]. The axial histidines are known to donate electron charge to bacteriochlorophyll chromophores both in reaction centers and light-harvesting complexes, and the acetyl groups conformation tunes the energy of the π -conjugated bacteriochlorophyll planes [9,10]. *Ab-initio* molecular dynamics (AIMD) simulations [11,12] have been performed at room temperature of a model including the special pair and the relevant closest protein environment (Figure 3.1). Long range interactions are not included in the model, but the chosen residues are thought to be sufficient to capture the most important effects for the local dynamics. Within this approach the dynamics of the nuclear coordinates is coupled to the corresponding electronic structure rearrangement calculated with density functional theory (DFT). This allows us to predict the reaction coordinate of coherent charge separation and the mechanism leading to the first charge transfer (CT) intermediate.

The AIMD simulations have been performed using the Car-Parrinello method [11,12] as implemented in the CPMD code [13]. The BLYP functional is used for the exchange-correlation energy [14]. The Kohn-Sham orbitals are expanded in a plane-wave basis set with a kinetic energy cutoff of 70 Ry and dispersion corrected atom-centered (DCACP) pseudopotentials [15] are used. For the excited state dynamics the restricted open-shell Kohn-Sham (ROKS) formalism [12] is applied. For the normal mode analysis and for single point calculations at selected snapshots along the AIMD trajectories I used the ADF code [16]. Also time dependent DFT (TDDFT) calculations have been performed using the ADF code for a selected set of configurations along the dynamical trajectories to evaluate the first excitation energies. Although TDDFT with standard GGA functionals suffers from the well known poor description of charge transfer character excitations, this analysis shows that the first excitation has a dominant HOMO to LUMO transition character. This finding justifies the use of the ROKS approach where only the HOMO to LUMO transition is taken into account to evaluate the excited state dynamics. Two AIMD ground state simulations have been performed of about 1 ps each starting from two sets of initial coordinates for our model taken from the X-ray crystallographic data of wild type [17] and R-26 mutant [18] *Rhodobacter Sphaeroides* reaction centers, respectively. The results presented in Figure 3.2 and 3.3 are obtained from the first trajectory using the wild type initial conditions. I verified that the trajectory generated from the R-26 mutant initial coordinates shows a pic-

ture consistent with the first trajectory. The ground state and excited state ROKS dynamics presented in Figure 3.4 are based on the R-26 initial conditions, while the inset of Figure 3.4 comes from the wild type model. The effect of long-range electrostatic interactions has been tested on a few snapshots along the trajectories by including a conductor like screening model (COSMO) using the ADF code with the same BLYP functional used in the AIMD simulations and a triple zeta with polarization basis set (TZP). A dielectric constant of 5 (a typical value in a protein environment) has been considered for this test. The relative energies of different configurations treated with and without the solvent model are well within 1 kcal/mol, thus confirming that the shape of the potential energy surface and therefore the force acting on the nuclei is not significantly modified by long range effects of the environment.

3.2 The Ground State

The ground state trajectories show that frontier orbital (HOMO-LUMO) localization is a dynamic characteristic of the special pair at room temperature (Figure 3.2).

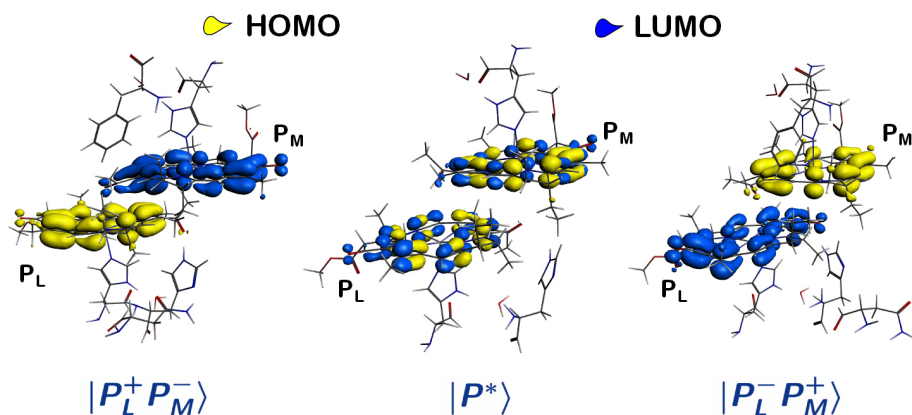


Figure 3.2: Frontier orbital localization for different snapshots along the trajectory. The HOMO fluctuates from localization on P_L (left) to a delocalized state (middle) to localization on P_M (right). Note that the LUMO shows the exact opposite behaviour, which leads to the CT character.

On a 1 ps timescale the HOMO fluctuates from complete localization on one dimer half to a delocalized state to complete localization on the other

dimer half. The LUMO shows the same dynamical behaviour with opposite phase; when the HOMO is localized on P_M the LUMO is localized on P_L and vice versa. This result can be interpreted by thermally induced orbital energy fluctuations of the two monomers: When the HOMO energy of P_L is lower than the HOMO energy of P_M , the HOMO of P shows an essentially monomeric character being localized entirely on P_L ; when the orbital energies of the monomers are very similar, the HOMO is delocalized. HOMO-LUMO photoexcitation of P at specific geometries will thus yield an excited state with strong CT character. We find both $P_L^+P_M^-$ and $P_L^-P_M^+$ CT characters to be present at room temperature as well as a delocalized pure exciton state P^* . Comparing the relative HOMO-LUMO gap of $P_L^+P_M^-$ and $P_L^-P_M^+$ transitions it is shown, in agreement with Stark experiments [6], that $P_L^+P_M^-$ is the lowest energy CT transition of the P absorption band. The dynamic picture (Figure 3.2) and the occurrence of excitations with different character (P^* , $P_L^+P_M^-$ and $P_L^-P_M^+$) gives insight into the homogeneous broadening of the P absorption band and provides an explanation for its red shift at low temperatures. Going to low temperature the structural fluctuations are quenched as the system freezes gradually. This will eliminate the higher energy transitions in the absorption spectrum of P and leave the pure exciton transition with some $P_L^+P_M^-$ charge transfer character to dominate the band and red-shift the absorption maximum at low temperature. The HOMO is preferentially localized on P_L . Upon photo-oxidation of P the unpaired electron is assumed to be removed from the HOMO leading to a net spin density. Both NMR and ENDOR techniques measure a spin density distribution on bacterial RCs in the charge-separated radical cation $P^{\bullet+}$ state delocalized over the dimer with a 2:1 ration between P_L and P_M [19-20].

The thermal rearrangement of electron density over P opens the possibility to correlate electronic structure with distinct conformational dynamics, i.e. to find the normal modes of P that couple to orbital localization. Fourier transformation of the velocity autocorrelation function of the trajectories gives a vibrational density of states that shows two distinct maxima at low frequencies, $\sim 50 \text{ cm}^{-1}$ and $\sim 100 \text{ cm}^{-1}$ (Figure 3.3, grey shading in top graphs). To assign the peaks and resolve the appropriate conformational dynamics additional Fourier transforms of the autocorrelation function of different components of the model and of individual structural parameters (e.g. dihedral angles and bond distances) were performed. The lowest frequency peak at $\sim 50 \text{ cm}^{-1}$ is well resolved in terms of the out-of-plane acetyl motion that couples strongly to the HisL168 imidazole ring dynamics

through hydrogen bonding interaction (see Figure 3.1, left top and Figure 3.3, blue lines). This is the characteristic vibrational coordinate of the mode, which is biased towards the P_L dimer half also absorbing at this frequency (see Figure 3.3, middle top inset, where the contribution of the two dimer halves is considered separately). To correlate the vibrational coordinate with the electronic structure, the energies of the HOMO and HOMO-1 along the trajectory are associated to either the P_L or P_M dimer half depending on their localization. The left bottom graph of Figure 3.3 shows the correlation between the P_L -HOMO energy (bars) and the hydrogen bond distance from the P_L -acetyl to the HisL168 with a computed Pearson correlation coefficient $\rho_c = 0.64$; at minimum distance, the hydrogen bond is strongest and stabilizes the P_L -HOMO energy.

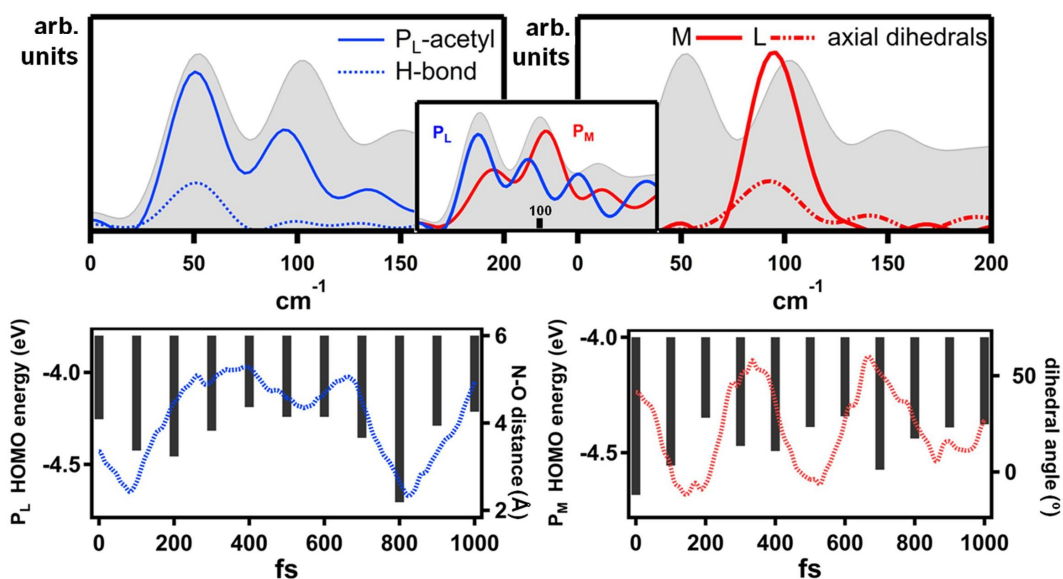


Figure 3.3: Total vibrational density of states (VDOS) obtained from the dynamical trajectory (grey shading top graphs). Blue lines in the top left represent conformational dynamics of the $\sim 50 \text{ cm}^{-1}$ mode obtained from the time evolution of the hydrogen bond with HisL168 and of the P_L -acetyl group. The inset gives the VDOS for P_L in blue. The bottom left graph gives the hydrogen bond distance (blue line) with the P_L -HOMO energy (bars) in the time domain. Red lines represent conformational dynamics of the $\sim 100 \text{ cm}^{-1}$ mode, top right graph gives the VDOS obtained from the axial histidine dihedrals and the inset the VDOS for P_M . The bottom right graph gives the HisM202 dihedral (red line) with the P_M -HOMO energy (bars) in the time domain.

In a separate calculation the Hessian matrix is diagonalized for the same model to analyze the normal modes. This calculation is performed using the Becke-Perdew functional. In agreement with the dynamical data the normal modes around $\sim 50 \text{ cm}^{-1}$ are asymmetrically delocalized over P with an emphasis on P_L and with most of the amplitude along the characteristic vibrational coordinate represented by the concerted motion of the P_L -acetyl and the HisL168. In- and out-of-plane rotation of the acetyl group with respect to the bacteriochlorophyll macrocycle is well known to modulate the conjugated π -system [10]. The underlying structural cause for the $\sim 50 \text{ cm}^{-1}$ mode to be dominated by the P_L -half acetyl group is that its symmetry-related counterpart on P_M acts as a sixth ligand to the Mg of P_L , inhibiting its free rotation. The average Mg-O^{acetyl} distances confirm this; the P_M acetyl group is $\sim 1 \text{ \AA}$ closer to the Mg on P_L 'locking' it into coordination.

Equally pronounced in the total vibrational density of states is a peak at $\sim 100 \text{ cm}^{-1}$ that is mostly localized on the P_M half of the dimer (Figure 3.3; inset, red line). Analysis of the structural dynamics showed an intriguing anti-correlated rotation of the two axial histidines with respect to the coordination Mg-N $_{\tau}$ axis (illustrated by the inset in Figure 3.4; left top) expressed in terms of dihedral angles (see Figure 3.1 inset; right bottom). Calculations of covariance between the L - and M -side axial histidines ($\rho_c = -0.81$) confirm this behaviour yielding values a factor of 2 to 4 larger than the negative covariance between the L and M bacteriochlorophyll planes. From the Fourier analysis both dihedral angles are found to contribute to the $\sim 100 \text{ cm}^{-1}$ mode, with the M -side dihedral showing larger amplitude (see Figure 3.3, top right, red lines). The normal mode analysis clearly confirms this picture; the modes around $\sim 100 \text{ cm}^{-1}$ contain an anti-correlated rotation of the axial histidines with respect to the Mg-N $_{\tau}$ axis, the amplitude being larger on the M -side. In conclusion, the characteristic vibrational coordinate of the $\sim 100 \text{ cm}^{-1}$ mode involves mostly the P_M dimer half and the axial rotation of the HisM202. The bottom right graph of figure 3.3 shows the dihedral angle of HisM202 (red line) with the energy of the P_M -HOMO (bars) along the trajectory. Minima at 0, 350 and 700 fs in the energy of the P_M -HOMO correspond to maxima in the dihedral angle revealing that these quantities are anti-correlated ($\rho_c = -0.50$). The ground state multidimensional configurational space along which the relative energies of P_L and P_M are modulated is thus essentially given by two collective coordinates with well defined frequencies ($\sim 50 \text{ cm}^{-1}$ and $\sim 100 \text{ cm}^{-1}$). Displacements along these coordinates changes the localization

of the frontier orbitals.

3.3 The Excited State

To explore the dynamics in the excited state (P^*) a molecular dynamics simulation based on the restricted open-shell Kohn-Sham (ROKS) approach [12] has been performed starting from the previously equilibrated ground state trajectory. The use of ROKS is justified given the dominant HOMO-LUMO character of the excitation. By comparing the ground state and the ROKS trajectories a distinct conformational change induced by the photo-excitation is apparent. This is illustrated in figure 3.4, showing the dihedral angles of the rotation of the axial histidines around the $Mg-N_\tau$ axis. In the ground state a striking negative covariance between the rotations of the two histidines was found (see also the inset in Figure 3.4).

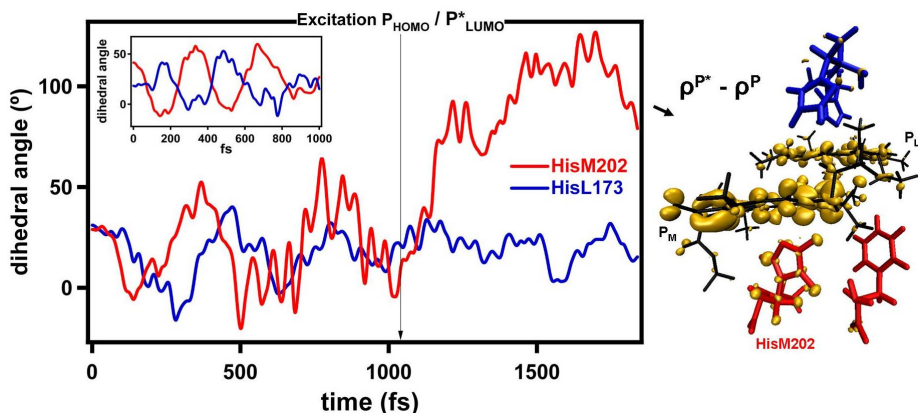


Figure 3.4: HisM202 (red line) and symmetry related HisL173 (blue line) dihedral angles representing the rotation of the histidine rings around the coordination $Mg - N_\tau$ axis as a function of time (see also Figure 3.1, right bottom). The arrow indicates the time step of the switch from ground state to excited state (ROKS) dynamics. In the inset for comparison the same structural parameters along a different ground state trajectory. The right figure shows the positive values of the difference between the P^* and P electron density ($\rho^{P^*} - \rho^P$) at the end of the ROKS dynamics.

After photo-excitation the dihedral angle of HisM202 (red line), that was found to be characteristic of the vibrational coordinate of the $\pm 100 \text{ cm}^{-1}$) mode, increases from an average of $\sim 25^\circ$ in the ground state to $\sim 80^\circ$ in

P^* and the negative covariance is lost. The vibrational coordinate of the $\pm 50 \text{ cm}^{-1}$ mode is not affected upon photo-excitation. In conclusion, upon photo-excitation P couples selectively to the $\pm 100 \text{ cm}^{-1}$ mode which I propose is the same mode seen in resonance Raman studies (96 cm^{-1}), [22] in femtosecond absorption spectroscopy (94 cm^{-1}) [3], and possibly hole-burning studies ($\sim 150 \text{ cm}^{-1}$) [4]. To check the effect of the dynamics on the evolution in the excited state and the electron density distribution the difference between the excited state and ground state electron density for selected snapshots along the ROKS dynamics is considered. In Figure 3.4 (right) the positive values of $\rho^{P^*} - \rho^P$ are plotted. Electron density moves from P_L to P_M and onto the HisM202 in agreement with experimental findings that P^* is dominated by a $P_L^+ P_M^-$ CT character [6,23].

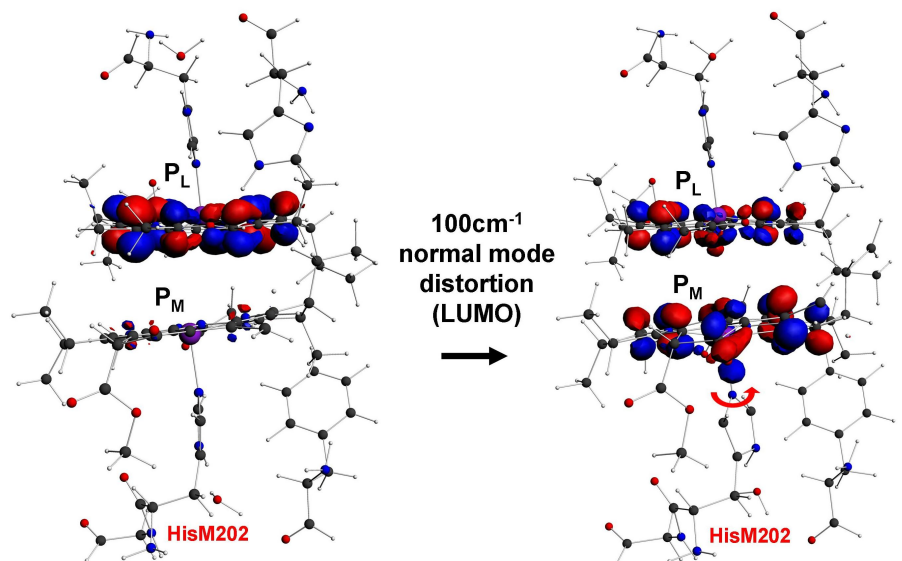


Figure 3.5: LUMO redistribution as a function of a displacement along the 100 cm^{-1} normal mode resulting in a rotation of the HisM202 around the coordination Mg- N_τ axis from 5° (left) to 50° (right).

To confirm that the excited state electron density redistribution is due to the coupling of the excited state with the discussed 100 cm^{-1} mode, I show in Figure 3.5 how the LUMO is redistributed by a displacement along this normal mode. The amplitude of the displacement is chosen such that the

HisM202 dihedral angle – representative of the rotation of the histidine around the coordination Mg-N_τ axis – increases from 5° to 50°. This confirms that the reaction coordinate, even starting from a $P_L^- P_M^+$ CT configuration, leads to a $P_L^+ P_M^-$ intermediate state through the coupling of P^* to the 100 cm⁻¹ mode resulting in an increase of the dihedral angle and initiating a directional displacement of electron density. From the Moser-Dutton simplification, the donor-acceptor distance is the rate-defining variable in most biological electron-transfer reactions [24,25]. In the bacterial RC, where competing electron-transfer pathways have similar distances, the reaction coordinate – as identified in this work – displaces electron density asymmetrically, possibly increasing the electronic coupling with one (B_A) of the two accessory bacteriochlorophylls. Additional investigations with an extended model including the electron acceptor are needed to support this suggestion (see Chapter 4).

3.4 Conclusions

In conclusion, the ground state electron density is continuously redistributed by thermally excited low frequency collective modes (~ 50 cm⁻¹ and ~ 100 cm⁻¹) that tune the respective dimer halves energies and induce the thermal broadening of P . Upon photo-excitation the excited state P^* specifically couples to the ~ 100 cm⁻¹ mode that lowers the P_M dimer half energy and effectively modulates the barrier for charge separation allowing a coherent displacement of electron density towards a $P_L^+ P_M^-$ charge transfer intermediate. Thus, I have structurally characterized the nuclear motion that drives the efficient charge separation in bacterial reaction centers. Further nonadiabatic, excited state dynamics would be needed to directly observe the oscillatory evolution of charge transfer character in combination with, for example, two-dimensional electronic spectroscopy.

3.5 References

- [1] Novoderezhkin, V.; Yakovlev, A.; van Grondelle, R.; Shuvalov, V. Coherent Nuclear and Electronic Dynamics in Primary Charge Separation in Photosynthetic Reaction Centers: A Redfield Theory Approach. *J. Phys. Chem. B* 2004, 108, 7445-7457.
- [2] Vos, M. H.; Jones, M. R.; Hunter, C. N.; Breton, J.; Martin, J. L. Coherent Nuclear Dynamics at Room Temperature in Bacterial Reaction Centers. *Proc. Natl. Acad. Sci. U.S. A.* 1994, 91, 12701- 12705.

3.5. REFERENCES

- [3] Rischel, C.; Spiedel, D.; Ridge, J. P.; Jones, M. R.; Breton, J.; Lambry, J. C.; Martin, J. L. Low Frequency Vibrational Modes in Proteins: Changes Induced by Point-Mutations in the Protein- Cofactor Matrix of Bacterial Reaction Centers. *Proc. Natl. Acad. Sci. U.S.A.* 1998, 95, 12306-12311.
- [4] Reddy, N. R. S.; Kolaczowski, S. V.; Small, G. J. A Photoinduced Persistent Structural Transformation of the Special Pair of a Bacterial Reaction Center. *Science* 1993, 260, 68-71.
- [5] Holzzapfel, W.; Finkle, U.; Kaiser, W.; Oesterhelt, D.; Scheer, H.; Stolz, H. U.; Zinth, W. Initial Electron-Transfer in the Reaction Center from Rhodobacter Sphaeroides. *Proc. Natl. Acad. Sci. U.S.A.* 1990, 87, 5168-5172.
- [6] Moore, L. J.; Zhou, H.; Boxer, S. G. Excited-State Electronic Asymmetry of the Special Pair in Photosynthetic Reaction Center Mutants: Absorption and Stark Spectroscopy. *Biochemistry* 1999, 38, 11949-11960.
- [7] Daviso, E.; Prakash, S.; Alia, A; Gast, P.; Neugebauer, J.; Jeschke, G.; Matysik, J. The Electronic Structure of the Primary Electron Donor of Reaction Centers of Purple Bacteria at Atomic Resolution As Observed by Photo-CIDNP ¹³C NMR. *Proc. Natl. Acad. Sci. U. S. A.* 2009, 106, 22281-22286.
- [8] Johnson, E. T.; Mu, F.; Nabedryk, E.; Williams, J. C.; Allen, J. P.; Lubitz, W.; Breton, J.; Parson, W. W. Electronic and Vibronic Coupling of the Special Pair of Bacteriochlorophylls in Photosynthetic Reaction Centers from Wild-Type and Mutant Strains of Rhodobacter Sphaeroides. *J. Phys. Chem. B* 2002, 106, 11859-11869.
- [9] Alia, Wawrzyniak, P. K.; Janssen, G. J.; Buda, F.; Matysik, J.; de Groot, H. J. M. Differential Charge Polarization of Axial Histidines in Bacterial Reaction Centers Balances the Asymmetry of the Special Pair. *J. Am. Chem. Soc.* 2009, 131, 9626-9627.
- [10] Wawrzyniak, P. K.; Beerepoot, M. T. P.; de Groot, H. J. M.; Buda, F. Acetyl Group Orientation Modulates the Electronic Ground- State Asymmetry of the Special Pair in Purple Bacterial Reaction Centers. *Phys. Chem. Chem. Phys.* 2011, 13, 10270-10279.
- [11] Car, R.; Parrinello, M. Unified Approach for Molecular Dynamics and Density-Functional Theory. *Phys. Rev. Lett.* 1985, 55, 2471-2474.
- [12] Marx, D.; Hütter, J. *Ab Initio Molecular Dynamics: Basic Theory and Advanced Methods*; Cambridge University Press: Cambridge, U.K., 2009.
- [13] CPMD v3.11.1, Copyright IBM Corp, 1990-2008; Copyright MPI für Festkörperforschung Stuttgart, 1997-2001; <http://www.cpmd.org/>.
- [14] a) A.D. Becke, *Phys. Rev. A* 1988, 38, 3096; b) C.T. Lee, W.T. Yang, R.G. Parr, *Phys. Rev. B* 1988, 37, 785.
- [15] a) O.A. von Lilienfeld, I. Tavernelli, U. Röthlisberger, D. Sebastiani, *Phys. Rev. Lett.* 2004, 93, 153004; b) O.A. von Lilienfeld, I. Tavernelli, U. Röthlisberger, D. Sebastiani, *Phys. Rev. B* 2005, 71, 195119.

- [16] ADF2010, SCM, Theoretical Chemistry, Vrije Universiteit, Amsterdam, The Netherlands, [http:// www.scm.com/](http://www.scm.com/).
- [17] U. Ermler, G. Fritzsche, S.K. Buchanant, H. Michel, *Structure* 1994, 2, 925-936.
- [18] M.H. Stowell, T.M. McPhillips, D.C. Rees, S.M. Soltis, E. Abresch, G. Feher, *Science* 1997, 276, 812-816.
- [19] E. Daviso, S. Prakash, A. Alia, P. Gast, J. Neugebauer, G. Jeschke, J. Matysik, *Proc. Natl. Acad. Sci. U. S. A.* 2009, 106, 22281-22286.
- [20] E. T. Johnson, F. Mu, E. Nabadryk, J.C. Williams, J.P. Allen, W. Lubitz, *J. Phys. Chem. B* 2002, 106, 11859-11869.
- [21] Cohen Stuart, T.; van Grondelle, R. Multipulse Spectroscopy on the Wild-Type and YM210W Bacterial Reaction Centre Uncovers a New Intermediate State in the Special Pair Excited State. *Chem. Phys. Lett.* 2009, 474, 352-356.
- [22] Cherepy, N. J.; Shreve, A. P.; Moore, L. J.; Boxer, S. G.; Mathies, R. A. Temperature Dependence of the Q_y Resonance Raman Spectra of Bacteriochlorophylls, the Primary Electron Donor, and Bacteriopheophytins in the Bacterial Photosynthetic Reaction Center. *Biochemistry* 1997, 36, 8559-8566.
- [23] Shuvalov, V.; Yakovlev, A. Coupling of Nuclear Wavepacket Motion and Charge Separation in Bacterial Reaction Centers. *FEBS Lett.* 2003, 540, 26-34.
- [24] Moser, C. C.; Keske, J. M.; Warncke, K; Farid, R. S.; Dutton, L. P. Nature of Biological Electron Transfer. *Nature* 1992, 355, 796-802.
- [25] Creighton, S.; Hwang, J. K.; Warshel, A; Parson, W. W.; Norris, J. Simulating the Dynamics of the Primary Charge Separation Process in Bacterial Photosynthesis. *Biochemistry* 1988, 27, 774-781.

Chapter 4

Stable Charge Separation through Proton Displacements

4.0.1 ABSTRACT

As we have shown in the previous chapter, resolving the dynamic nuclear motion accompanying charge separation in bacterial reaction centers is crucial to understand how photosynthesis has optimized solar energy transduction. In this chapter we identify the pathway of primary electron transfer from the special pair excited state (P^*) to the accessory bacteriochlorophyll (B_A) using first-principles molecular dynamics and constrained density functional theory. We confirm that the oscillatory motion of a histidine at the interface between donor and acceptor initiates exciton dissociation and demonstrate how proton displacements are coupled to stable photoproduct formation.

Parts of this chapter were published in:

T. J. Eisenmayer, J. A. Lasave, A. Monti, H. J. M. de Groot, F. Buda, "Proton Displacements Coupled to Primary Electron Transfer in the Rhodobacter Sphaeroides Reaction Center", *Journal of Physical Chemistry B*, 2013, 38, pp 11162-11168.

DOI: 10.1021/jp401195t

4.1 Introduction

In bacterial photosynthesis, sunlight is absorbed by antenna complexes that transfer the excitation energy to reaction centers where the photoinduced charge separation takes place [1]. The transition state of the primary photochemical reaction in the *Rhodobacter Sphaeroides* reaction center (bRC) is not reached through random thermal motion but through specific vibrational coherences that effectively modulate the barrier for charge separation [1,2] (see previous Chapter). This mechanism is of interest for artificial devices aiming for high-yield photon-to-charge conversion.

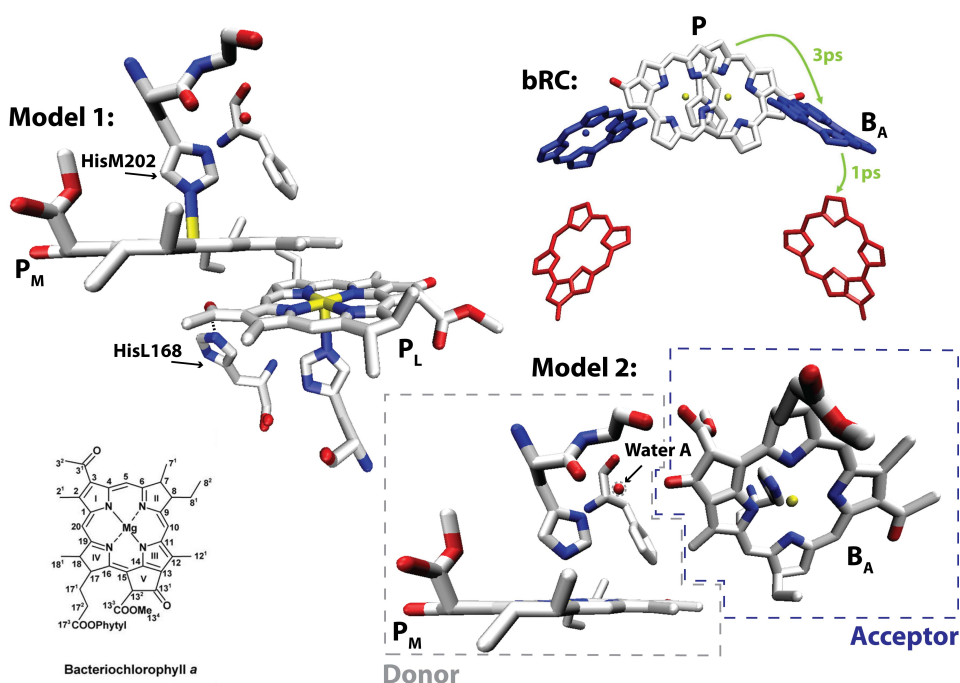


Figure 4.1: bRC (right top): Two-fold symmetric reaction center of *Rhodobacter sphaeroides* extracted from the latest 2.55 Å resolution X-ray structure (PDB entry 1M3X). The direction of electron transfer and corresponding time scales are denoted in green. Model 1 (left top): Including the special pair (P), axial histidines (HisL173 and HisM202), water A and B, and the diagonal symmetry-breaking residues PheM197 and HisL168. Model 2 (right bottom): Water A, the donor P_M , the primary acceptor B_A , the axial histidines (HisM202 and HisL153), and GlyM203. Inset (left bottom): Bacteriochlorophyll numbering.

The frequencies of these promoting vibrations are well-known from time-resolved spectroscopy [3-9]. In parallel, atomistic simulations are important because they can provide access to structural information that is inaccessible to spectroscopic methods. From the phenomenological study of Novoderezhkin and coworkers based on Redfield theory [2] we know that the formation of the first photoproduct is conveniently described by two vibrational coherences: a fast component of 100-150 cm^{-1} and a slower component of 30-35 cm^{-1} . The time scale of the primary photoinduced process in bRC is 3 ps, [10] and it occurs selectively along one of two pseudosymmetric cofactor branches (Figure 4.1) through a charge transfer (CT) intermediate [11,12] on the special pair (P). B_A is the accessory bacteriochlorophyll acting as primary acceptor. Subsequent electron transfer (ET) to form the secondary photoproduct along the A-branch, a reduced bacteriopheophytin (H_A^-), is very fast (1 ps). In this context, it is our aim to accurately characterize the reaction coordinate of the primary photoinduced charge separation from first principles. In previous work on the special pair, excited-state dynamics combined with a frequency analysis showed that a $\sim 100 \text{ cm}^{-1}$ vibrational mode is coupled to the electronic excitation, leading to a CT intermediate ($P_L^+ P_M^-$) [13]. Structurally, this $\sim 100 \text{ cm}^{-1}$ mode involves a collective motion of P with most of the amplitude on P_M and the rotation of HisM202 as the characteristic coordinate. This is predicted to be the first/fast vibrational component that coherently modulates the charge transfer dynamics [2]. HisM202 is hydrogen bonded to an interstitial water (water A), which is held in place by a hydrogen-bond network connecting P_M and B_A . The loss of water A through site-directed mutation is accompanied by a slowing of the rate of ET by approximately a factor of 8 [14]. The second/slower vibrational component coupled to full charge separation is thus thought to involve the motion of water A with a frequency of $\sim 30\text{-}35 \text{ cm}^{-1}$ [15]. The breaking of symmetry between cofactor chains is intimately related with the forward CT reactions. Although the special pair itself is already surrounded by the protein environment in a quasi-symmetric fashion (see Figure 4.1), on the L-side, HisL168 forms a hydrogen bond with the 3¹-acetyl of P_L , whereas on the M-side PheM197 does not. It is therefore plausible that even before excitation of P the ground-state electron density is asymmetrically distributed [16,17]. The vibrational mode corresponding to the hydrogen bond between P_L and HisL168 has been calculated to have a frequency of $\sim 50 \text{ cm}^{-1}$, and it is found to affect the stability of the cation ($P^{\bullet+}$) [13,18]. Here we employ atomistic simulations and single-point calculations to address (i) the role of the interstitial water A and (ii) the coupling of the ET process to configurational changes following the excitation and

(iii) upon oxidation of P .

4.2 Model and Methods

We extract the special pair (Model 1) and the donor-acceptor model (Model 2) from the latest X-ray crystallographic data of wild-type *Rhodobacter sphaeroides* at 2.55 Å resolution [19]. The special pair Model 1 includes the two Bacteriochlorophylls P_M and P_L , the five closest amino acids (GlyM203, PheM197, HisM202, HisL173, HisL168), and two interstitial waters (Figure 4.1). The donor-acceptor Model 2 includes P_M and its axially coordinated HisM202, taken as the donor of charge. B_A and its axially coordinated histidine HisL153 are taken as the charge acceptor (Figure 4.1). We also include PheM197 and GlyM203 to keep the whole protein pocket environment for the water A. For the entire system - Model 1 combined with Model 2 - we find that the HOMO and LUMO are localized on P_M and B_A , respectively, consistently with Model 2. Moreover, the HOMO-LUMO gap is not significantly altered (~ 0.04 eV) and this justifies the exclusion of P_L from Model 2 to keep the system size minimal. The mechanical constraints induced by the protein environment are ensured by fixing the tails of the histidines, the phenylene, and the glycine. Because of their length the phytol side chains are sterically hindered within the protein and are known not to affect the electronic structure of the bacteriochlorophylls [17]. Hence they are reduced to a methyl group that is fixed. The AIMD simulations have been performed using the Car-Parrinello method [20,21] as implemented in the CPMD code [22] with a time step of 0.1 fs. A Nosé thermostat is used in all simulations to keep the temperature around an average of 300 K. The time scales of the simulation runs for Model 1 were kept ~ 1 ps for ground, excited, and radical cation states. For Model 2 a ground-state simulation is performed for ~ 2 ps. It should be stressed that this simulation is not aimed at the explicit description of the nonadiabatic ET from P^* to B_A^- in real-time, which would require modeling the evolution of the excited electronic state (see Chapter 6) on a time scale of ~ 3 ps. The main goal of this AIMD simulation is to investigate the stability of the interstitial water and the thermal fluctuations in the hydrogen-bonding network established between the donor and acceptor. Both models are stable along the dynamics with a root-mean-square displacement (RMSD) that fluctuates around an average value of 0.8 Å for Model 2, slightly larger than the RMSD of Model 1 (0.6 Å). The BLYP functional [24,25] is used for the exchange-correlation energy, which is known to yield hydrogen bonds that are in good agreement with experiment. The Kohn-Sham orbitals are ex-

panded in a plane-wave basis set with an energy cutoff of 70 Ry. We employ dispersion-corrected atom-centered (DCACP) pseudopotentials [26,27]. To study the frequency domain, we perform Fourier transforms of the velocity autocorrelation function of the AIMD trajectory. We can in this way obtain specific characteristic frequencies of individual structural parameters (i.e., bond distances, bond angles). The recently developed computational method of Constrained Density Functional Theory (CDFT) is used to verify the predicted reaction coordinate of primary charge separation. This method was specifically developed by Wu and van Voorhis [21] to address long-range CT states. It has been shown that CDFT can accurately describe the excitation energy and its dependence on the donor-acceptor distance [28]. The CDFT calculations are performed with the same functional, basis set, and pseudopotentials used for the AIMD simulations. In the CDFT method applied to bRC, the charge-localized states (or diabatic states) A and B are obtained from two DFT calculations. The first represents the initial state where no ET between donor and acceptor has occurred yet (state A), while the second (state B) describes the charge-separated state obtained by constraining a positive charge on the donor and a negative charge on the acceptor. The resulting ground-state density $\rho(r)$ on each diabatic state will satisfy the constraint

$$\int_V W(r)\rho(r)dr = N_c \quad (4.1)$$

where $W(r)$ is the operator that defines the electronic population and the integral runs over the entire volume of the system. N_c is the value of the constraint defined as the charge difference between the net charge on the donor and acceptor group: $N_c = N_{don} - N_{acc}$. Therefore, we choose $N_c = 0$ for state A and $N_c = 2$ for state B. For the population operator we use the Hirshfeld partitioning scheme [29] as implemented in the CPMD code [30].

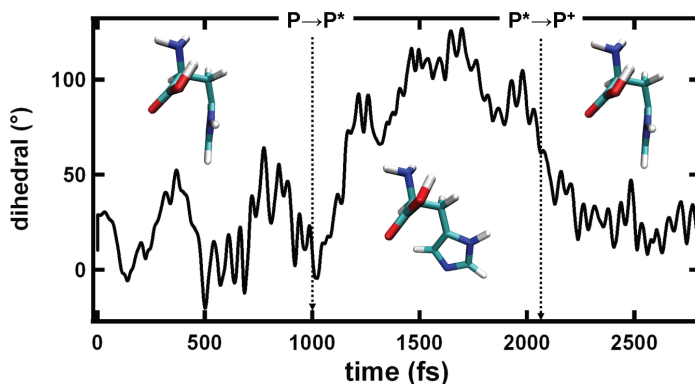
4.3 Results

AIMD Simulations

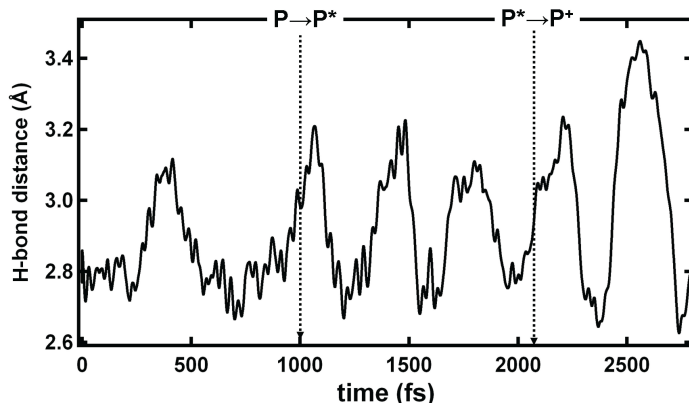
Previous AIMD simulations on the special pair (Model 1) ground and excited state found two important degrees of freedom coupled to electronic structure rearrangements of P : (1) the rotation of HisM202 with respect to the Mg- N_τ coordination axis and (2) the hydrogen bond between P_L and HisL168 [13]. Here we extend these simulations to analyze the oxidized radical cation state. The first degree of freedom and characteristic coordinate of the

vibrational mode coupled to the formation of the CT intermediate involves the rotation of the axial histidine M202. From Figure 4.2(a), which shows the compiled trajectories for ground state, excited state, and radical cation, it can be seen that HisM202 rotates upon excitation to an average dihedral angle of 80° with respect to the Mg- N_τ coordination axis. Upon oxidation this conformational rearrangement is reversed and the dihedral angle rotates back to the ground-state values.

Figure 4.2: AIMD simulations in P , P^* and $P^{\bullet+}$.



(a) AIMD simulations of Model 1 showing the time evolution of the HisM202 dihedral angle with respect to the Mg- N_τ coordination axis along the ground (0 to 1.0 ps), excited (1.0 to 2.1 ps), and oxidized state (2.1 to 2.8 ps) trajectories.



(b) N...O hydrogen-bond distance between HisL168 and the 3^1 -acetyl of P_L for ground state (0 to 1.0 ps), excited state (1.0 to 2.1 ps), and radical cation (2.1 to 2.8 ps) AIMD trajectories. Upon excitation no changes in the amplitude of the fluctuations are observed, whereas in the radical cation state the hydrogen bond is weakened, representing a proton displacement.

4.3. RESULTS

Inversely, the second important degree of freedom involving the hydrogen bond between the 3¹-acetyl of P_L and HisL168 (see Figure 4.1) shows no significant changes going from ground to excited state. However, upon oxidation the oscillations become larger and the hydrogen bond is on average weakened (Figure 4.2(b)).

For the donor-acceptor model (Model 2) a room-temperature AIMD simulation is performed extending over 2 ps. DFT single-point calculations performed at several snapshots along the trajectory show consistently that the HOMO is localized on P_M and the LUMO is localized on B_A . The LUMO electron density extends over the interstitial water A, whereas the HOMO shows no electron density in this region, although it does extend over the axial histidine M202. To understand the structural cause of HOMO-LUMO localization we investigated the planarity of both chromophores taking into account the C₃-C₇-C₁₂-C₁₇ dihedral angle (see inset, Figure 4.1). P_M is found to be the more distorted chromophore, whereas B_A is almost perfectly planar. Another factor influencing the HOMO-LUMO localization is the orientation of the axial histidines relative to the Mg-N_τ axis. For P_M the dihedral angle of the axially coordinated histidine, averaged over the dynamics, is 21°, whereas for B_A this angle is -108°. The position of water A in its hydrogen-bond network is stable throughout the dynamics. The average position of water A is halfway between the HisM202-nitrogen and the 13¹-keto-carbonyl of B_A .

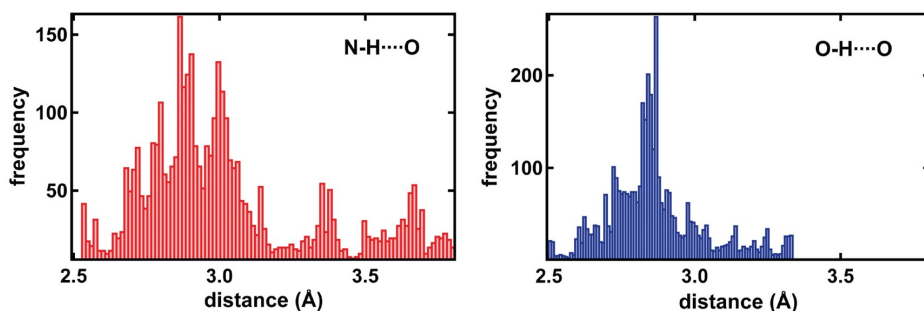


Figure 4.3: Distribution of distances centered around the interstitial water A oxygen atom sampled during the AIMD simulations of Model 2 in the ground state. Left graph (red) distribution of N-H...O distances representing the hydrogen bond with HisM202. Right graph (blue) distribution of O-H...O distances representing the hydrogen bond with the keto carbonyl of B_A .

Figure 4.3 shows the distribution of N-H \cdots O and O-H \cdots O distances. The most frequently occurring separation is ~ 2.8 Å for both degrees of freedom. The N-H \cdots O distances additionally have a tail at larger separations with peaks at 3.4 and 3.7 Å. Dynamically, both protons of water A form and break hydrogen bonds with the keto carbonyl of B_A in a "switching" motion (Figure 4.4(a,b)). A Fourier analysis of this motion, in terms of hydrogen-bond angles and distances, gives a frequency of 30–35 cm^{-1} for the breaking and forming of the keto carbonyl hydrogen bonds (Figure 4.4(c)). The weakest hydrogen bond of water A is with GlyM203, which is rarely formed during the 2 ps ground-state trajectory.

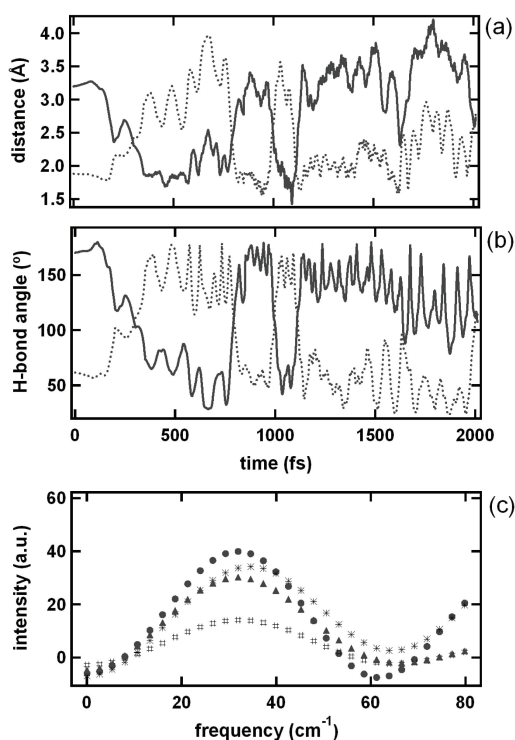


Figure 4.4: Hydrogen bond H \cdots O distance (a) and O-H \cdots O angle (b) along the dynamical trajectory. The full and dotted line show the two protons of water A that break and form hydrogen bonds in a "switching" motion with the keto ^{13}C carbonyl group of B_A . The bottom graph (c) shows the Fourier transform of this molecular motion between water A and the keto carbonyl group of B_A with a first peak at 30–35 cm^{-1} in agreement with the experimental result of Yakovlev et al. [15].

Constrained DFT

To explore the reaction coordinate of excited-state relaxation and ET we performed CDFT calculations constraining a positive charge on the donor (P_M) and a negative charge on the acceptor (B_A). Following the HOMO-LUMO analysis, we include the axial histidine HisM202 in the donor and the axial histidine HisL153 in the acceptor. Energies are calculated as a function of the dihedral angle corresponding to the HisM202 rotation (see Figure 4.2(a)). For each value of the dihedral angle we optimize the other degrees of freedom including the position of water A. The energy difference between the ground state and the vertical charge separated state - calculated with CDFT at the ground state geometry - decreases along the suggested reaction coordinate, as shown in Figure 4.5.

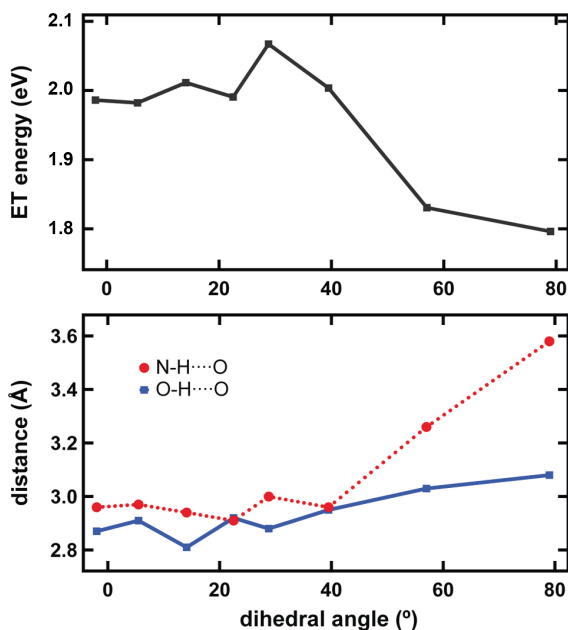


Figure 4.5: Top: Vertical electron transfer (ET) energy dependence on the dihedral angle of HisM202 with respect to the Mg- N_τ coordination axis. Bottom: N-H...O (circles) and O-H...O (squares) hydrogen-bond distances as a function of the same dihedral angle.

The results in Figure 4.5 show that the vertical ET energy decreases along the collective reaction coordinate approximated by the rotation of HisM202. We also observe that along this coordinate proton displacement

accompany the charge separation: The rotation of HisM202 displaces water A in its hydrogen-bond pocket toward the carbonyl of B_A and GlyM203 (Figure 4.5). After ET the N-H...O distance increases to 3.6 Å, representing a considerable weakening of the hydrogen bond between the water and HisM202 (Figure 4.5). Interestingly, it is apparent that already in the ground state this conformation of the hydrogen-bond network is occasionally sampled (see Figure 4.3). Thus, while our results show no direct evidence for full proton coupled electron transfer (PCET) they indicate proton displacements coupled to the reaction coordinate.

Finally, within the entire model it is possible to verify that the unoccupied Kohn-Sham states on the special pair are higher in energy than the unoccupied Kohn-Sham state on B_A . Indeed, the lowest LUMO on P^* is 0.14 eV higher in energy than the LUMO on B_A (Figure 4.6). This represents a small overestimation with respect to experiment, where the negative energy gradient (ΔG) is estimated to be ~ -0.06 eV [34].

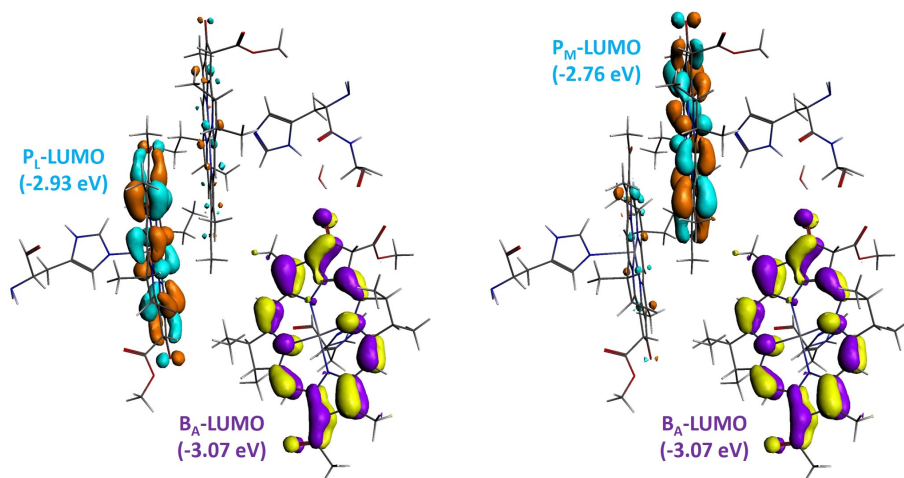


Figure 4.6: Left: Spatial distribution and energies of the LUMO on P_L and on B_A . Right: Spatial distribution and energies of the LUMO on P_M and on B_A . As detailed in Chapter 3, the frontier orbitals on the special pair exhibit dynamic localization and the initial excitonic state can thus involve a population of either $P_L \cdot LUMO$ or $P_M \cdot LUMO$. The orbitals calculated at the B3LYP/TZP level of theory and their associated dynamics (Chapter 3) reveal that there is a reaction coordinate for photoinduced charge separation to the $B_A \cdot LUMO$.

4.4 Discussion and Conclusions

In this chapter, we elucidate the conformational rearrangements that couple to the full ET from the special pair excited state of bRC to the primary acceptor B_A . The charge separation is highly optimized and known to occur at an optimal rate [33]. Recently, this rate was found to be governed by a single (Goldilocks) parameter Λ that at the point of optimum transfer is equal to $1/\sqrt{2}$ [35].

$$\Lambda_{opt} = \frac{\lambda T}{\gamma_c \Delta G} = \frac{1}{\sqrt{2}} \quad (4.2)$$

If we consider the ambient conditions at which bRC operates ($300K \sim 26meV$), the experimental value for the reorganization energy ($\lambda \sim 28meV$ [36]) and for the energy gradient ($\Delta G \sim 65meV$ [34]), the only unknown parameter remains the bath correlation time γ_c . As this parameter describes the correlation between the electronic states (P^*B and PB^-) and the (protein) environment, we provide the value of the first low frequency mode that couples to ET ($100cm^{-1} \sim 12.5meV$). Then, indeed the Goldilocks parameter is $\sim 1/\sqrt{2}$.

In Chapter 3, the coordinate of this low frequency mode was found to involve the rotation of HisM202, which from Figure 4.2a is seen to be reversible upon oxidation. This rotation displaces the protons of water A toward GlyM203 and the 13^1 -carbonyl of B_A in a collinear fashion with respect to the direction of ET (Figure 4.7). The proton displacement is found to have a frequency of $30\text{-}35\text{ cm}^{-1}$ in good agreement with experiment and thus gives a structural interpretation to the second coordinate of charge separation suggested in the phenomenological study by Novoderezhkin and coworkers [2]. In contrast with Ivashin and Larsson, who propose a double proton-transfer mechanism within the hydrogen-bond network surrounding water A [37], we observe proton displacements following ET (Figures 4.5 and 4.7). In the ground state, these conformations are already occasionally sampled (Figure 4.3), although the average distance of water A from HisM202 is 2.9 \AA . In the charge-separated state we find a new equilibrium value of 3.6 \AA at the same approximate values where the ground-state histogram exhibits a long tail (Figure 4.3). The second proton displacement found to couple to oxidation of P involves the weakening of the hydrogen bond between HisL168 and the 3^1 -acetyl of P_L . The weakening of this interaction destabilizes the HOMO of P_L [13], the site on which most of the positive charge is localized in $P^{\bullet+}$ [38], and therefore

reduces the driving force for charge recombination. Experimental evidence for such a mechanism is possibly given by Deshmukh and coworkers [39], who find a light-induced hypsochromic shift in *Rhodobacter capsulatus* and suggest this to be caused by the 3¹-acetyl group.

In conclusion, the reaction coordinate of initial charge separation in the *Rhodobacter sphaeroides* reaction center is a multidimensional landscape. First, upon excitation a reversible conformational rearrangement stabilizes the charge transfer from P_L to P_M , mostly involving the rotation of HisM202 with a characteristic frequency of $\sim 100\text{ cm}^{-1}$. Second, through this rotation a proton is displaced in the hydrogen network surrounding water A with a frequency of $30\text{--}35\text{ cm}^{-1}$. Finally, on a longer time scale, another proton is displaced from the 3¹-acetyl of P_L toward HisL168, which destabilizes the cation $P^{\bullet+}$ by mixing in the P^{\bullet} neutral radical state. This effectively reduces the driving force for charge recombination. Together these rearrangements present a structural framework for understanding the highly efficient and coherent CT process from the special pair excited state to the primary charge-separated state.

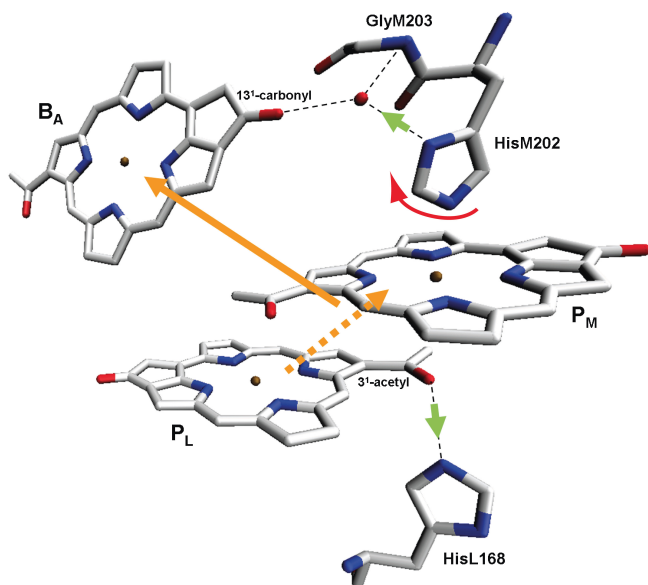


Figure 4.7: Schematic representation of the nuclear motion (green and red arrows) accompanying the charge and electron transfer processes (orange arrows).

4.5 References

- [1] Deisenhofer, J.; Epp, O.; Miki, K.; Huber, R.; Michel, H. Structure of the Protein Subunits in the Photosynthetic Reaction Centre of *Rhodospseudomonas Viridis* at 3Å Resolution. *Nature* **1985**, 318, 618-624.
- [2] Novoderezhkin, V.; Yakovlev, A.; van Grondelle, R.; Shuvalov, V. Coherent Nuclear and Electronic Dynamics in Primary Charge Separation in Photosynthetic Reaction Centers: A Redfield Theory Approach. *J. Phys. Chem. B* **2004**, 108, 7445-7457.
- [3] Vos, M. H.; Jones, M. R.; Hunter, C. N.; Breton, J.; Martin, J. L. Coherent Nuclear Dynamics at Room Temperature in Bacterial Reaction Centers. *Proc. Natl. Acad. Sci. U.S.A.* **1994**, 91, 12701-12705.
- [4] Vos, M. H.; Jones, M. R.; Martin, J. L. Vibrational Coherence in Bacterial Reaction Centers: Spectroscopic Characterisation of Motions Active during Primary Electron Transfer. *Chem. Phys.* **1998**, 233, 179-190.
- [5] Rischel, C.; Spiedel, D.; Ridge, J. P.; Jones, M. R.; Breton, J.; Lambry, J. C.; Martin, J. L. Low Frequency Vibrational Modes in Proteins: Changes Induced by Point-Mutations in the Protein- Cofactor Matrix of Bacterial Reaction Centers. *Proc. Natl. Acad. Sci. USA.* **1998**, 95, 12306-12311.
- [6] Reddy, N. R.; Kolaczowski, S. V.; Small, G. J. A Photoinduced Persistent Structural Transformation of the Special Pair of a Bacterial Reaction Center. *Science* **1993**, 260, 68-71.
- [7] Cherepy, N. J.; Shreve, A. P.; Moore, L. J.; Franzen, S.; Boxer, S. G.; Mathies, R. a. Near-Infrared Resonance Raman Spectroscopy of the Special Pair and the Accessory Bacteriochlorophylls in Photosynthetic Reaction Centers. *J. Phys. Chem.* **1994**, 98, 6023-6029.
- [8] Yakovlev, A. G.; Shkuropatov, A. Y.; Shuvalov, V. A. Nuclear Wave Packet Motion between P^* and $P^+B_A^-$ Potential Surfaces with a Subsequent Electron Transfer to HA in Bacterial Reaction Centers at 90 K. Electron Transfer Pathway. *Biochemistry* **2002**, 41, 14019-14027.
- [9] Shuvalov, V.; Yakovlev, A. Coupling of Nuclear Wavepacket Motion and Charge Separation in Bacterial Reaction Centers. *FEBS Lett.* **2003**, 540, 26-34.
- [10] Moore, L. J.; Zhou, H.; Boxer, S. G. Excited-State Electronic Asymmetry of the Special Pair in Photosynthetic Reaction Center Mutants: Absorption and Stark Spectroscopy. *Biochemistry* **1999**, 38, 11949-11960.
- [11] Cohen Stuart, T.; van Grondelle, R. Multipulse Spectroscopy on the Wild-Type and YM210W Bacterial Reaction Centre Uncovers a New Intermediate State in the Special Pair Excited State. *Chem. Phys. Lett.* **2009**, 474, 352-356.
- [12] Holzapfel, W.; Finkle, U.; Kaiser, W.; Oesterhelt, D.; Scheer, H.; Stolz, H. U.; Zinth, W. Initial Electron-Transfer in the Reaction Center from Rhodobacter

- Sphaeroides. *Proc. Natl. Acad. Sci. U.S.A.* **1990**, *87*, 5168-5172.
- [13] Eisenmayer, T. J.; de Groot, H. J. M.; van de Wetering, E.; Neugebauer, J.; Buda, F. Mechanism and Reaction Coordinate of Directional Charge Separation in Bacterial Reaction Centers. *J. Phys. Chem. Lett.* **2012**, *3*, 694-697.
- [14] Potter, J. A.; Fyfe, P. K.; Frolov, D.; Wakeham, M. C.; Grondelle, R. V.; Robert, B.; Jones, M. R. Strong Effects of an Individual Water Molecule on the Rate of Light-driven Charge Separation in the Rhodobacter sphaeroides Reaction Center. *Biochemistry* **2005**, *280*, 27155-27164.
- [15] Yakovlev, A. G.; Shuvalov, V. A. Electron Transfer in Deuterated Reaction Centers of Rhodobacter Sphaeroides at 90 K According to Femtosecond Spectroscopy Data. *Biochemistry* **2003**, *68*, 603-610.
- [16] Daviso, E.; Prakash, S.; Alia, A.; Gast, P.; Neugebauer, J.; Jeschke, G.; Matysik, J. The Electronic Structure of the Primary Electron Donor of Reaction Centers of Purple Bacteria at Atomic Resolution as Observed by PhotoCIDNP ^{13}C NMR. *Proc. Natl. Acad. Sci. U.S.A.* **2009**, *106*, 22281-22286.
- [17] Wawrzyniak, P. K.; Beerepoot, M. T. P.; de Groot, H. J. M.; Buda, F. Acetyl Group Orientation Modulates the Electronic Ground-State Asymmetry of the Special Pair in Purple Bacterial Reaction Centers. *Phys. Chem. Chem. Phys.* **2011**, *13*, 10270-10279.
- [18] Rautter, J.; Lendzian, F.; Schulz, C.; Fetsch, A.; Kuhn, M.; Lin, X.; Lubitz, W. ENDOR Studies of the Primary Donor Cation Radical in Mutant Reaction Centers of Rhodobacter Sphaeroides with Altered Hydrogen-Bond Interactions. *Biochemistry* **1995**, *34*, 8130-8143.
- [19] Camara-Artigas; Brune, D.; Allen, J. P. Interactions between Lipids and Bacterial Reaction Centers Determined by Protein Crystallography. *Proc. Natl. Acad. Sci. U.S.A.* **2002**, *99*, 11055-11060.
- [20] Car, R.; Parrinello, M. Unified Approach for Molecular Dynamics and Density-Functional Theory. *Phys. Rev. Lett.* **1985**, *55*, 2471.
- [21] Marx, D.; Hutter, J. *Ab Initio Molecular Dynamics: Basic Theory and Advanced Methods*; Cambridge University Press: Cambridge, U.K., **2009**.
- [22] Wu, Q.; Van Voorhis, T. Constrained Density Functional Theory and its Application in Long-Range Electron Transfer. *J. Chem. Theory Comput.* **2006**, *2*, 765-774.
- [23] CPMD v3.11.1, Copyright IBM Corp, 1990-2008; Copyright MPI für Festkörperforschung Stuttgart, 1997-2001. <http://www.cpmd.org/>.
- [24] Becke, A. D. Density-Functional Exchange-Energy Approximation with Correct Asymptotic Behavior. *Phys. Rev. A* **1988**, *38*, 3096.
- [25] Lee, C.; Yang, W.; Parr, R. G. Development of the Colle-Salvetti Correlation-energy Formula into a Functional of the Electron Density. *Phys. Rev. B* **1988**, *37*, 785.

4.5. REFERENCES

- [26] von Lilienfeld, O. A.; Tavernelli, I.; Rothlisberger, U.; Sebastiani, D. Optimization of Effective Atom Centered Potentials for London Dispersion Forces in Density Functional Theory. *Phys. Rev. Lett.* **2004**, 93, 153004.
- [27] von Lilienfeld, O. A.; Tavernelli, I.; Rothlisberger, U.; Sebastiani, D. Performance of Optimized Atom-centered Potentials for Weakly Bonded Systems Using Density Functional Theory. *Phys. Rev. B* **2005**, 71, 195119.
- [28] Wu, Q.; Van Voorhis, T. Direct Optimization Method to Study Constrained Systems Within Density-functional Theory. *Phys. Rev. A* **2005**, 72, 024502.
- [29] Hirshfeld, F. L. Bonded-atom Fragments for Describing Molecular Charge Densities. *Theor. Chem. Acc.* **1977**, 44, 129.
- [30] Oberhofer, H.; Blumberger, J. Electronic Coupling Matrix Elements From Charge Constrained Density Functional Theory Calculations Using a Plane Wave Basis Set. *J. Chem. Phys.* **2010**, 133, 244105.
- [31] Marcus, A.; Sutin, N. Electron Transfers in Chemistry and Biology. *Biochim. Biophys. Acta* **1985**, 811, 265.
- [32] Moser, C. C.; Keske, J. M.; Warncke, K.; Farid, R. S.; Dutton, L.P. Nature of Biological Electron Transfer. *Nature* **1992**, 355, 796-802.
- [33] Blumberger, J. Free Energies for Biological Electron Transfer from QM/MM Calculation: Method, Application and Critical Assessment. *Phys. Chem. Chem. Phys.* **2008**, 10, 5651-5667.
- [34] Smith, D. M. A.; Rosso, K. M.; Dupuis, M.; Valiev, M.; Straatsma, T. P. Electronic Coupling between Heme Electron-Transfer Centers and Its Decay with Distance Depends Strongly on Relative Orientation. *J. Phys. Chem. B* **2006**, 110, 15582-15588.
- [35] L. Mourokh and S. Lloyd, Optimal rates for electron transfer in Marcus theory, *Phys. Rev. E.*, **2013**, 88, 42819.
- [36] D. C. Arnett, C. Moser, P. L. Dutton and N. F. Scherer, The First Events in Photosynthesis: Electronic Coupling and Energy Transfer Dynamics in the Photosynthetic Reaction Center from Rhodobacter sphaeroides, *J. Phys. Chem. B*, **1999**, 103, 2014-2032.
- [37] Ivashin, N.; Larsson, S. Trapped Water Molecule in the Charge Separation of a Bacterial Reaction Center. *J. Phys. Chem. B* **2008**, 112, 12124.
- [38] Lendzian, F.; Huber, M.; Isaacson, R. A.; Endeward, B.; Plato, M.; Bořl̃nigk, B.; Mořl̃bius, K.; Lubitz, W.; Feher, G. The Electronic Structure of the Primary Donor Cation Radical in Rhodobacter Sphaeroides R-26: ENDOR and TRIPLE Resonance Studies in Single Crystals of Reaction Centers. *Biochim. Biophys. Acta* **1993**, 1183, 139-160.
- [39] Deshmukh, S. S.; Akhavein, H.; Williams, J. C.; Allen, J. P.; Kařl̃mařn, L. Light-Induced Conformational Changes in Photosynthetic Reaction Centers: Impact of Detergents and Lipids on the Electronic Structure of the Primary Electron Donor. *Biochemistry* **2011**, 50, 5249-5262.

*"I must Create a System, or be enslav'd by another Man's.
I will not Reason and Compare;
my business is to Create."*

— William Blake —

Jerusalem (1804)

Chapter 5

Photoinduced Coherent Charge Transfer

5.0.1 ABSTRACT

Theoretical and spectroscopic evidence of coherent oscillatory behaviour associated to photoinduced charge transfer has been reported both in complex biological environments as well as in biomimetic models for artificial photosynthesis. Here we consider a biomimetic model to investigate this process in real-time simulations based on Ehrenfest dynamics. The Ehrenfest formalism allows for a detailed analysis of how photon-to-charge conversion is promoted by a coupling of the electronic excitation with specific vibrational modes. The simulations show that when the difference in energy between the exciton and charge transfer orbitals matches the frequency of interfacial bond-stretching the energies of the orbitals start to oscillate in resonance. Moreover, charge transfer is only observed when these interfacial N-H bonds are free to move.

Parts of this chapter were published in:

T. J. Eisenmayer and F. Buda, "Real-time Simulations of Photoinduced Coherent Charge Transfer and Proton-Coupled Electron Transfer", *ChemPhysChem*, 2014.

DOI: 10.1002/cphc.201402444

5.1 Introduction

In natural photosynthesis, photoinduced charge separation is the first fundamental step leading to the conversion of solar energy into chemical energy (see Chapters 3 and 4 of this thesis and [1,2]). There is converging experimental and theoretical evidence of oscillatory features associated with the reaction coordinates for energy and electron transfer in natural and artificial photosynthetic complexes (see Chapters 3 and 4 of this thesis and [3-9]). Understanding the nature and the role of this coherent dynamics is important both from a fundamental and technological point of view, as it may provide guiding principles for the design of efficient molecular devices for solar to fuel conversion. Photoinduced electron transfer processes are usually analysed in the context of transition rates. However, in reality many competing processes occur at the same time including dynamic and possibly coherent nuclear motion. Here we use instead Ehrenfest dynamics simulations to overcome this issue and investigate in real-time the coupling between the electronic motion and specific vibrational modes of the complex. We consider a donor-acceptor hydrogen bonded complex formed by melamine and isocyanuric acid that mimicks DNA base-pairing [10].

5.2 Model and Methods

For the time dependent Kohn-Sham (TDDFT) simulations of photoinduced electron transfer we consider a supramolecular complex consisting of melamine (1,3,5-triazine-2,4,6-triamine) and isocyanuric acid (1,3,5-triazine-2,4,6-trione) held together by a hydrogen bonding network (Figure 5.1) [11].

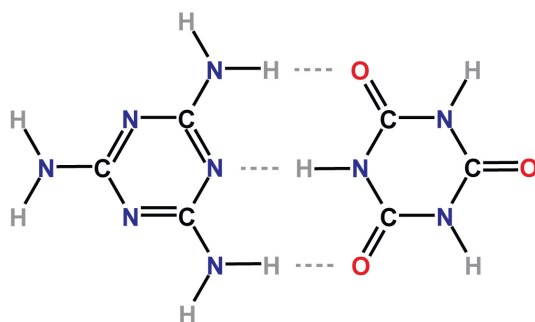


Figure 5.1: Melamine (donor; left) and isocyanuric acid (acceptor; right).

The biomimicry of the model lies in its resemblance with DNA base-pairing as it self-assembles into a tile-like structure with two-dimensional hydrogen bonds [11]. The geometry optimization of the complex is performed with the ADF program [12] at the BLYP/TZP level of theory. We do not impose the symmetry (C_{2v} in this case); therefore even a small residual asymmetry at the end of the geometry optimization will manifest itself in the molecular orbitals. This can be seen in Figure 5.2 for the LUMO+2 that has no amplitude on the lower right amine, while it does on the top right amine.

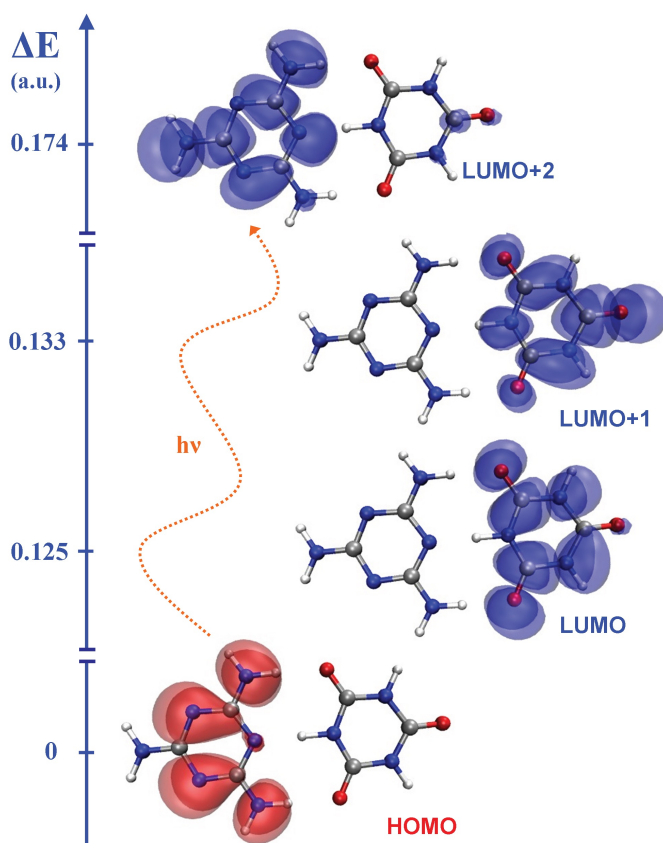


Figure 5.2: Localization of the frontier molecular orbitals at $t = t(0)$. The photoexcitation $[HOMO] \rightarrow [LUMO+2]$ and its energy are shown together with the gradients for photoinduced charge transfer $[LUMO+2] \rightarrow [LUMO+1/LUMO]$.

The optimized geometry is then used to perform a spin-polarized single-point LDA [13] density optimization on a real space grid with 52 Ry cutoff

using the OCTOPUS suite [14-17]. The core electrons are described by Troullier-Martins pseudopotentials in SIESTA format [18]. From the obtained set of occupied and unoccupied states we prepare the system in a single-particle excited state on the melamine, by depopulating the HOMO and populating the LUMO+2 (Figure 5.2). We also calculated the energies the relevant orbitals using different exchange-correlation functionals, including the Local-Density Approximation (LDA), a Generalized Gradient Approximation (BLYP) and several hybrid functionals with varying amount of Hartree-Fock exchange. We observe that the orbital energies involved in the photoinduced electron transfer process do not change significantly with respect to the Local-Density Approximation that is used to propagate the excitonic (HOMO \rightarrow LUMO+2) state in time. In Table 5.1 we also report the oscillator strengths of the relevant excitations for the complex obtained using linear-response TDDFT calculations.

	BLYP	B3LYP	B1LYP	MPW1PW	CAM-B3LYP
Excitonic state (eV)	6.49	6.49	6.66	6.68	6.93
<i>Oscillator strength</i>	<i>0.295</i>	<i>0.191</i>	<i>0.274</i>	<i>0.269</i>	<i>0.597</i>
Charge Transfer state (eV)	3.57	4.79	5.11	5.14	6.45
<i>Oscillator strength</i>	<i>0.001</i>	<i>0.002</i>	<i>0.002</i>	<i>0.002</i>	<i>0.007</i>

Table 5.1: Linear-response TDDFT energies (eV) with different functionals.

We employ the BLYP and several hybrid functionals with varying amount of Hartree-Fock exchange. We also include the results obtained with the long-range corrected functional CAM-B3LYP that generally provides more accurate charge transfer excitation energies. Moreover, we have performed higher level ab initio calculations using the EOM-CCSD method with a cc-pVDZ basis set for the donor molecule. All these additional test calculations have been performed using the Gaussian 09 package [19]. We verify that across the range of functionals the excitonic state on the melamine has the highest oscillator strength. This justifies the [HOMO] \rightarrow [LUMO+2] excitation as the most appropriate starting condition for the excited state trajectories. For the excited state dynamics starting from the excitonic state, we solve the time dependent Kohn-Sham equations using the OCTOPUS quantum-chemical suite [14-17] with a time step of 2 attoseconds:

$$i \frac{\partial}{\partial t} \varphi_i(\mathbf{r}, t) = [-1/2 \nabla^2 + v_{eff}(\mathbf{r}, t)] \varphi_i(\mathbf{r}, t)$$

$$\sum_i^N |\varphi_i(\mathbf{r}, t)|^2 = \rho(\mathbf{r}, t). \quad (5.1)$$

This is achieved by constructing the time-dependent orbitals $\varphi(\mathbf{r}, t)$ through an expansion of the adiabatic Kohn-Sham orbitals $\phi_i(\mathbf{r}; \mathbf{R}(t))$ [20]:

$$\varphi(\mathbf{r}, t) = \sum_i c_i(t) \phi_i(\mathbf{r}; \mathbf{R}(t)). \quad (5.2)$$

To approximate the evolution operator we use the Approximated Enforced Time-Reversal Symmetry algorithm [17] and the exponential of the Hamiltonian is calculated by Taylor expansion. The nuclei are propagated classically within the Ehrenfest formalism on a mean-field potential energy surface [21]:

$$M_I \frac{d^2 \mathbf{R}_I}{dt^2} = - \frac{\partial E_{KS}[\rho(\mathbf{r}, t)]}{\partial \mathbf{R}_I}. \quad (5.3)$$

Nonadiabatic transitions between orbitals are invoked by evaluating the nonadiabatic coupling:

$$\mathbf{d}_{ij} = \langle \phi_i(\mathbf{r}; \mathbf{R}(t)) | \nabla_{\mathbf{R}} | \phi_j(\mathbf{r}; \mathbf{R}(t)) \rangle \cdot d\mathbf{R}/dt, \quad (5.4)$$

that modifies the coefficients $c_i(t)$ through [20]:

$$i \frac{\partial c_i(t)}{\partial t} = \sum_j c_j(t) (\epsilon_j \delta_{ij} - \mathbf{d}_{ij}), \quad (5.5)$$

To quantify the photoinduced electron transfer along the dynamics we monitor the photoinduced spin density (PSD):

$$PSD(r) = \rho^\beta(r) - \rho^\alpha(r) = \sum_i^{N/2} |\phi_i^\beta(r)|^2 - \sum_i^{N/2} |\phi_i^\alpha(r)|^2 \quad (5.5)$$

where ρ represents the density, α and β the respective spin species, N the number of electrons and ϕ_i the Kohn-Sham molecular orbitals. Although the total spin of the system is equal to 0, the spatial spin distribution upon photoexcitation will show regions with an excess of α or β spin. By partitioning the simulation box in two halves, one containing the electron donor (melamine) and the other containing the electron acceptor (isocyanuric acid) we quantify the amount of PSD transferred through the hydrogen bond network. Furthermore, the negative/depleted regions of the PSD give the spatial localization of the photoinduced hole, whereas regions with an increase in PSD correspond to the photoinduced electron transfer.

5.3 Results and Discussion

To follow the photoinduced electron transfer through a hydrogen bond network we prepare the melamine cyanurate complex in a singlet excited state on the melamine. This represents a typical excitonic state where the electron and hole are both localized on the same moiety with no net charge transfer.

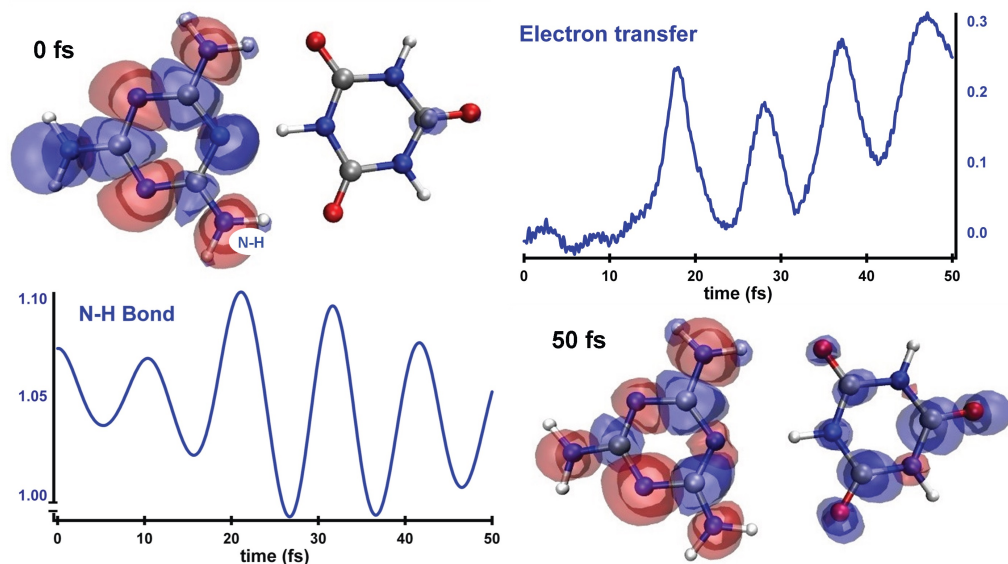


Figure 5.3: Coherent photoinduced electron transfer (upper right panel) in a DNA-base-pair-mimic held together by hydrogen bonds (See Movie 5.1). The calculations were performed in real-time within the Ehrenfest formalism starting from the localized photoinduced spin density in the upper left panel. The photoinduced spin density after 50 fs (lower right panel) shows electron transfer (blue) to the isocyanuric acid and an accumulation of the hole (red) on the melamine. The fluctuations in the hydrogen bond network, illustrated by the N-H bond (Å) in the lower left panel, indicate a coherent coupling between proton displacements and electron transfer.

In terms of the photoinduced spin, we can compare the initial state of the quantum-classical dynamics (Figure 5.3, top left) with the involved orbitals (Figure 5.2) and verify that the depleted (red) density corresponds to the HOMO and the increase (blue) corresponds to the LUMO+2. Starting from the localized exciton state on the melamine the quantum-classical dynam-

ics simulation shows charge transfer through the hydrogen bond network with superimposed temporal oscillations with a period of approximately 10 fs (Figure 5.3, upper right panel). In wavenumbers this equals $\sim 3300 \text{ cm}^{-1}$, which lies in the amine N-H stretching mode range suggesting a coherent coupling of the (nonadiabatic) electron transfer with nuclear motion involving the hydrogen bond network. This is further illustrated by simply comparing the N-H bond dynamics (Figure 5.3, bottom left panel) with the oscillatory electron transfer along the trajectory, both exhibiting the same number of oscillations within the simulation time. The total charge transferred in 50 fs amounts to ~ 0.3 electron equivalent. The dynamical snapshots in Appendix I show the photoinduced spin density along the dynamics where this oscillatory behaviour in the charge transfer is evident.

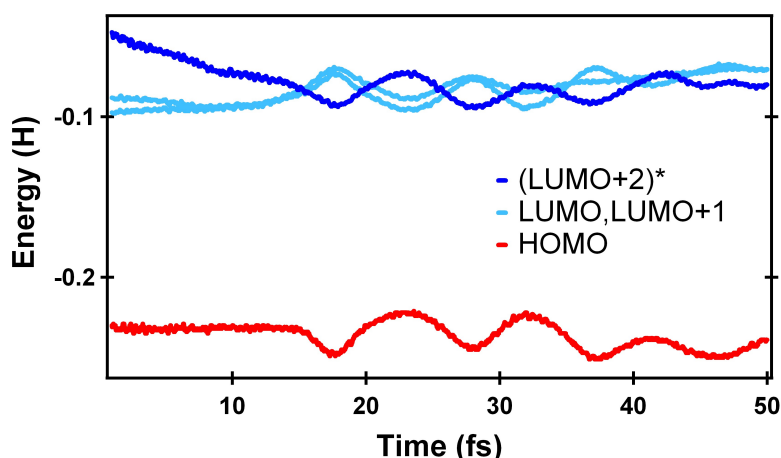


Figure 5.4: Eigenvalues of the molecular orbitals, the dark blue line represents the initially occupied excitonic LUMO+2, while the light blue lines represent the populated charge transfer orbitals LUMO and LUMO+1.

Interestingly, in Figure 5.4 it can be seen that the energies of the exciton (LUMO+2, dark blue line in Figure 5.4) and charge transfer states (LUMO+1, LUMO, light blue lines in Figure 5.4) oscillate in quasi-resonance once their difference matches the $\sim 3300 \text{ cm}^{-1}$ energy of the N-H stretching vibration. This happens after approximately 10 fs, and is also the point where the charge transfer from the melamine donor to the isocyanuric acid acceptor is initiated (Figure 5.3, upper right panel). Therefore the coupling with the interfacial N-H stretching mode seems

crucial for there to be any charge transfer. We verify this by fixing the coordinates of the three interfacial N-H bonds and perform an identical dynamical evolution starting in the excitonic state. In this case the energies do not oscillate and do not cross as can be seen in Figure 5.5. Also, as can be seen from the dynamical snapshots in Appendix II no charge is transferred from the melamine donor to the isocyanuric acid acceptor.

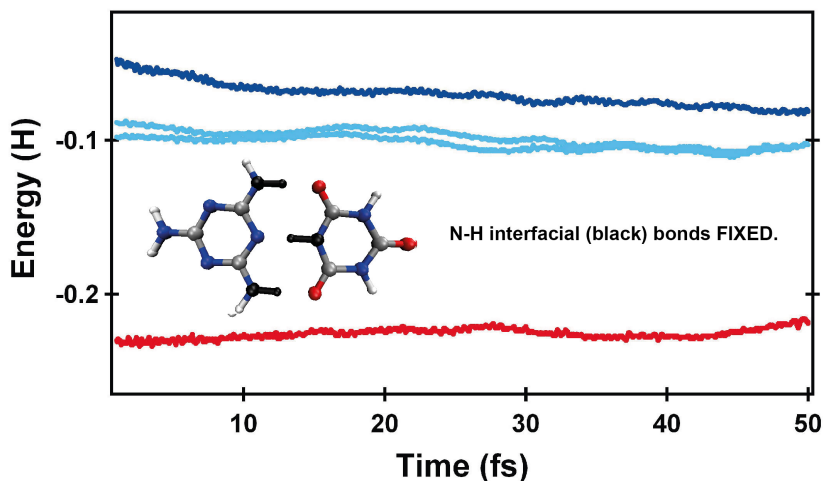


Figure 5.5: Eigenvalues of the molecular orbitals with the three interfacial N-H bonds (depicted in black) fixed, the dark blue line represents the initially occupied excitonic LUMO+2, while the light blue lines represent the charge transfer orbitals LUMO and LUMO+1. No charge transfer is observed.

In photosynthesis, coherent charge and energy transfer has been observed at ambient temperature in complex biological surroundings [3,4,8]. The near unity quantum yield of photon-to-charge conversion in photosynthetic complexes stems from such concerted nuclear motion of the chromophore and a responsive protein matrix [2,22]. The responsiveness lies in the fact that the matrix couples specific vibrations to the photoexcited chromophore that facilitate efficient photoinduced charge separation [3-5,9,23]. Promoting vibrations are also observed in enzyme catalysis [24] and proton displacements play an important role in facilitating electron transfer and preventing charge recombination in photosynthetic charge separation [23]. The coherent coupling between amine stretching vibrations and photoinduced electron transfer in melamine cyanurate (Figure 5.3) illustrates how proton

displacements control the charge transfer in a hydrogen bonded complex. It has recently been shown - with similar TDDFT/LDA simulations - that correlated, coherent motion of ions and electrons drives the first steps of photoinduced electron transfer in an artificial reaction center [7]. We show that even photoexcitation of a DNA base-pair mimic leads to such coherent motion. Based on these results we conclude that such characteristic vibrations involve the nuclear motion at the interface between donor and acceptor. It is tempting to suggest that this oscillatory behaviour is common to photoinduced charge transfer processes. A broader investigation on a range of supramolecular complexes is needed to verify the generality and role of this phenomenon. At the same time these coherences can be optimized to increase the efficiency of photon-to-charge conversion in molecular devices. Interestingly, our results show that when the vibration has an energy that matches the energy difference between exciton and charge transfer states, the charge transfer is initiated and the energies oscillate in quasi-resonance (Figure 5.4).

5.4 Conclusions

We have presented Ehrenfest dynamics simulations describing in real-time the electron transfer in melamine-cyanurate. The photoinduced ET dynamics in this DNA base-pair mimic shows an oscillatory behaviour that is suggested to be a signature of the coupling between electronic states and high frequency vibrational modes associated to hydrogen bonding interactions. When the nuclear coordinates associated to the N-H stretching modes are fixed no charge transfer occurs. We also observe that the transfer is initiated when the energy of the vibration matches the energy difference between exciton and charge transfer state. At this point, the energies are found to oscillate in quasi-resonance.

5.5 References

- [1] D. Gust, T. A. Moore, A. L. Moore, Solar fuels via artificial photosynthesis, *Accounts of chemical research*, **2009**, 42, 1890.
- [2] G. D. Scholes, G. R. Fleming, A. Olaya-Castro, R. van Grondelle, Lessons from nature about solar light harvesting, *Nature Chemistry*, **2011**, 3, 763-774.
- [3] M. H. Vos, F. Rappaport, J. C. Lambry, J. Breton, J. L. Martin, Visualization of coherent nuclear motion in a membrane protein by femtosecond spectroscopy, *Nature*, **1993**, 363, 320-325.
- [4] G. S. Engel, T. R. Calhoun, E. L. Read, T. K. Ahn, T. Mancal, Y. C. Cheng, R. E. Blankenship, G. R. Fleming, Evidence for wavelike energy transfer through quantum coherence in photosynthetic systems, *Nature*, **2007**, 446, 782.
- [5] V. Novoderezhkin, A. Yakovlev, R. van Grondelle, V. Shuvalov, Coherent Nuclear and Electronic Dynamics in Primary Charge Separation in Photosynthetic Reaction Centers: A Redfield Theory Approach, *J. Phys. Chem. B*, **2004**, 108, 7445.
- [6] A. W. Chin, J. Prior, R. Rosenbach, F. Caycedo-Soler, S. F. Huelga and M. B. Plenio, The Role of non-equilibrium vibrational structures in electronic coherence in pigment-protein complexes, *Nature Physics*, **2013**, 9, 113-118.
- [7] C. A. Rozzi, S. M. Falke, N. Spallanzani, A. Rubio, E. Molinari, D. Brida, M. Maiuri, G. Cerullo, H. Schramm, J. Christoffers and C. Lienau, Quantum coherence controls the charge separation in a prototypical artificial light-harvesting system, *Nature communications*, **2013**, 4, 1602.
- [8] Romero, E., Augulis, R., Novoderezhkin, V.I., Ferretti, M., Thieme, J., Zigmantas, D., and van Grondelle, R., Quantum coherence in photosynthesis for efficient solar-energy conversion, *Nature Physics* **2014**, *advanced publication*.
- [9] Fuller, F.D., Pan, J., Gelzinis, A., Butkus, V., Senlik, S.S., Wilcox, D.E., Yocum, C.F., Valkunas, L., Abramavicius, D., and Ogilvie, J.P., Vibronic coherence in oxygenic photosynthesis, *Nature Chemistry* **2014**, 6, 706-711.
- [10] Analysis of charge transfer effects in molecular complexes based on absolutely localized molecular orbitals, R. Z. Khaliullin, A. T. Bell, M. Head-Gordon, *J. Chem. Phys.*, **2008**, 128, 184112.
- [11] L. M. Perdigo, N. R. Champness, P. H. Beton, Surface self-assembly of the cyanuric acid-melamine hydrogen bonded network, *Chem. Commun.*, **2006**, 5, 538-540.
- [12] ADF2012, SCM, Theoretical Chemistry, Vrije Universiteit, Amsterdam, The Netherlands, <http://www.scm.com/>.
- [13] J. P. Perdew and A. Zunger, *Phys. Rev. B*, **1981**, 23, 5048.

5.5. REFERENCES

- [14] X. Andrade, J. Alberdi-Rodriguez, D. A. Strubbe, M. J. T. Oliveira, F. Nogueira, A. Castro, J. Muguerza, A. Arruabarrena, S. G. Louie, A. Aspuru-Guzik, A. Rubio, and M. A. L. Marques, Time-dependent density-functional theory in massively parallel computer architectures: the octopus project, *J. Phys. Cond. Matt.*, **2012**, 24 233202.
- [15] H. Castro, M. O. Appel, C.A. Rozzi, X. Andrade, F. Lorenzen, M.A.L. Marques, E.K.U. Gross, and A. Rubio, "Octopus: A tool for the application of time-dependent density functional theory", *Phys. Stat. Sol. B*, **2006**, 243, 2465-2488.
- [16] M.A.L. Marques, Alberto Castro, George F. Bertsch, and Angel Rubio, "Octopus: a first-principles tool for excited electron-ion dynamics", *Comput. Phys. Commun.*, **2003**, 151, 60-78.
- [17] Castro, M.A.L. Marques, and A. Rubio, Propagators for the time-dependent Kohn-Sham equations, *J. Chem. Phys.*, **2004**, 121, 3425-3433.
- [18] N. Troullier and J. L. Martins, *Phys. Rev. B*, **1991**, 43, 1993-2006.
- [19] M. J. Frisch, et al., Gaussian 09, Revision D.01; Gaussian, Inc.: Wallingford CT, **2009**.
- [20] W. R. Duncan and O. V. Prezhdo, Nonadiabatic Molecular Dynamics Study of Electron Transfer from Alizarin to the Hydrated Ti^{4+} Ion, *J. Phys. Chem. B*, **2005**, 109, 17998-18002.
- [21] X. Andrade, A. Castro, D. Zueco, J. L. Alonso, P. Echenique, F. Falceto and A. Rubio, Modified Ehrenfest Formalism for Efficient Large-Scale ab initio Molecular Dynamics, *J. Chem. Theor. Comp.*, **2009**, 5, 728-742.
- [22] T.J. Eisenmayer, H.J.M. de Groot, E. van de Wetering, J. Neugebauer, F. Buda, Mechanism and Reaction Coordinate of Directional Charge Separation in Bacterial Reaction Centers, *J. Phys. Chem. Lett.*, **2012**, 3, 694.
- [23] T. J. Eisenmayer, J. A. Lasave, A. Monti, H. J. M. de Groot, F. Buda, Proton Displacements Coupled to Primary Electron Transfer in the Rhodobacter sphaeroides Reaction Center, *J. Phys. Chem. B*, **2013**, 117, 38, 11162-11168.
- [24] S. Hay, N. S. Scrutton, Good vibrations in enzyme-catalysed reactions, *Nature Chemistry*, **2012**, 4, 161.

5.6 Appendix I

MOVIE 6.1: "Oscillatory Charge Transfer"

(Click below to see MOVIE)

Left top: Charge on the melamine. **Right top:** Charge on the cyanuric acid.
Bottom panel: Photoinduced spin density along the trajectory.

Appendix II

MOVIE 6.2: "Interfacial N-H bonds fixed: No Charge Transfer"

(Click below to see MOVIE)

Left top: Charge on the melamine. **Right top:** Charge on the cyanuric acid.
Bottom panel: Photoinduced spin density with interfacial N-H bonds fixed.

Chapter 6

Redox Levels and Potentials

6.0.1 ABSTRACT

So far, we have been concerned with the highly optimized photon-to-charge conversion in photosynthetic bacterial reaction centers and a biomimetic system. In plant photosystems photons are not only converted to charges, the photogenerated holes are also utilized for water oxidation. The photosystem II reaction center performs photoinduced charge separation in a similar protein-cofactor architecture as the bacterial reaction center. Yet the mechanism is less understood and the oxidation potential of the primary donor ($P680^+$) is the highest known to biological systems. Only recently, spectroscopic evidence for coherent charge separation processes have been discovered. In this chapter we do not discuss the dynamics of coherent charge transfer in photosystem II. Rather, we show how density functional theory can be used to model large complexes the size of reaction centers and provide a qualitatively correct picture of static redox levels, coupling between chromophores and vertical charge transfer energies. Additionally, we present evidence that the high oxidation potential of P680 implies a very small dielectric constant of the local protein environment.

Parts of this chapter are to be submitted:

T. J. Eisenmayer, J. Marcelis, H. J. M. de Groot and F. Buda, 2014.

6.1 Introduction

Photosystem II (PSII) is the complex that powers the biosphere. Not only does it transform solar irradiation into charge separated states, it also couples this ultrafast process to the relatively slow catalytic cycle of water oxidation, whilst operating at the highest known oxidation potential in biological systems. Only recently (2011) a highly accurate crystal structure of PSII has been resolved [1]. The functioning of PSII has been studied intensively [2-6]. A remarkable difference with the bacterial reaction center (bRC), considered in the previous chapters, is its absorption spectrum [7]. Apart from the fact that the absorption maximum at 680 nm is shifted towards the blue, the PSII absorption band is broad with little fine structure, meaning that all cofactors absorb at approximately the same wavelength. This is in stark contrast with bRCs where the different cofactor pairs ($P_L P_M, B_A B_B$ and $H_A H_B$) exhibit distinct absorption peaks. The electron transfer chain is therefore more easily understood ($P \rightarrow B \rightarrow H$) [8]. In PSII, there may be multiple charge separation pathways that only recently are being uncovered [9,10], and the coherent mixing of charge transfer states into the delocalized excitons due to long-living collective vibrations is recently suggested to be the cause of its high efficiency [11,12,13]. In this Chapter we will not discuss these features, but rather concentrate on the larger supramolecular architecture of the reaction centers using static density functional theory methods to assess the relative energies of frontier orbitals, to calculate charge transfer integrals between cofactor pairs and to assess the energies of the different charge transfer states. Additionally, we discuss the fact that the PSII primary donor has an oxidation potential of ~ 1.2 V [14-16] enabling it to oxidize water, whereas the bRC operates at only 0.5 V [17]. For PSII, we analyze how the oxidation potential of the primary donor is affected by geometrical distortion and by varying the dielectric constant of the environment.

6.2 Models and Methods

The total photosystem II model is extracted from the latest X-ray crystallographic data (PDB-entry 3ARC [1]) and comprises the 4 chlorophyll pigments, 2 pheophytins and the 12 closest surrounding residues (653 atoms in total, see Figure 6.1 and Appendix I for the full list). For this large supramolecular complex we perform density functional theory calculations using the ADF quantum chemical suite [18] at the BLYP/TZP level of theory. The same computational setup is used for a model of bRC (PDB-entry

1M3X) comprising also all the cofactors and the direct protein environment. We also subdivide the total model into 5 smaller cofactor-pair models, including interstitial and surrounding amino acids. We shall refer to these models based on their constituent cofactors: $Pheo_{D1}Chl_{D1}$, $Chl_{D1}P_{D1}$, $P_{D1}P_{D2}$, $P_{D2}Chl_{D2}$ and $Chl_{D2}Pheo_{D2}$.

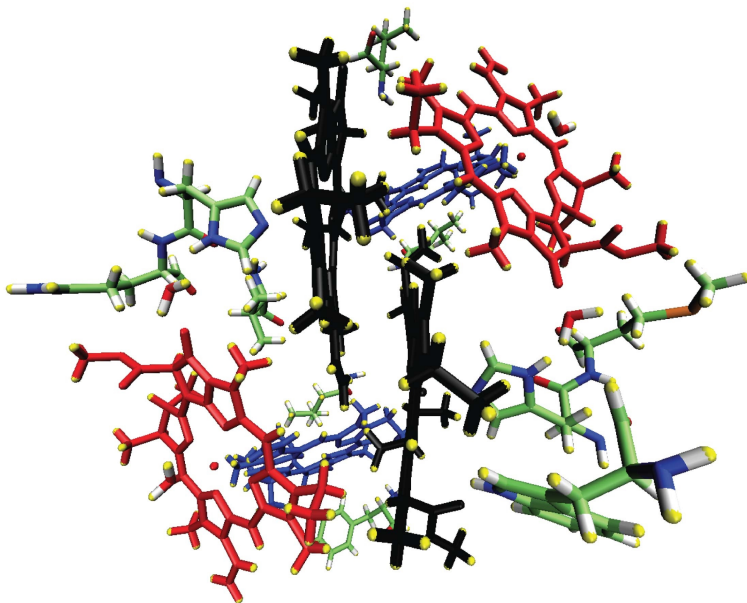


Figure 6.1: Total model of PSII including 653 atoms, 6 cofactors and 12 residues.

From these models we calculate charge transfer integrals between adjacent cofactors with the method of Senthilkumar [19,20] as implemented in ADF at the B3LYP/TZP level. Additionally, we compute the charge transfer energies of the 6 most likely charge transfer configurations in PSII, being $Pheo_{D1}^{-}Chl_{D1}^{+}$, $Chl_{D1}^{-}P_{D1}^{+}$, $P_{D1}^{-}P_{D2}^{+}$, $P_{D1}^{+}P_{D2}^{-}$, $P_{D2}^{+}Chl_{D2}^{-}$ and $Chl_{D2}^{+}Pheo_{D2}^{-}$. These energies are calculated using the method of Wu and van Voorhis [21,22] implemented in the CPMD suite [23], known as constrained DFT (CDFT). Within this formalism the DFT energy is optimized under a charge density constraint corresponding to a cofactor with charge +1 and a cofactor with -1. We use the BLYP functional [24,25] and a plane-wave basis set with an energy cutoff of 70 Ry and employ dispersion-corrected atom-centered pseudopotentials (DCACP) [26,27]. Finally, we extract only the P_{D1} chlorophyll as a model for calculating the

oxidation potential of the primary donor under different solvation conditions as expressed by a range of dielectric constants ($1 < \epsilon < 80$) within the conductor-like screening model (COSMO) [28]. The oxidation potential is calculated by subtracting the energy at the B3LYP/TZP level in the ground state closed-shell system from the energy of the cationic chlorophyll (P_{D1}^+) under the same solvation conditions. This is compared with the bacteriochlorophyll (P_L) of the *Rhodobacter Sphaeroides* reaction center and with undistorted chlorophyll after geometry optimization with ADF at the B3LYP/TZP level.

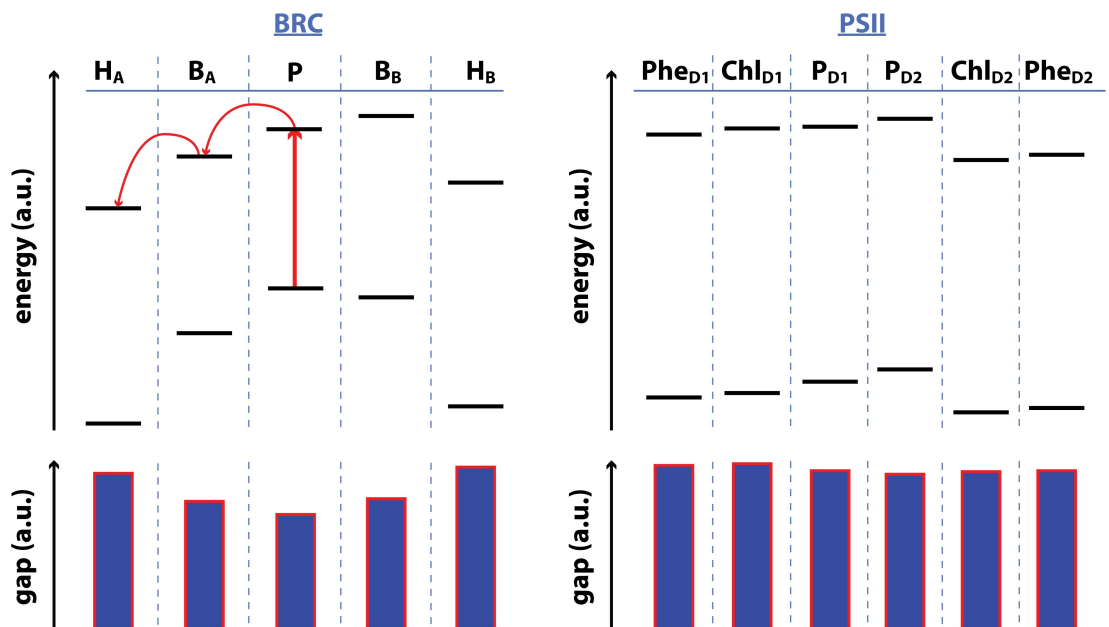


Figure 6.2: HOMO-, LUMO-levels and HOMO-LUMO gaps (vertical bars) for the full model (~ 650 atoms). In the bRC the smallest gap is at the special pair and there is a moderate redox gradient for unidirectional electron transfer (red arrows) while the LUMO on B_B is higher in energy than P . For PSII, the gaps are similar and there is a smaller gradient for unidirectional electron transfer. It is suggested that there is a lower lying LUMO on the D2 branch at Chl_{D2} .

6.3 Results and Discussion

The single-point density optimization of the total PSII model is evaluated by first considering the localization of the frontier orbitals. We find that

6.3. RESULTS AND DISCUSSION

these orbitals are neatly localized on individual cofactors and we can thus associate orbital energies with specific cofactors. This can be done for the highest occupied (HOMO) and lowest unoccupied (LUMO) molecular orbitals. We can then define a local energy gap for every cofactor that is a crude approximation of the 'true' site energy. Notwithstanding the approximate nature of the absolute energies and energy gaps, we are interested in a qualitative description of the electronic structure of the entire complex. Figure 6.2 summarizes the energy gaps and frontier orbital energies for the cofactors in PSII (*right*) and compares these with bRC (*left*). It can be seen that the qualitative picture of the electronic structure of bRC is correct. The special pair (*P*) gap is smallest, the gaps of the two accessory bacteriochlorophylls (*B*) on either side are expectedly larger and of the same magnitude and the gaps of the bacteriopheophytins (*H*) are even larger and also of the same magnitude. This corresponds to the absorption spectrum of bRC [29], where the special pair peak is the most red-shifted, followed by a peak consisting of $B_{A,B}$ and farthest to the blue a peak corresponding to $H_{A,B}$. Therefore, by using the generalized gradient approximation (GGA, i.e. BLYP) for the exchange–correlation energy within DFT one can qualitatively describe the electronic structure of a protein–cofactor complex the size of the bRC (red arrows, Figure 6.2) and make an educated guess about the directionality of the charge separation in the complex along the B-branch [8,29]. If we consider the PSII orbital energies (Figure 6.2, right) and HOMO–LUMO gaps the picture is different, yet qualitatively consistent with the PSII experimental absorption spectrum showing only one broad peak that contains all cofactors [7].

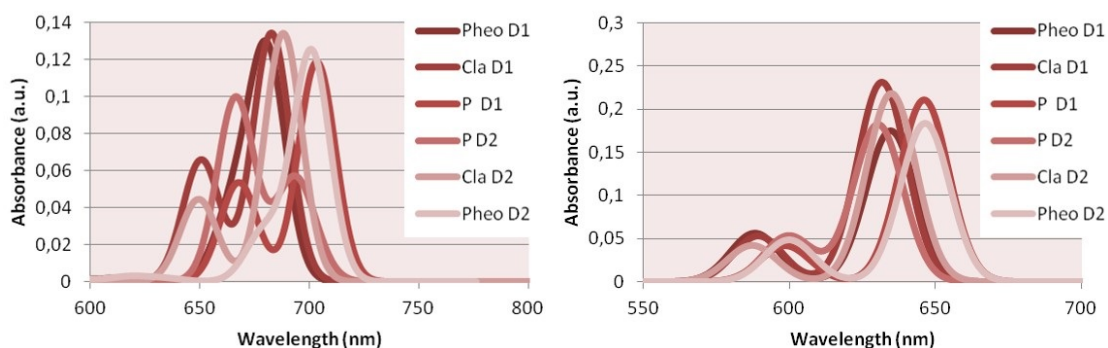


Figure 6.3: TDDFT spectra (*left*: BLYP/TZP, *right*: B3LYP/TZP).

With linear response TDDFT calculations on the 6 cofactor models (with local protein environment included) we are able to reproduce this as shown in Figure 6.3. Interestingly, the BLYP functional provides more accurate site energies centered around 680 nm compared to the hybrid B3LYP functional that overestimates the excitation energies. The narrow range of site-energies in PSII is therefore reproduced and Figure 6.3 clearly illustrates the difference with the electronic structure of bRC. What both reaction centers do have in common is the unidirectionality of electron transfer, despite the twofold-symmetric architectures. Within the orbital energies pictures discussed above a higher LUMO-energy at B_B is observed for bRC and a lower LUMO-energy at Chl_{D2} for PSII. In this static picture these discontinuities in the redox gradients along the inactive branches may be related to the directionality of electron transfer steps. However, dynamic effects would need to be taken into account to substantiate this.

While the orbital energy picture gives some insight into the possible electron transfer paths, also the electron coupling between different cofactors will be considered for the static structure. In Figure 6.4, we show the charge transfer integrals between adjacent cofactor pairs that are a measure for the electronic coupling.

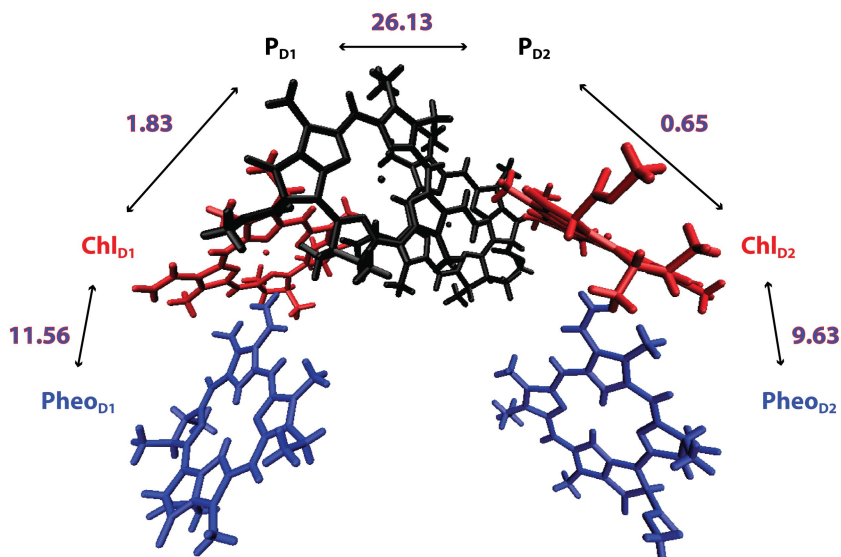


Figure 6.4: Charge transfer integrals between the cofactor LUMO's (meV).

6.3. RESULTS AND DISCUSSION

The magnitude of the charge transfer integrals compares nicely with the related heme-heme macrocycle electronic coupling found to be ~ 10 meV [30]. Our calculations show a strong coupling between the chlorophylls constituting the special pair and weaker couplings with the accessory chlorophylls and pheophytins. By comparing the D1 and D2-branches it can be seen that the coupling strength between the special pair and the accessory Chl_{D2} is significantly lower than with its counterpart on the D1-branch. The center-to-center distances between the special pair chlorophylls and the accessory chlorophylls may contribute to this effect as the $P_{D1} - Chl_{D1}$ distance (10.38 Å) is 0.13 Å shorter than the $P_{D2} - Chl_{D2}$ distance (10.51 Å) according to the latest crystal structure [1]. Another factor of influence may be that the water ($Water_{D1}$) that coordinates to Chl_{D1} is hydrogen bonded to a tryptophan ($Thr179_{D1}$), whereas the water that coordinates to Chl_{D2} has no surrounding residues in its proximity that it can form a hydrogen bond with [1].

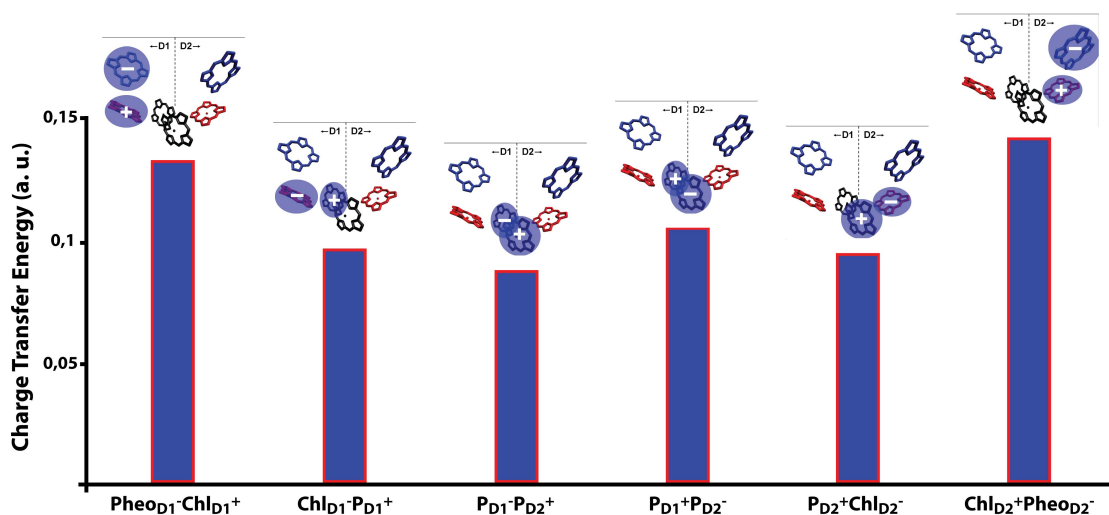


Figure 6.5: Vertical charge transfer energies from constrained DFT of nearest-neighbour cofactor pairs in atomic units, calculated including the direct protein environment. The internal charge transfer state in the special pair with the electron on P_{D1} and the hole on P_{D2} is found to be the lowest in energy.

Where the charge separation in PSII is initiated has been much debated as all site energies are very similar. The charge transfer energies in Figure 6.5 are calculated by constraining a positive charge on one cofactor and a

negative charge on its nearest neighbour. In agreement with the minimum HOMO-LUMO gap for P_{D2} that can be discerned from Figure 6.2, the lowest accessible charge transfer state is found to be internal to the special pair and has a hole on P_{D2} and an electron on P_{D1} ($P_{D1}^+P_{D2}^-$). A proper comparison with the dominant charge separation mechanisms found in ultrafast spectroscopic experiments [9,10,11] would however require dynamic effects, as energy levels are so closely spaced.

How charge transfer states mix into excitonic states in PSII to produce stable charge separated states with high yield is an area of current debate, and likely involves a coherent coupling to vibrational modes [12,13] as we have seen in the bRC. First-principles molecular dynamics simulations as described in the previous chapters and in the following chapter could contribute to a better mechanistic understanding of this process.

6.3.1 Oxidation Potential

The location of the cation, P_{D1}^+ , formed after charge separation is well established [3,31]. We extract the P_{D1} chlorophyll from the latest crystal structure (PDB-entry: 3ARC) and calculate the energy difference between the ground state closed-shell system and the cationic state P_{D1}^+ in vacuum. We repeat this calculation adding a continuous solvent with increasing dielectric constant, resulting in the blue curves in Figure 6.6. In the upper panel we compare PSII with the P_L^+ bacteriochlorophyll of bRC. There is an intrinsic difference in oxidation potential between chlorophyll and bacteriochlorophyll of 0.16 eV [16] that is well reproduced. Interestingly, the oxidation potential of $P680^+$ (PSII) is experimentally found at ~ 1.2 V [14–16], which is a lot larger than $P870^+$ (bRC) at ~ 0.5 V [17] even when the intrinsic difference in potential between bacteriochlorophyll and chlorophyll is taken into account. Taking the curves in the upper panel of Figure 6.6 and relating them to these experimental values implies a very low dielectric constant of $\epsilon \sim 2$ for the local environment of P_{D1} in PSII and a relatively high dielectric constant of $\epsilon \sim 10$ for P_L in bRC. We conclude that the ability of PSII to oxidize water is related to the low dielectric constant of the protein environment surrounding the primary donor in agreement with an earlier DFT-study [32]. This is further substantiated by considering the lower panel in Figure 6.6, where we plot the dependence on the dielectric constant of optimized chlorophyll (light blue line), which does not differ significantly from the results obtained from the distorted chlorophyll extracted from the crystal structure (dark blue line). This suggests that the high ox-

ation potential is not so much due to geometric distortions induced by the protein scaffolding. Rather, electrostatic effects are found to be important.

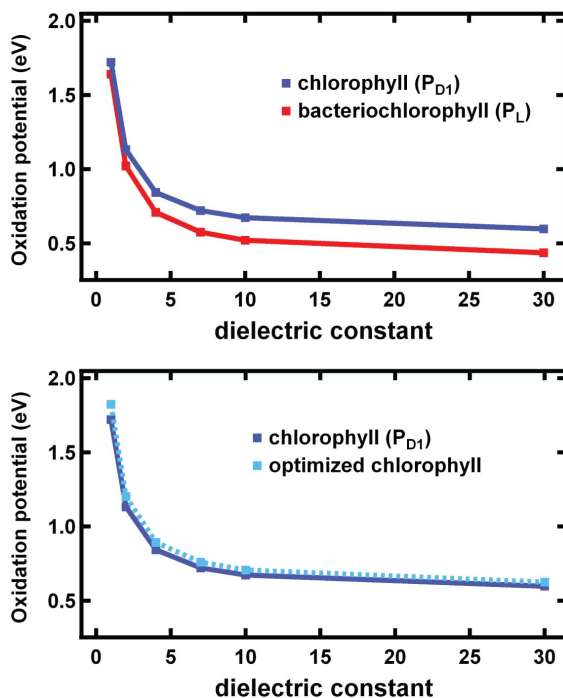


Figure 6.6: Oxidation potential estimated by subtracting the total DFT-energy of the closed-shell system from the oxidized system at the B3LYP/TZP level of theory in a continuous solvent model (COSMO) with varying dielectric constant. The PSII chlorophyll P_{D1} (dark blue line) as extracted from the latest crystal structure (PDB-entry: 3ARC) is compared with the bRC bacteriochlorophyll P_L (red line, PDB-entry 1M3X) and with optimized chlorophyll (light blue line).

6.4 Conclusions

We have used various DFT-based methods to assess site energies, electronic couplings, charge transfer energies and oxidation potentials in PSII and have compared some of these results with the bRC. Overall we find a good agreement with experiment and an insightful qualitative picture of the PSII reaction center. The origin of the high oxidation potential of the PSII primary donor $P680^+$ is suggested to be the low local dielectric constant ($\epsilon \sim 2$) of the protein matrix.

6.5 References

- [1] Umena, Y., Kawakami, K., Shen, J.-R., and Kamiya, N., Crystal structure of oxygen-evolving photosystem II at a resolution of 1.9 Å, *Nature* **2011**, 473, 55-60.
- [2] Durrant, J.R., Klug, D.R., Kwa, S.L., Van Grondelle, R., Porter, G., and Dekker, J.P. A multimer model for P680, the primary electron donor of photosystem II, *PNAS* **1995**, 92, 4798-4802.
- [3] Groot, M.L., Pawlowicz, N.P., van Wilderen, L.J., Breton, J., van Stokkum, I.H., and van Grondelle, R., Initial electron donor and acceptor in isolated photosystem II reaction centers identified with femtosecond mid-IR spectroscopy, *PNAS* **2005**, 102, 13087-13092.
- [4] Holzwarth, A.R., Muller, M.G., Reus, M., Nowaczyk, M., Sander, J., and Rogner, M., Kinetics and mechanism of electron transfer in intact photosystem II and in the isolated reaction center: pheophytin is the primary electron acceptor. *PNAS* **2006**, 103, 6895-6900.
- [5] Diller, A., Roy, E., Gast, P., van Gorkom, H.J., de Groot, H.J., Glaubitz, C., Jeschke, G., Matysik, J., and Alia, A., 15N photochemically induced dynamic nuclear polarization magic-angle spinning NMR analysis of the electron donor of photosystem II, *PNAS* **2007**, 104, 12767-12771.
- [6] Renger, T., and Schlodder, E., Primary Photophysical Processes in Photosystem II: Bridging the Gap between Crystal Structure and Optical Spectra. *ChemPhysChem* **2010**, 11, 1141-1153.
- [7] Konermann, L., and Holzwarth, A.R., Analysis of the absorption spectrum of photosystem II reaction centers: Temperature dependence, pigment assignment, and inhomogeneous broadening, *Biochemistry* **1996**, 35, 829-842.
- [8] Holzappel, W., Finkle, U., Kaiser, W., Oesterhelt, D., Scheer, H., Stiltz, H.U., and Zinth, W., Initial electron-transfer in the reaction center from *Rhodobacter sphaeroides*, *PNAS* **1990**, 87, 5168-5172.
- [9] Romero, E., van Stokkum, I.H.M., Novoderezhkin, V.I., Dekker, J.P., and van Grondelle, R., Two Different Charge Separation Pathways in Photosystem II, *Biochemistry* **2010**, 49, 4300-4307.
- [10] Novoderezhkin, V.I., Romero, E., Dekker, J.P., and van Grondelle, R., Multiple Charge-Separation Pathways in Photosystem II: Modeling of Transient Absorption Kinetics, *ChemPhysChem* **2011**, 12, 681-688.
- [11] Novoderezhkin, V.I., Dekker, J.P., and van Grondelle, R., Mixing of Exciton and Charge-Transfer States in Photosystem II Reaction Centers: Modeling of Stark Spectra with Modified Redfield Theory, *Biophysical Journal* **2007**, 93, 1293-1311.
- [12] Romero, E., Augulis, R., Novoderezhkin, V.I., Ferretti, M., Thieme, J., Zigmantas, D., and van Grondelle, R., Quantum coherence in photosynthesis for

6.5. REFERENCES

- efficient solar-energy conversion, *Nature Physics* **2014**, advanced publication.
- [13] Fuller, F.D., Pan, J., Gelzinis, A., Butkus, V., Senlik, S.S., Wilcox, D.E., Yocum, C.F., Valkunas, L., Abramavicius, D., and Ogilvie, J.P., Vibronic coherence in oxygenic photosynthesis, *Nature Chemistry* **2014**, *6*, 706-711.
- [14] Rappaport, F., Guergova-Kuras, M., Nixon, P.J., Diner, B.A., and Lavergne, J., Kinetics and Pathways of Charge Recombination in Photosystem II, *Biochemistry* **2002**, *41*, 8518-8527.
- [15] Ishikita, H., Loll, B., Biesiadka, J., Saenger, W., and Knapp, E. W., Redox Potentials of Chlorophylls in the Photosystem II Reaction Center, *Biochemistry* **2005**, *44*, 4118-4124.
- [16] Ishikita, H., Saenger, W., Biesiadka, J., Loll, B., and Knapp, E. W., How photosynthetic reaction centers control oxidation power in chlorophyll pairs P680, P700, and P870, *PNAS* **2006**, *103*, 9855-9860.
- [17] X. Lin, H. A. Murchison, V. Nagarajan, W. W. Parson, J. P. Allen, and J. C. Williams, Specific alteration of the oxidation potential of the electron donor in reaction centers from *Rhodobacter sphaeroides*, *PNAS* **1994**, *91*(22), 10265-10269.
- [18] ADF2012, SCM, Theoretical Chemistry, Vrije Universiteit, Amsterdam, The Netherlands, <http://www.scm.com/>.
- [19] K. Senthilkumar, F.C. Grozema, F.M. Bickelhaupt, and L.D.A. Siebbeles, Charge transport in columnar stacked triphenylenes: Effects of conformational fluctuations on charge transfer integrals and site energies, *The Journal of Chemical Physics* **2003**, *119*, 9809.
- [20] K. Senthilkumar, F.C. Grozema, C. Fonseca Guerra, F.M. Bickelhaupt, F.D. Lewis, Y.A. Berlin, M.A. Ratner, and L.D.A. Siebbeles, Absolute Rates of Hole Transfer in DNA, *JACS* **2005**, *127*, 14894.
- [21] Wu, Q.; Van Voorhis, T. Constrained Density Functional Theory and its Application in Long-Range Electron Transfer. *J. Chem. Theory Comput.* **2006**, *2*, 765-774.
- [22] Wu, Q.; Van Voorhis, T. Direct Optimization Method to Study Constrained Systems Within Density-functional Theory. *Phys. Rev. A* **2005**, *72*, 024502.
- [23] CPMD v3.11.1, Copyright IBM Corp, 1990-2008; Copyright MPI für Festkörperforschung Stuttgart, 1997-2001. <http://www.cpmc.org/>.
- [24] Becke, A. D. Density-Functional Exchange-Energy Approximation with Correct Asymptotic Behavior. *Phys. Rev. A* **1988**, *38*, 3096.
- [25] Lee, C.; Yang, W.; Parr, R. G. Development of the Colle-Salvetti Correlation-energy Formula into a Functional of the Electron Density. *Phys. Rev. B* **1988**, *37*, 785.

- [26] von Lilienfeld, O. A.; Tavernelli, I.; Rothlisberger, U.; Sebastiani, D. Optimization of Effective Atom Centered Potentials for London Dispersion Forces in Density Functional Theory. *Phys. Rev. Lett.* **2004**, 93, 153004.
- [27] von Lilienfeld, O. A.; Tavernelli, I.; Rothlisberger, U.; Sebastiani, D. Performance of Optimized Atom-centered Potentials for Weakly Bonded Systems Using Density Functional Theory. *Phys. Rev. B* **2005**, 71, 195119.
- [28] C.C. Pye and T. Ziegler, An implementation of the conductor-like screening model of solvation within the Amsterdam density functional package, *Theoretical Chemistry Accounts* **1999**, 101, 396.
- [29] M. A. Steffen, K. Lao, and S. G. Boxer, Dielectric Asymmetry in the Photosynthetic Reaction Center, *Science* **1994**, 264 (5160), 810-816.
- [30] Smith, D. M. A.; Rosso, K. M.; Dupuis, M.; Valiev, M.; Straatsma, T. P., Electronic Coupling between Heme Electron-Transfer Centers and Its Decay with Distance Depends Strongly on Relative Orientation, *J. Phys. Chem. B* **2006**, 110, 15582-15588.
- [31] Saito, K., Ishida, T., Sugiura, M., Kawakami, K., Umena, Y., Kamiya, N., Shen, J.-R., and Ishikita, H., Distribution of the Cationic State over the Chlorophyll Pair of the Photosystem II Reaction Center, *JACS* **2011**, 133, 14379-14388.
- [32] Hasegawa, K., and Noguchi, T., Density Functional Theory Calculations on the Dielectric Constant Dependence of the Oxidation Potential of Chlorophyll: Implication for the High Potential of P680 in Photosystem II, *Biochemistry* **2005**, 44, 8865-8872.

6.6 Appendix I

List of residues comprising the total PSII model:

Cofactors:

P_{D1} (CLA 604), P_{D2} (CLA 605), Chl_{D1} (CLA 606), Chl_{D2} (CLA 607), $Pheo_{D1}$ (PHO 608), $Pheo_{D2}$ (PHO 609).

Amino acids coordinated to cofactors:

His_{D1} coordinated to P_{D1} (HIS 198), His_{D2} coordinated to P_{D2} (HIS 197), $Water_{D1}$ coordinated to Chl_{D1} (HOH 1003), $Water_{D2}$ coordinated to Chl_{D2} (HOH 1009), Leu_{D1} coordinated to $Pheo_{D1}$ (LEU 209), Leu_{D1} coordinated to $Pheo_{D1}$ (LEU 210).

Other residues:

LEU 151, PHE 146, MET 198, HOH 382, TRP 191, HOH 349, GLN 199, VAL 202.

Chapter 7

Proton-Coupled Electron Transfer

7.0.1 ABSTRACT

Proton-coupled electron transfer is a fundamental processes in nature, most noticeably in photosynthesis. Within the adiabatic molecular dynamics approach we present real-time evidence of proton-coupled electron transfer upon oxidation of a benzimidazole-phenol redox relay. The decoupling of spin and positive charge observed in this system may be an important motif to mediate between the fast charge separation and slower water oxidation catalysis in artificial photosynthesis.

Parts of this chapter were published in:

T. J. Eisenmayer and F. Buda, "Real-time Simulations of Photoinduced Coherent Charge Transfer and Proton-Coupled Electron Transfer", *ChemPhysChem*, 2014.

DOI: 10.1002/cphc.201402444

7.1 Introduction

Proton coupled electron transfer (PCET) is a fundamental process in many biochemical reactions and molecular electronic device functions [1-3]. Also in the oxygen evolving complex (OEC) of Photosystem II successive PCET reaction steps are crucially important to overcome the thermodynamically demanding water splitting reaction avoiding the accumulation of excess positive charge in the manganese cluster [4]. Moreover, in Photosystem II a tyrosine-histidine pair mediates the electron transfer between the OEC and the radical cation $P680^{\bullet+}$ and provides a kinetic intermediate between the slow catalytic water oxidation steps and the fast photoinduced charge transfer through an intermolecular PCET process (Figure 7.1) [5,6].

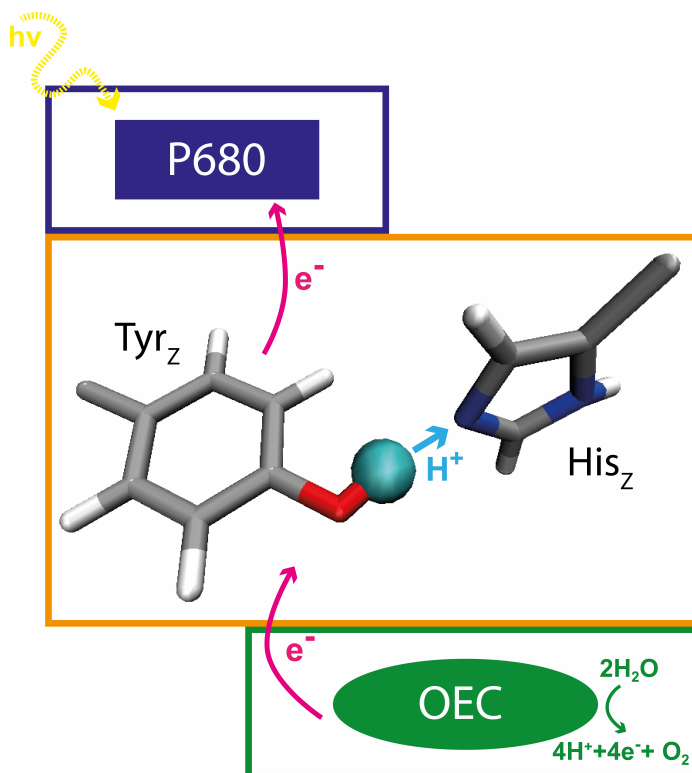


Figure 7.1: Redox mediation between the lightactive P680 pigments and the oxygen evolving complex (OEC): A proton is transferred from Tyrosine_Z to the imidazole ring of Histidine_Z upon oxidation of the tyrosine.

We present ab initio molecular dynamics simulations of the benzimidazole-phenol redox relay recently included in an artificial triad for efficient charge separation [6] and show real-time evidence of the PCET process induced by oxidation of the benzimidazole-phenol that leads to the formation of the stable phenoxyl radical.

7.2 Model and Methods

The real-time simulations of proton-coupled electron transfer were performed on a single adiabatic potential energy surface. The model we study is a benzimidazole-phenol (Figure 7.2) that mimics the tyrosine-histidine pair in Photosystem II [6]. In analogy with natural photosynthesis the PCET from the phenol to the benzimidazole can prevent charge recombination by stabilizing the photoinduced hole. To simulate the PCET process in real-time we use the Car-Parrinello method as implemented in the CPMD code [7,8]. The total time of the trajectories is 5 ps with a time step of 0.1 fs. A Nosé thermostat is used in all simulations to keep the temperature around an average of 300 K. At this temperature we expect that quantum effects on the proton dynamics are not dominant and that the classical description of the nuclear motion is appropriate.

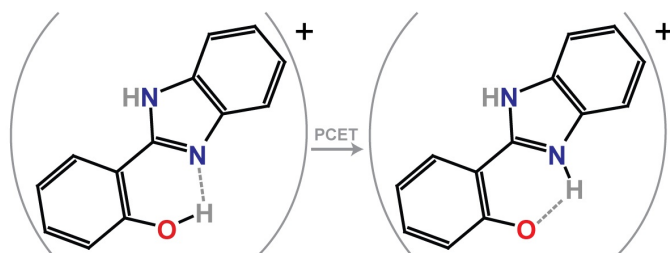


Figure 7.2: Proton-coupled electron transfer in benzimidazole-phenol upon (photoinduced) oxidation.

The BLYP functional [9,10] is used for the exchange-correlation energy. The Kohn-Sham orbitals are expanded in a plane-wave basis set with an energy cutoff of 70 Ry. We employ dispersion-corrected atom-centered (DCACP) pseudopotentials [11,12]. Starting from a partially optimized structure with the proton on the phenol (Figure 7.3), we follow the dynamics of the proton and the unpaired electron in real-time. The unpaired electron is tracked

along the trajectories by monitoring the hole spin density (HSD):

$$HSD(r) = \rho^\beta(r) - \rho^\alpha(r) \quad (7.1)$$

where ρ represents the density, and α, β the respective spin species. The total integral over space of the HSD equals 1. By integrating the HSD over different partitions of the simulation box we quantify the localization of the unpaired electron. We perform CPMD simulations both in vacuum and in the presence of an explicit water solvent.

7.3 Results and Discussion

In many natural processes and most noticeably in photosynthesis electron transfer is often accompanied by a concerted proton motion that reduces the probability of charge recombination. Moreover the tyrosine-histidine redox mediator in Photosystem II becomes an extremely long lived neutral radical after removing the hole from the special pair. As such it facilitates the kinetically demanding water oxidation in the oxygen evolving complex [5]. To simulate the proton-coupled electron transfer in the benzimidazole-phenol mimic of this redox mediator, we perform ab initio molecular dynamics simulations in the state after electron injection to an acceptor. In this configuration the proton is still attached to the phenol oxygen. After 180 fs of dynamical evolution we observe a first attempt of a proton transfer to the imidazole nitrogen (Figure 7.3, upper left panel, 0.2 ps). This unsuccessful approach is at the end of the first characteristic fluctuation of the hydrogen bond. After another full period of this oscillation the proton is transferred to the imidazole nitrogen (~ 0.5 ps). The proton remains stable in this configuration during the entire simulation (5 ps) even though we still observe hydrogen bond dynamics that moves the proton close (1.3 Å) to the phenoxyl oxygen radical (see upper left panel ~ 0.8 ps). Initially the hole spin density is delocalized over the entire complex (Figure 7.3, lower left). After the proton transfer (0.6 ps) the spin density localizes on the phenol with a modified nodal structure forming a phenoxyl neutral radical (Figure 7.3, upper right). The integrated spin density on the phenol ring in the lower right panel of Figure 7.3 quantifies the spin transfer along the dynamics. Clearly, the spin density rearranges in a concerted fashion with the proton dynamics (Figure 7.3 upper left) and approaches unity as the proton is transferred to the imidazole nitrogen.

7.3. RESULTS AND DISCUSSION

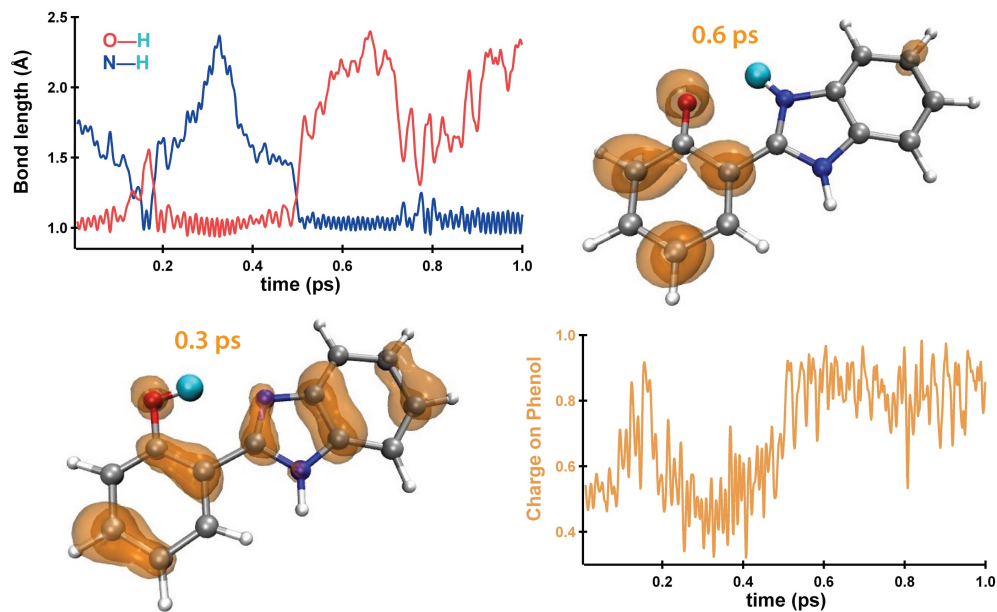


Figure 7.3: Real-time simulation of proton-coupled electron transfer in a mimic of the tyrosine-histidine pair in PSII (See Movie 7.1 in Appendix I). We start the ab initio molecular dynamics in the configuration of the benzimidazole-phenol immediately after oxidation. The upper left panel tracks the distance of the proton with respect to the phenol (O) and imidazole (N). We observe the proton transfer after ~ 0.5 ps. The hole spin density (orange) almost entirely localizes on the phenol as the proton is transferred under formation of a phenoxyl neutral radical (upper right panel). The symmetry of the unpaired electron changes with a modified nodal structure (compare lower left and upper right panels). When integrating the spin (*errata: NOT charge as on y-axes*) on the phenol as the simulation proceeds (lower right panel) the spin density on the phenol follows the proton motion and approximates unity after the proton transfer.

To investigate the possibility of a solvent mediated proton transfer in benzimidazole-phenol we perform ab initio molecular dynamics with an explicit water solvation shell and periodic boundary conditions. We start from the same initial conditions of the redox mediator as in the vacuum simulations and evolve the system starting with the proton attached to the phenolic oxygen. The proton transfer occurs on a significantly longer time scale with the inclusion of an explicit solvent (see Figure 7.4). Moreover the thermal fluctuations of the intramolecular hydrogen bond are damped by the formation of hydrogen bonds with the solvent. As we established in

the simulation for the isolated system, the fluctuations of the intermolecular hydrogen bond are crucial in facilitating the proton transfer. The reduced amplitude of these fluctuations in the presence of the solvent decreases the probability for the proton to be transferred to the imidazole. Water-assisted proton transfer through the temporary formation of a hydronium ion is not observed. In terms of hole spin density the symmetry before and after proton transfer changes in the same fashion as in vacuum. The nodal structure is modified and the localization is now almost entirely on the phenol that becomes a neutral phenoxyl radical (Figure 7.4, bottom panels).

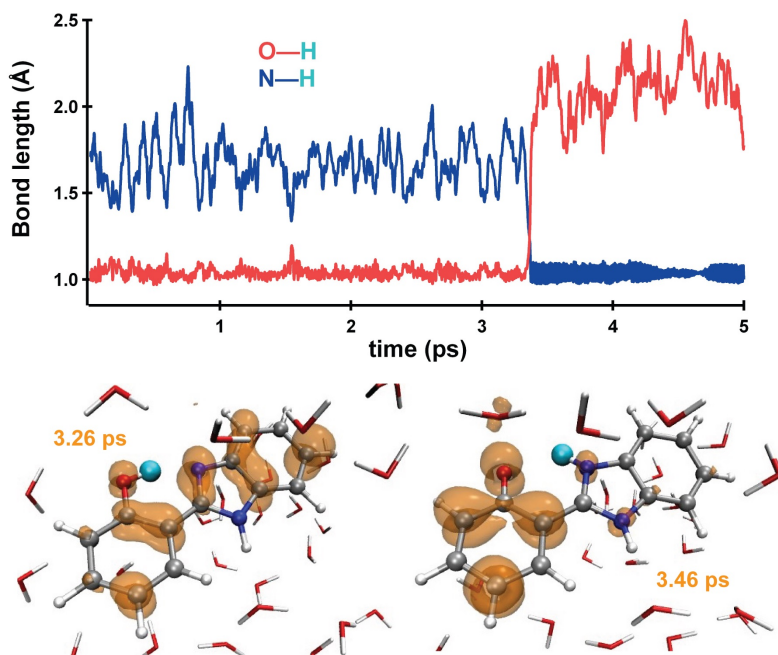


Figure 7.4: Proton-coupled electron transfer simulation with explicit water solvent. We find almost an order of magnitude slower proton transfer with respect to the simulations in vacuum (upper panel), which we attribute to hydrogen bonding between the proton and the solvent. The delocalized hole spin density before proton transfer (lower left panel) localizes on the phenol after proton transfer (lower right panel) and a phenoxyl neutral radical is formed.

Small fractions of spin density are also observed on water molecules further indicating the hydrogen bonding interaction with the solvent. We observe that the out-of-plane motion between the imidazole and phenol moieties is limited to a range of a few degrees ($+5$, -5) due to the presence of an

intramolecular hydrogen bond, consistently with experimental findings. [6] We find that the fluctuations in this dihedral angle are coupled to the proton transfer since they are associated with fluctuations in the distance between the proton donor and proton acceptor.

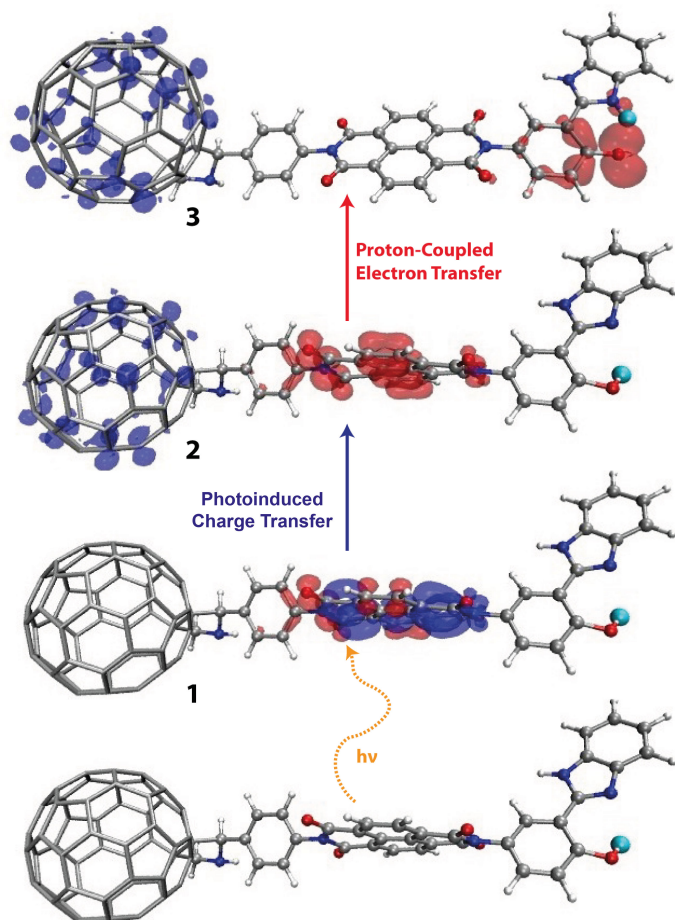


Figure 7.5: Artificial photosynthetic assembly consisting of a fullerene acceptor, a naphthalene diimide antenna and a benzimidazole-phenol electron donor. The latter will prevent charge recombination by filling the hole on the antenna that is formed after photoinduced charge transfer to the acceptor. Once oxidized, the donor will transfer a proton from the phenolic moiety to the imidazole through a proton-coupled electron transfer step. Depicted are the photoinduced spin densities (blue=electron, red=hole) after short TDDFT trajectories in the excitonic state (1), the intermediate charge transfer state (2) and the fully charge separated state (3) where the proton has been transferred to the imidazole.

7.3.1 Artificial Reaction Center

The concept and realization of an artificial reaction center for stable photoinduced charge separation based on properly chosen molecular building blocks has been developed for many years [13]. It is generally accepted that such supramolecular complexes should comprise at least three components (triad) with a light sensitive antenna molecule coupled to a donor and an acceptor to reach a charge separated state that lives long enough to support the kinetically demanding redox catalytic steps. One of the most studied triads in the literature is the carotenoid-porphyrin-fullerene complex [14] where ultrafast charge transfer dynamics have been observed with femtosecond spectroscopy [15]. Following a similar strategy as in Reference [13], we explore a triad including a fullerene acceptor, a naphthalene diimide (NDI) antenna and the benzimidazole-phenol (BiP) moiety discussed in the previous section as electron donor (see Figure 7.5). The NDI antenna is very versatile since it can be functionalized with different groups to adjust its optical and electronic properties [16,17]. This allows to control the molecular absorption range and to adapt the molecular redox properties to specific interface requirements. The BiP relay module is included in the triad to stabilize the charge separated state through the formation of the phenoxyl radical. We have verified that this radical state is accessible in the triad upon charge separation (see Figure 7.5, top). We are planning to perform long real time Ehrenfest dynamics simulations of the triad starting from the excitonic state to follow the full electron/hole transfer and the PCET step. These simulations should allow also to establish whether coherent motion might play a role in this supramolecular complex similarly to what has been observed in the carotenoid-porphyrin-C60 complex [15] and in Chapter 5 of this thesis [18].

7.4 Conclusions

We have presented ab-initio molecular dynamics simulations describing in real-time the proton-coupled electron transfer process in benzimidazole-phenol. The dynamics in this mimic of the tyrosine-histidine pair in PSII shows the proton transfer from the phenolic oxygen to the imidazole nitrogen upon oxidation. The proton dynamics is strongly coupled to the hole spin density that localizes on the phenol leading to the formation of the stable phenoxyl radical. Incorporating the decoupling of spin and charge in an artificial device has the potential to bridge the timescales between the fast photoinduced processes and catalysis.

7.5 References

- [1] S. Hammes-Schiffer, A.V. Soudackov, Proton-coupled electron transfer in solution, proteins, and electrochemistry, *J. Phys. Chem. B*, **2008**, 112 (45), 14108-14123.
- [2] S. Hammes-Schiffer, Theory of Proton-Coupled Electron Transfer in Energy Conversion Processes, *Acc. Chem. Res.*, **2009**, 42 (12), 1881-1889.
- [3] C. Ko and S. Hammes-Schiffer, Charge-transfer excited states and proton transfer in model guanine-cytosine DNA duplexes in water, *J. Phys. Chem. Lett.*, **2013**, 4, 2540-2545.
- [4] H. Dau, C. Limberg, T. Reier, M. Risch, S. Roggan, P. Strasser, The Mechanism of Water Oxidation: From Electrolysis via Homogeneous to Biological Catalysis, *ChemCatChem*, **2010**, 2, 724-761.
- [5] L. Hammarstrom and S. Styring, Proton-coupled electron transfer of tyrosines in photosystem II and model systems for artificial photosynthesis: the role of a redox-active link between catalyst and photosensitizer, *Energy Environ. Sci.*, **2011**, 4, 2379-2388.
- [6] J. D. Megiatto Jr, D. D. Mendez-Hernandez, M. E. Tejada-Ferrari, A. Teillout, M. J. Llansola-Portoles, G. Kodis, O. G. Poluektov, T. Rajh, V. Mujica, T. L. Groy, D. Gust, T. A. Moore & A. L. Moore, A bioinspired redox relay that mimics radical interactions of the Tyr-His pairs of photosystem II, *Nature Chemistry*, **2014**, 6, 423-428.
- [7] CPMD v3.11.1, Copyright IBM Corp, 1990-2008; Copyright MPI fur Festkorperschaft Stuttgart, 1997-2001; <http://www.cpmd.org/>.
- [8] R. Car, M. Parrinello, Unified Approach for Molecular Dynamics and Density-Functional Theory, *Phys. Rev. Lett.*, **1985**, 55, 2471.
- [9] D. Becke, *Phys. Rev. A*, **1988**, 38, 3098.
- [10] T. Lee, W.T. Yang, R. G. Parr, Development of the Colle-Salvetti Correlation-energy Formula into a Functional of the Electron Density, *Phys. Rev. B*, **1988**, 37, 785.
- [11] O. A. von Lilienfeld, I. Tavernelli, U. Rothlisberger, D. Sebastiani, Optimization of Effective Atom Centered Potentials for London Dispersion Forces in Density Functional Theory, *Phys Rev. Lett.*, **2004**, 93, 153004.
- [12] O. A. von Lilienfeld, I. Tavernelli, U. Rothlisberger, D. Sebastiani, Performance of Optimized Atom-centered Potentials for Weakly Bonded Systems Using Density Functional Theory, *Phys. Rev. B*, **2005**, 71, 195119.
- [13] D. Gust, T. A. Moore, A. L. Moore, Solar fuels via artificial photosynthesis, *Accounts of chemical research*, **2009**, 42, 1890.
- [14] G. Kodis, P. A. Liddell, A. L. Moore, T. A. Moore and D. Gust, Synthesis and photochemistry of a carotene-porphyrin-fullerene model photosynthetic reaction center. *J. Phys. Org. Chem.*, **2004**, 17, 724-734.

- [15] C. A. Rozzi, S. M. Falke, N. Spallanzani, A. Rubio, E. Molinari, D. Brida, M. Maiuri, G. Cerullo, H. Schramm, J. Christoffers and C. Lienau, Quantum coherence controls the charge separation in a prototypical artificial light-harvesting system, *Nature communications*, **2013**, 4, 1602.
- [16] N. Sakai, J. Mareda, E. Vauthey, S. Matile, Core-Substituted Naphthalenediimides, *Chem. Commun.*, **2010**, 46, 4225-4237
- [17] S. V. Bhosale, C. H. Jani, S. J. Langford, Chemistry of naphthalene diimides, *Chem. Soc. Rev.*, **2008**, 37, 331.
- [18] T.J. Eisenmayer, F. Buda, Real-time Simulations of Photoinduced Coherent Charge Transfer and Proton-Coupled Electron Transfer, published online 15 September 2014, **2014**, 15 (15), pp 3258-3263.

Chapter 8

Conclusions and Outlook

8.1 Conclusions

The special pair in bacterial photosynthesis, where excitons evolve into charge transfer states at near unity efficiency, has been modeled using first-principles molecular dynamics to elucidate the relationship between nuclear motion and electronic structure. The frontier molecular orbitals are found to dynamically localize over the two halves of the special pair dimer induced by specific vibrational modes. One specific vibration is predicted to couple to the excitation involving a histidine coordinated to one half of the pair (P_M) closest to the primary acceptor. Full charge separation is most likely effectuated by proton displacements in the hydrogen bond network surrounding an interstitial water between primary donor and acceptor.

A coherent coupling between nuclear motion and charge transfer is also observed in a biomimetic system with the donor and acceptor moieties held together by hydrogen bonds. In this system the oscillatory photoinduced charge transfer starting from an excitonic state is simulated in real-time within a time-dependent Kohn-Sham formulation of Ehrenfest dynamics. High frequency N-H bond stretching is found to have the same oscillatory period as observed in the charge transfer from donor to acceptor. Furthermore, the energies of the excitonic and charge transfer states oscillate in quasi-resonance once the energy difference between the states matches the energy contained in the vibrational mode and it appears that only when this criterium is met the charge transfer is initiated.

Static density functional theory calculations on a large model of Photosystem II are found to provide an insightful picture of redox levels. The high oxidation potential observed for the reaction center is postulated to emanate from the low dielectric constant of the local protein environment around the special pair chlorophyll P_{D1} .

Finally, a promising system to bridge timescales between photoinduced charge separation and water oxidation catalysis that mimics photosynthetic redox mediation was considered. The proton-coupled electron transfer step that decouples spin and charge in this system upon oxidation was simulated in real-time illustrating a periodic collective motion of the molecule that facilitates the transfer of the proton.

8.2 Outlook

In much of chemistry the motion of the nuclei does not change the quantum mechanical state of the system. This is true for reactant and product states in chemical reactions that are characterized by two different probability densities pertaining to different regions of conformational space of a single quantum mechanical ground state. Then the adiabatic or Born-Oppenheimer approximation holds [1]. Nevertheless, nuclear motion is required to move between the different regions of conformational space. This motion, the so-called reaction coordinate, is often unknown and unspecified.

Starting in the metastable reactant state the nuclear motion to overcome the potential energy barrier and move into the product state is thought to be random or thermal, with temperature being the decisive parameter. However, a potential energy barrier is not a preordained quantity, it crucially depends on the nature of the nuclear motion or reaction coordinate that is chosen by the system to evolve the reactant into the product state.

In this respect, there are several interesting developments suggesting that specific nuclear vibrational modes may be used by enzymes to lower reaction barriers ([2]) or that nuclear motion plays a role in promoting catalytic product formation on surfaces [3]. In this thesis in Chapter 7 it was seen that proton transfer on a single adiabatic potential energy surface was effectuated after several periods of a collective nuclear motion of the molecule in vacuo. The collective nuclear motion in the explicitly solvated simulation was less pronounced and the transfer was almost an order of magnitude slower. It will be interesting to further examine how one can lower the potential energy barrier for chemical product formation through specific periodic motion of the nuclei.

The crucial point in this thesis and the most interesting research direction to pursue is beyond the adiabatic approximation, when multiple quantum mechanical states are non-negligibly coupled. This is the nonadiabatic realm that needs to be explored in order to meet with the societal demand for energy from non-depletable resources.

Consider a two-level system consisting of an excitonic and a charge transfer state coupled through periodic nuclear motion in Dirac's representation of Quantum Mechanics. Such two-level systems subject to an external time-dependent perturbation describe, for example, NMR and laser-induced Rabi oscillations. In Chapter 5 it was found that the energies of the exciton and charge transfer states oscillate in quasi-resonance during the photoinduced charge transfer, while in the frameworks of NMR and Rabi the energies of the states are constant. A smart strategy to deal with this is needed that may involve choosing a reference frame that rotates with the oscillatory perturbation. If the perturbation may be described by a sinusoidal function it can be decomposed into complex exponentials. Further simplification may be achieved if one of these terms cancels with a possible physical interpretation that the electronic system follows the nuclear motion only in a single direction in the complex plane.

An interesting computational development is the efficient implementation of time-dependent Kohn-Sham in the OCTOPUS quantum-chemical suite allowing real-time simulations of excited supramolecular complexes [4]. The Ehrenfest method for coupling the electronic quantum system and the classical nuclear motion seems to correctly predict the coherent nuclear motion that couples to photoinduced charge separation [5,6]. However, the method has limitations as the system will not fully collapse onto a pure eigenstate of the Hamiltonian and in the limit of long timescales no proper thermal equilibrium is reached [7,8]. Therefore, a firm theoretical foundation - possibly following Scully [9] - is needed to guide numerical simulations and experiments towards efficient systems for solar energy transduction.

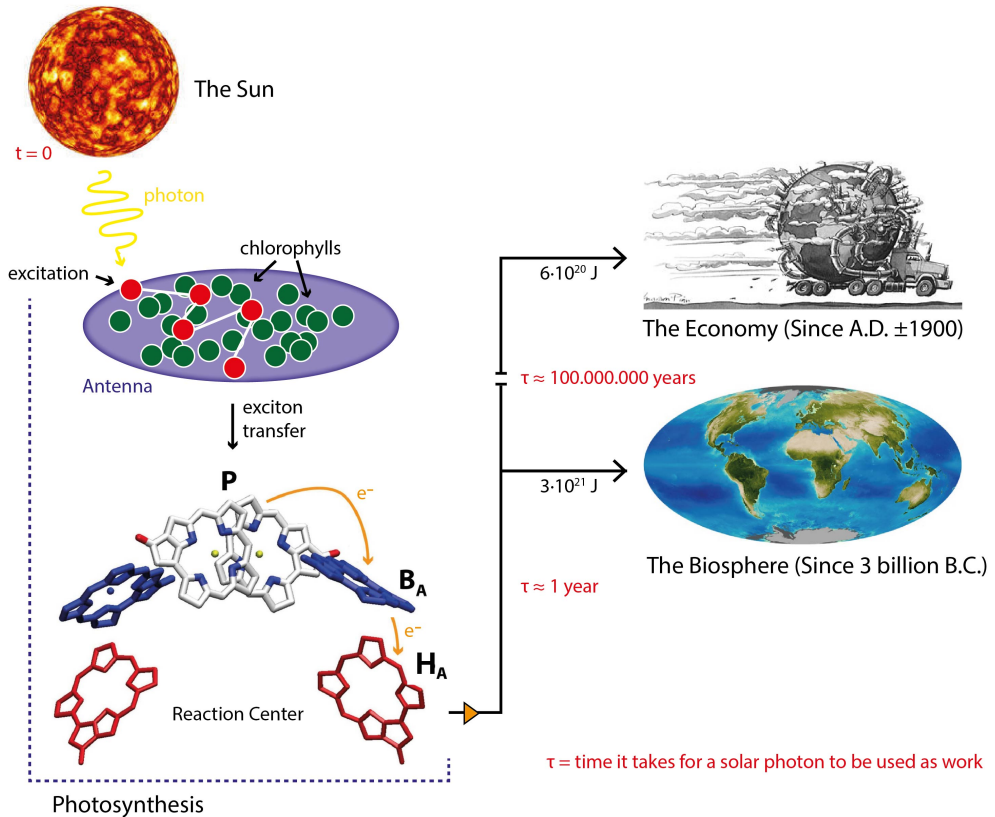
8.3 References

- [1] Max Born and J. Robert Oppenheimer, "Zur Quantentheorie der Molekeln", *Annalen der Physik*, **1927**, 389 (20), 457-484.
- [2] S. Hay, N. S Scrutton, Good vibrations in enzyme-catalysed reactions, *Nature Chemistry*, **2012**, 4, 161.

- [3] H. Hou, S. J. Gulding, C. T. Rettner, A. M. Wodtke, and D. J. Auerbach, The Stereodynamics of a Gas-Surface Reaction, *Science*, **1997**, 277 (5322), 80-82.
- [4] X. Andrade, J. Alberdi-Rodriguez, D. A. Strubbe, M. J. T. Oliveira, F. Nogueira, A. Castro, J. Muguerza, A. Arruabarrena, S. G. Louie, A. Aspuru-Guzik, A. Rubio, and M. A. L. Marques, Time-dependent density-functional theory in massively parallel computer architectures: the octopus project, *J. Phys. Cond. Matt.*, **2012**, 24 233202.
- [5] C. A. Rozzi, S. M. Falke, N. Spallanzani, A. Rubio, E. Molinari, D. Brida, M. Maiuri, G. Cerullo, H. Schramm, J. Christoffers and C. Lienau, Quantum coherence controls the charge separation in a prototypical artificial light-harvesting system, *Nature communications*, **2013**, 4, 1602.
- [6] S. M. Falke, C. A. Rozzi, D. Brida, M. Maiuri, M. Amato, E. Sommer, A. De Sio, A. Rubio, G. Cerullo, E. Molinari, and C. Lienau, Coherent ultrafast charge transfer in an organic photovoltaic blend, *Science*, **2014**, 344, 1001-1005.
- [7] A. V. Akimov, A. J. Neukirch and O. V. Prezhdo, Theoretical Insights into Photoinduced Charge Transfer and Catalysis at Oxide Interfaces, *Chemical Reviews*, **2013**, 6, 4496.
- [8] J. C. Tully, Perspective: Nonadiabatic Dynamics Theory, *J. Chem. Phys.*, **2012**, 137, 22301.
- [9] Marlan O. Scully, Quantum Photocell: Using Quantum Coherence to Reduce Radiative Recombination and Increase Efficiency, *Physical Review Letters*, **2010**, 104, 207701.

Summary

The motivation for this work is the Energy Conundrum depicted below. Simply stated, all energy on earth comes from the sun and is emitted through radiation.¹ This energy is used to power both the economy and all living organisms, collectively referred to as the biosphere. The light-to-electricity conversion is the crucial step in the energy transduction and is performed by photosynthesis. The time it takes between the emission of solar radiation and the utilization of the energy in the economy is approximately a hundred million years. In the biosphere the same is achieved within a single year.



¹Nuclear energy excluded.

Coincidentally, the energy conundrum started taking shape at the same time (A.D.±1900) as the fundamental physical description of light and matter that is the theory of Quantum Mechanics. The prefix quantum was added to Newton's theory of mechanics to represent the fact that light and matter consist of specific quantum states that do not form a classical continuum. Oddly, a quantum system can be in multiple states simultaneously called a *superposition*. Sunlight consists of quantum mechanical packets of energy, photons. These can only be absorbed when their energy matches the energy difference between two quantum mechanical states of matter. Considering the building blocks of matter, positive nuclei and negative electrons, the higher energy state of matter that is populated by the absorption of a photon is a positive nucleus surrounded by a high energy electron collectively called an exciton.

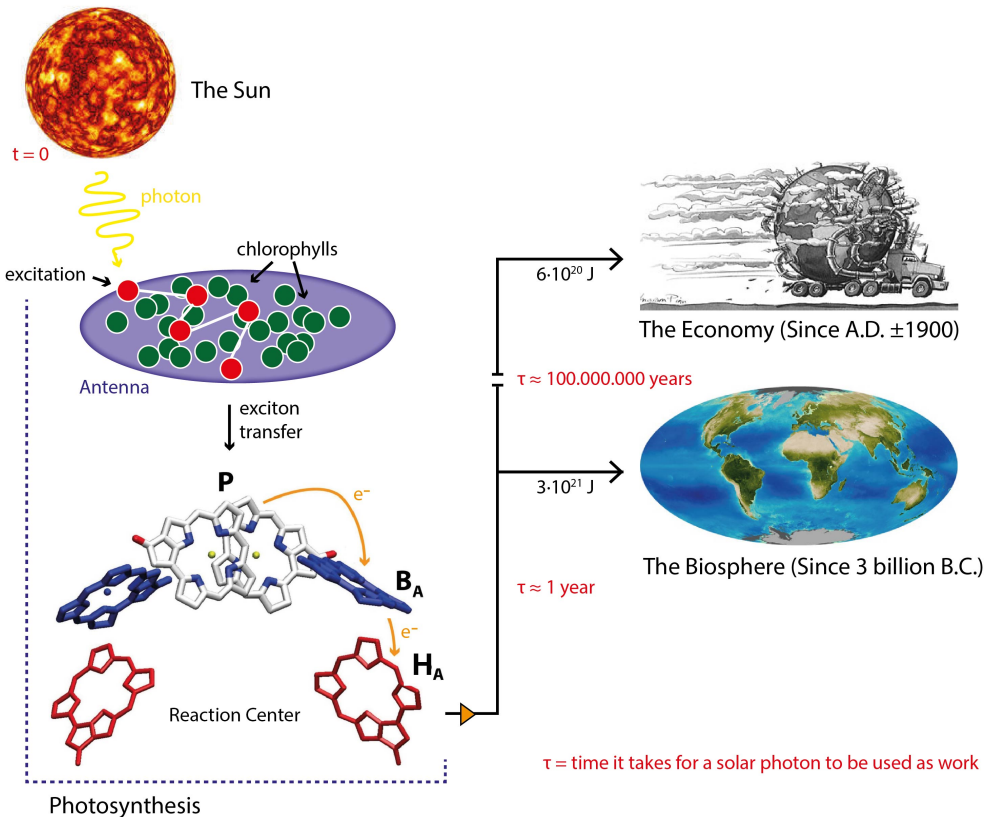
The exciton is of no practical use for generating electricity. Left alone, this higher energy state will lose its energy and decay back to the original state through the emission of a photon. The challenge is to populate a different quantum mechanical state where the high energy electron is spatially separated from the positive nucleus, a so-called charge transfer state.² As nuclei are much heavier than electrons their movements are usually disregarded during the separation of charges. The crucial point in this thesis is that nuclear movements need to be accounted for as they drive the transitions between quantum states and ultimately determine the efficiency of solar energy transduction. Nuclear motion is said to be *coherent* when it induces a superposition of quantum states. In photosynthesis, evolution has optimized solar energy transduction by developing complex molecular structures that preserve coherence and allow single nuclear vibrations to drive the highly efficient separation of charges (**Chapters 3 and 4**). The condition for nuclear motion to coherently drive one state into another is called *resonance* and involves a matching of the energy contained in the vibration and the energy difference between the states. When satisfied, the energies of the states cross with the frequency of the coherent vibration and the initial state is gradually transformed into the final state (**Chapter 5**).

In summary, quantum technologies for solar energy transduction beyond the classical efficiency limit are possible (**Chapter 8, Outlook**). Left unpatented, such technologies can raise living standards and promote equality.

²Once this challenge is met an electric current can be generated from the negative to the positive regions. The economy can be imagined as a resistance in this electrical circuit and its energy demands can be directly supplied from the sun.

Samenvatting

De aanleiding voor dit werk is het energievraagstuk dat hieronder schematisch is weergegeven. De zon voorziet de economie en alle levenden organismen genaamd biosfeer van energie uit licht.¹ De omzetting van zonlicht naar elektrische potentiaal is de cruciale conversiestap in dit proces en wordt uitgevoerd door de fotosynthese. Honderd miljoen jaar nadat straling de zon heeft verlaten wordt het in de economie gebruikt als nuttige arbeid. De biosfeer bewerkstelligt hetzelfde in één jaar.



¹Kernenergie daargelaten

Het tijdsgewricht waarbinnen dit energievraagstuk vorm begon te krijgen (A.D.±1900) is ook de periode dat de eerste ontdekkingen werden gedaan op het gebied van de fundamentele fysische theorie die licht en materie beschrijft, de Quantummechanica. De toevoeging quantum aan de klassieke Newtoniaanse mechanica duidt op het feit dat zowel licht als materie zijn opgebouwd uit quantumtoestanden die geen klassiek continuüm beslaan. Vreemd genoeg kan een quantumstelsel zich tegelijkertijd in verschillende toestanden bevinden genaamd een *superpositie*. Zonlicht is opgebouwd uit energiepakketjes, fotonen, die alleen geabsorbeerd worden wanneer het verschil in energie tussen twee quantumtoestanden van materie exact overeenkomt met de energie van het foton. Gegeven dat materie bestaat uit positieve kernen en negatieve electronen kan de resulterende toestand, het zogenaamde exciton, worden gezien als een positieve kern met daaromheen een negatief electron in een hogere energietoestand.

Een dergelijk exciton kan niet worden gebruikt om een elektrische stroom te genereren. Het negatieve electron en de positieve kern zijn zodanig sterk aan elkaar gekoppeld dat het exciton snel terugvalt naar de initiële toestand door een lichtfoton te emitteren. De uitdaging ligt in het transformeren van het exciton naar een nieuwe quantumtoestand waarbij het electron ruimtelijk is gescheiden van de positieve kern, een zogenaamde ladingsgescheiden toestand.² Omdat kernen veel zwaarder zijn dan electronen wordt hun beweging in de regel buiten beschouwing gelaten. De fundamentele stellingname in dit proefschrift is dat de beweging van de kernen de efficiëntie van zonne-energie-transductie bepaalt. Kernbewegingen worden *coherent* genoemd wanneer zij een superpositie van quantumtoestanden induceren. De fotosynthese gebruikt specifieke kernbewegingen om zonlicht efficiënt om te zetten in bruikbare energie (**Hoofdstukken 3 en 4**). De voorwaarden voor dergelijke kernbewegingen om een superpositie te induceren is *resonantie*, de kernbeweging moet een energie bezitten die gelijk is aan het energieverval tussen de twee quantumtoestanden. Indien aan deze voorwaarde wordt voldaan kruisen de energieën van de twee toestanden elkaar periodiek waardoor de begintoestand gelijdelijk in de eindtoestand wordt omgezet (**Hoofdstuk 5**).

Samenvattend, er zijn quantumtechnologieën mogelijk voorbij de bestaande grenzen voor de efficiëntie van zonne-energie. Zulke technologieën kunnen bijdragen aan een brede toegankelijkheid van betaalbare energie.

²Deze toestand kan gebruikt worden om een elektrisch circuit aan te leggen om de economie ('de weerstand') direct uit zonlicht van energie te voorzien.

Curriculum Vitae



Education

PERIOD	2010 — 2014	Leiden Institute of Chemistry
PHD.	Computational Quantum Mechanics	
	Supervised by Dr. F. Buda and Prof. Dr. H.J.M. de Groot.	
	Title: <i>Coherent Dynamics in Solar Energy Transduction.</i>	
PERIOD	2007 — 2010	Leiden University
MSc.	Physical & Theoretical Chemistry	
	Thesis with Dr. F. Buda and Prof. Dr. H.J.M. de Groot (grade for thesis: 10).	
	Thesis subject: <i>Asymmetry in Reaction Centers.</i>	
	Extra-curricular: Honours Class, Science Based Business.	
	Certificate: Financial Markets Summer School, London School of Economics (2009).	
PERIOD	2002 — 2007	Delft University of Technology
BSc.	Molecular Science and Technology	
	Thesis with Prof. Dr. L.D.A. Siebbeles and Dr. J.M. Schins (grade for thesis: 10).	
	Thesis subject: <i>Excited State and Charge Photogeneration Dynamics in P3HT and P3HT/PCBM blends.</i>	
	Majors: Molecular Quantum Mechanics, Physical Chemistry.	
	Minors: Economics, Sustainable Energy.	
PERIOD	2001 — 2002	Delft University of Technology
	Technology, Policy and Management	
	→ Propedeutic exam.	
PERIOD	1994 — 2000	Sint Ignatius Gymnasium

Languages

ENGLISH **Native**
DUTCH **Native**
ITALIAN **Fluent**

GERMAN **Proficient**
FRENCH **Basic**

Programming & Software

Fortran Bash Unix Matlab Igor Pro LaTeX

OCTOPUS CPMD Gaussian Amsterdam Density Functional

Conference Proceedings

- Thomas J. Eisenmayer, Huub J. M. de Groot, Francesco Buda. *Real-Time Simulations of Photoinduced Processes*, CHAINS, (Veldhoven, 2014). **Talk**
- Thomas J. Eisenmayer, Huub J. M. de Groot, Francesco Buda. *Charge Transfer and Coherent Dynamics*, Physics@FOM, (Veldhoven, 2014). **Talk**
- Thomas J. Eisenmayer, Huub J. M. de Groot, Francesco Buda. *From Photosynthesis to Solar Fuel*, Holland Research School of Molecular Chemistry, (Naturalis, 2013). **Talk**
- Thomas J. Eisenmayer, A. Monti, J. Rombouts, Huub J. M. de Groot, Francesco Buda. *In Silico Design of Novel Charge Separators*, European Science Foundation, (Torun, 2013). **Talk**
- Thomas J. Eisenmayer, Huub J. M. de Groot, J. Neugebauer, Francesco Buda. *Mechanism and Reaction Coordinate of Directional Charge Separation in Bacterial Reaction Centers*, Study group Spectroscopy and Theory, (Utrecht, 2012). **Talk**
- Jorge Piris, Thomas J. Eisenmayer, Minh T. Trinh, Juleon M. Schins and Laurens D.A. Siebbeles: *Photoexcitations and Charge Generation Dynamics in P3HT/PCBM Blended Films Studied by Ultrafast Transient Absorption Spectroscopy*. Materials Research Society, Symposium H: Nanostructured Solar Cells (Boston, 2007). **Abstract**

List of Publications

- T. J. Eisenmayer, F. Buda. "Real-Time Simulations of Photoinduced Coherent Charge Transfer and Proton-Coupled Electron Transfer", *ChemPhysChem*, **2014**, 15 (15), pp 3258-3263.
DOI: 10.1002/cphc.201402444
--> **Chapters 5 and 7** of this thesis.
- T. J. Eisenmayer, H. J. M. de Groot, E. van de Wetering, J. Neugebauer, F. Buda, "Mechanism and Reaction Coordinate of Directional Charge Separation in Bacterial Reaction Centers", *Journal of Physical Chemistry Letters*, **2012**, 3, pp 694-697.
DOI: 10.1021/jz201695p
--> **Chapter 3** of this thesis.
- T. J. Eisenmayer, J. A. Lasave, A. Monti, H. J. M. de Groot, F. Buda, "Proton Displacements Coupled to Primary Electron Transfer in the Rhodobacter Sphaeroides Reaction Center", *Journal of Physical Chemistry B*, **2013**, 38, pp 11162-11168.
DOI: 10.1021/jp401195t
--> **Chapter 4** of this thesis.
- K. S. Joya, J. L. Valles-Pardo, Y. F. Joya, T. J. Eisenmayer, B. Thomas, F. Buda, H. J. M. de Groot, "Molecular Catalytic Assemblies for Electro-driven Water Splitting", **2013**, *ChemPlusChem*, **78**, pp 35-47.
DOI: 10.1002/cplu.201200161
- T. J. Eisenmayer, J. Marcelis, H. J. M. de Groot and F. Buda, **2014**, "Redox levels and Oxidation Potential in Photosystem II: A DFT investigation", *to be submitted*.
--> **Chapter 6** of this thesis.
- **2015**, "A Practical Quantum Theory for Efficient Solar Energy Transduction", *in preparation*.
--> **Outlook** of this thesis.